Experimental Study of Ultrafast Carrier Dynamics and Plasmons in Nanostructures

by

Dimitri Chekulaev

A thesis submitted to
The University of Birmingham
for the degree of
DOCTOR OF PHILOSOPHY

Nanoscale Physics Research Laboratory
School of Physics and Astronomy
The University of Birmingham
Birmingham B15 2TT
United Kingdom
February 2012

Abstract

This thesis is devoted to the experimental investigation of ultrafast dynamics in silicon nanostructures and surface plasmonics by means of femtosecond lasers.

First part of the research, ultrafast carriers dynamics in silicon nano-structures, is based on the time-resolved pump-probe reflectivity method. A change in the density of excited carriers, as a response to the change of the excitation intensity, was extracted from the time-resolved reflectivity of crystalline nanopillars and nano-inclusions. The measurements were performed mainly in the sub-melting fluence regime, at nearly normal incidence to the sample surface plane of the pump and probe beams. Both types of nano-structures have shown strong intensity dependent response comparing to bulk crystalline silicon. This enhanced response is attributed to a suppression of the diffusion processes in nanopillars and nonlinear response due to a constructive multilayer interference between the host matrix material, where silicon inclusions have been embedded, and the sublayers. Electron-phonon and recombination characteristic decay-times are extracted.

The second part is devoted to sub-nanosecond decay of photoluminescence from silicon-nitride amorphous structures. Particular structures have shown two radiative decay peaks. The second radiative peak is addressed to deep subband tail states, originated by the open bonds of the amorphous structure leading to the long radiative transition.

The last part describes femtosecond-resolved plasmon-assisted dissociation of diatomic oxygen molecules in ultrahigh vacuum conditions. Asymmetric gold gratings have been utilised to create enhanced local electric fields originated from the optically excited surface plasmon resonances. Charged products of the dissociation process have been analysed by time-of-flight linear drift mass spectrograph, while two-dimensional distribution has been achieved deploying Velocity Map Imaging technique. The dissociation process is found intensity dependent with strong non-linear profile. No correlation has been observed with background plasmon-enhanced electron emission.

Acknowledgements

The author thanks the XTRA for the financial support during the early stages of this project and expresses gratitude to the Midlands Physics Alliance Graduate School (MPAGS) for the award of a PhD studentship.

My sincere appreciation goes to Dr. Andrey Kaplan of the School of Physics and Astronomy of the University of Birmingham for his invaluable supervision and help. I am grateful to Prof. Richard E. Palmer, Head of the Nano-Physics Research Laboratory (NPRL), for the opportunity to work in the group. I would also like to express my thanks to Mr. Valery Garber, Chief Technology Officer at DC Sirica Ltd, for providing samples and to Dr. Emmanuel Baskin of the Solid State Institute at the Technion - Israel Institute of Technology, for fruitful discussions.

I must also acknowledge the contribution of many people in the group (NPRL) and the School, who have been directly or indirectly associated with this project, in particular Mi Yeon Song for the SEM images of our sample. My special thanks goes to Emma Catton who helped me with technical introduction at the beginning of my work and to Tomas Roger for his scrupulous maintenance of the new laser apparatus.

Finally, I want to sincerely thank all my family and friends for their support and endless encouragement.

Contents

List of Figures

List of Tables

List of Symbols and Abbreviations

Symbols

α - Linear absorption coefficient

β - Two-photon absorption coefficient

e - Electron charge

ϵ_0 - The vacuum permittivity ϵ - Host dielectric constant

D_N - Ambipolar diffusion coefficient

E - Electric field

E_g - Semiconductor gap energy

F - Fluence F_m - Melting threshold fluence

I - Intensity

NL - Order of non-linearity

λ - Excitation wavelength

m_e - Electron mass m_{eff} - Effective electron mass m_{heff} - Effective mass of a hole

N_{e-h} - Electron-hole plasma density

n - Refractive index n_p - Electron-hole plasma affected refractive index (Drude model)

k - k-vektor

k_B - Boltzmann constant

R_0 - Absolute reflection R - Reflectivity

T - Temperature

t - Time τ - Delay/decay time

τ_{e-ph} - Electron-phonon interaction time τ_r - electron-hole recombination time

U_{pond} - Ponderomotive energy

ω - Excitation angular frequency ω_p - Electron-hole plasma frequency

Abbreviations

2D - Two-dimensional
3D - Three-dimensional
α**-Si** - Amorphous Silicon
A/D - Analog-to-Digital
CCD - Charge-Coupled Device
CW - Continuous Wave
FC - Free Carrier
FWHM - Full Width at Half Maximum
MCP - Micro Channel Plate
SEM - Scanning Electron Microscope
SiN - Silicon Nitride (SiN_x)
SiNP - Silicon Nano-Pillars
SiNI - Silicon Nano-Inclusions
SP - Surface Plasmon (resonance)
PECVD - Plasma Enhanced Chemical Vapour Deposition
PEEM - Photo-Emission Electron Microscope
PL - Photoluminescence
ToF - Time of Flight
TRPL - Time-Resolved Photoluminescence
VMI - Velocity Map Imaging

Chapter 1

Introduction

1.1 Femtosecond spectroscopy

Femtosecond spectroscopy allows to resolve molecular and electronic processes ocuring on a timescale as short as $10-100$ femtoseconds (1 femtosecond $= 10^{-15}$ of a second). Among these processes are vibrational motion in molecules, relaxation and dephasing of weakly bound electrons and electron-hole dynamics in semiconductors. The former can be attributed to the Femtochemistry field, which has gained particular attention in 1999, when Ahmed H. Zewail received the Nobel Prize in Chemistry for pioneering observation of intermolecular atomic motion during a chemical reaction [1]. Study of various electronic processes taking place on the femtosecond scales are known as Ultrafast Carrier Dynamics field, although, recent advances in the femtosecond laser technology allowed to resolve subfemtosecond (attosecond) processes associated with inner-shell electron transitions [2].

During last twenty years, titanium-doped sapphire crystal has remained the core of ultrashort broadband pulses, while scientific and engineering efforts have been applied to shorten an output pulse duration as well as improving its power and stability characteristics [3]. Broadly speaking, the nature of optical experiments consists of two essential mechanisms: an excitation and a detection. Femtosecond lasers can be a good example where an optical rate of "information transfer" (in its general meaning) appears to be significantly higher than the electronic one. Namely, electronic measuring devises in principle are limited by a response time being in order of picoseconds (1 picosecond $= 10^{-12}$ of a second) making time-resolved detection of ultrafast events impossible. To overcome this issue, the femtosecond spectroscopy is based on the utilisation of methods where a detection occurs in a "relative" time rather than in the “real” one. The relative time is known as a “delay time”, being the time between two laser pulses, where one pulse is responsible for an excitation of the investigated system and another one is responsible for a triggering of the detection. The delay time can be achieved by splitting of an initial laser beam into two beams with variable optical path length, transforming the (delay) time control task into (one dimensional) spatial control task.

The ultrafast optical investigations have been applied in many areas, here are just a few of them: two-photon photoemission microscopy of nano-optical fields [4, 5]; photoelectron spectroscopy and momentum map imaging of fullerenes [6] and noble gases during the above-threshold ionisation [7, 8]; lattice stability [9] and ablation [10]; carriers relaxation and recombination processes in metals [11, 16] and semiconductors [13, 14, 15]; ellipsometry investigation of the optical properties of metals [16] and semiconductors [17]; ultrafast control of surface plasmon propagation [18].

This work represents diverse application of ultrafast laser facilities in the following aspects: (i) monitoring of ultrafast electron-hole dynamics in crystalline silicon nanometer structures, utilising infrared (800 nm) light, (ii) time-resolved photoluminescence from amorphous silicon nitride thin films, deploying super-continuum spectrum generated from 1 μm femtosecond fiber laser and (iii) surface plasmon-assisted dissociation of oxygen by visible (400 nm) ultrashort pulses. Such broad application potential is another indication that femtosecond spectrometry is a powerful tool to study a variety of physical phenomena.

1.2 Thesis structure

This thesis is arranged in three main chapters, each chapter is associated with one of the following experimentally investigated topics:
(Chapter 2) Ultrafast Carriers Dynamics in crystalline silicon nano-structures,
(Chapter 3) Time-resolved photoluminescence from silicon-nitride thin film,
(Chapter 4) Surface plasmon assisted oxygen dissociation in a high vacuum.

Structural presentation of each chapter appears in four major sections devoted to a theoretical introduction, a technical background, experimental results and data analysis. Conclusions and future plans are brought up by the end of each chapter. Additional matter can be found in Appendices when referred to.

Chapter 2 - *Ultrafast Carriers Dynamics in Silicon Nano-structures.*

In the first section, relevant concepts of time-resolved reflectivity and related optical quantities are introduced. Further on, the time-resolved pump-probe reflectivity technique is briefly described. Also a number of different experimental techniques for measuring of fast electron dynamics are reviewed.

In the second section, the experimental setup is described in some detail. The peculiar problems which arise from the necessity to measure weak optical response in the strong irradiated background are discussed, and a few weaknesses of the experimental setup are pointed out.

In the third section, the experimental results for the time-resolved reflectivity of silicon nanopillars and nano-inclusions are presented. These results are compared with bulk silicon measurements. It is found that both silicon nano-structures show an increased change in time-resolved reflectivity comparing to bulk silicon.

In the fourth section, a qualitative analysis of the results is made and supported by simulations of the free electron-hole plasma in silicon. The enhanced change in time-resolved reflectivity of nanopillars is addressed, in particular, to the low dimensionality of the semiconducting surface structure grown on an insulator. In the case of nano-inclusions, the enhanced change is attributed to the constructive interference, which was originated by multilayered structures of the sample.

Conclusions and future plans are brought up in the last section.

Chapter 3 - *Time-resolved photoluminescence.*

The first section, devoted to the overview of photoluminescence from silicon-nitride thin films and other amorphous semiconductor structures, concentrating on the time domain of this phenomena. An exponential and non-exponential photoluminescence decay forms are addressed.

The second section, describes the experimental setup dedicated to investigate photoluminescence in the subpicosecond timescale. Silicon-nitride thin film samples and some of their optical properties have been introduced.

Experimental results have been presented in the third section. Characteristic exponential decay times are extracted.

The fourth section is focused on an interpretation of a double radiative decay process observed from some of the silicon-nitride thin films. Dynamical model is presented and fitted to the experimental data. A comparison with literature is done.

Last section summarises this work.

Chapter 4 - *Surface plasmon assisted oxygen dissociation.*

In the first section, motivation for this work is expressed throughout currently available ultrafast near-field microscope tools designed to resolve nano-particle objects. Alternative experimental technique being based on the surface plasmon assisted dissociation is proposed.

The second section is dedicated to the surface plasmon theoretical background. The core idea of the strong field gained from the resonant photo-excitation of electrons in metal and application of this field to the dissociation is explained.

The third section presents experimental apparatus based on the time-of-flight mass spectrometry and an adaptation of Velocity Mapping Imaging method for time selected two-dimensional projection of charged particles in the high vacuum.

Experimental evidence of plasmon-assisted dissociation is shown in the fourth section. Temporal resolution of this process is shown when two delayed optical femtosecond pulses have been applied.

The fifth section dedicated to the qualitative analyse of plasmonics involvement in the dissociation process.

Last section provides conclusions and future plans of this work.

The thesis conclusion is brought in the last chapter. The mentioned above experimental works have resulted or contributed to scientific articles being addressed in Appendix A.

Chapter 2

Ultrafast carriers dynamics in silicon nano-structures

2.1 Introduction

During the last three decades there have been advanced achievements in the area of ultrafast carrier dynamics in semiconductors. Scientific interest, apart from the basic fundamental interest, is the application of semiconductor devices and the growing need for faster response and processing of information. To be able to continuously improve and develop microelectronics devices and address these needs, a detail understanding of various dynamical processes in semiconductors is required. These constant needs triggered massive research activity in the area of the excitation of semiconductors out of their equilibrium and subsequent various rates relaxation processes. Tremendous investigation activity has been enabled by the development of the ultrafast pulsed lasers which can generate pulses of duration as short as a few femtoseconds, leading the excitation and following probing of semiconductors on an ultrashort timescale. Example of these ultrafast processes, carrier momentum randomisation, carrier thermalisation and energy relaxation, have been reviewed in detail using "pump and probe" techniques elsewhere [3].

The most developed way to follow a relaxation process can be done by means of investigation of optical response such as absorption, transmission, reflection and second harmonic generation. This work is devoted to time-resolved reflectivity of silicon based nano-structures, being in the focus of scientific interest during last decade, for example [19, 20, 21].

2.1.1 The aim of this work

This work attempts to fill the void in knowledge of ultrafast carrier dynamics in semiconductor nano-structures, where quasi one- and two-dimensional topological conditions apply new restrictions on carriers behaviour, unseen in bulk measurements. One of the processes directly affected would be diffusion. Thus, the decay process is governed by relaxation dynamics solely, excluding a contribution from the carrier transport. We will discuss absolute enhancement of the time-resolved reflectivity signal from quasi one-dimensional crystalline silicon nano-structure (nanopillars) and even much bigger enhancement from a two-dimensional array of crystalline nano-particles embedded in an amorphous silicon matrix layer. These results will be compared to bulk crystalline silicon measurements.

2.1.2 Generation of electron-hole plasma in semiconductors

Free electrons and holes of a semiconductor material, under equilibrium conditions, are distributed according to the Fermi-Dirac statistics, while phonons characterise lattice excitations following the Bose-Einstein statistics [22]. In the absence of any external force, energy and momentum are interchanged through carrier-carrier and carrier-phonon interactions keeping both distributions at a common temperature. Under these conditions, an average momentum of the carrier and phonon systems is zero, while their average energies are represented by their common temperature. When an optical electromagnetic radiation is absorbed by a semiconductor, the equilibrium is disturbed leading different thermal states of the two systems. However, the carriers return to equilibrium within short time after the external excitation is switched off. The average momentum relaxes to zero, while the average carrier temperature reaches an equilibrium with the lattice temperature as carriers lose momentum and energy to phonons through variety of scattering processes. The rate of momentum and energy relaxation taking the carriers to the equilibrium is determined by the character of the scattering and the number of the events being involved in electron-phonon coupling.

Figure 2.1 shows a schematic representation of the major processes following photoexcitation of a direct semiconductor with a monochromatic polarised laser light assumed to be a delta function in time, which is an approximation of a real ultrashort pulse excitation. Absorption of an optical electromagnetic radiation by a semiconductor, where the quanta of energy $\hbar\omega_0$ is above the band gap energy E_g, results in the creation of electron-hole pairs with

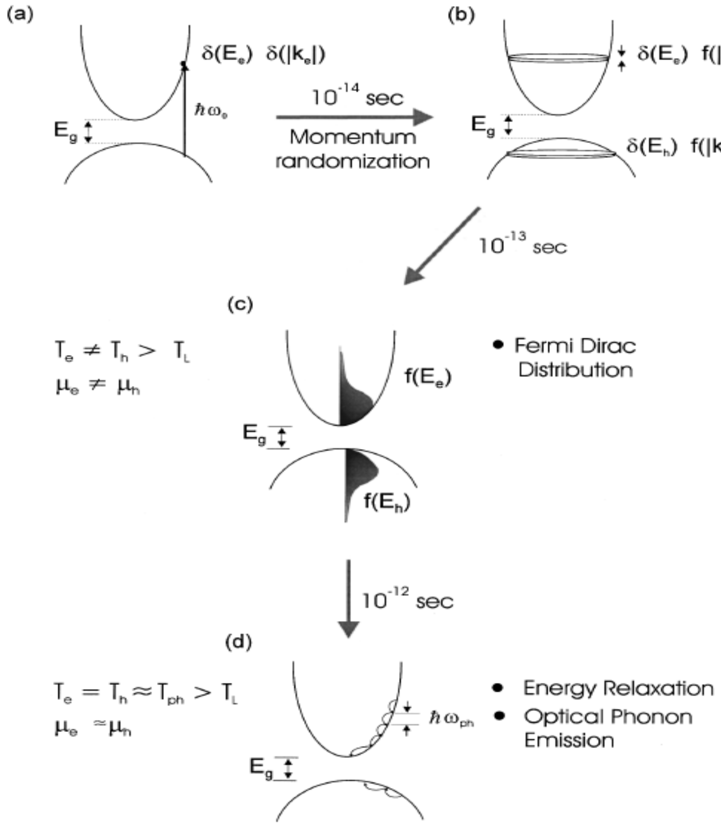

Figure 2.1: A schematic diagram illustrating the photoexcitation of a semiconductor and subsequent energy relaxation. a) Initially after photo-excitation with light, the carriers will have delta function distribution in momentum and energy space. b) Within tens of femtoseconds momentum randomisation occurs. c) Thermalisation of carriers into a Fermi-Dirac distribution for carrier densities greater than 10^{19} cm^{-3} via collision occurs on 10^{-13} s. d) As time evolves the hot carriers lose their excess kinetic energy while attempting to reach thermal equilibrium with the lattice through optical phonon scattering, from [3].

excess kinetic energy corresponding to the residual energy $(\hbar\omega_0 - E_g)$. This initial excitation by a monochromatic and polarised radiation produces distributions of electrons and holes that are narrow in energy (restricted by the Pauli exclusion principe), $\delta(E_e)$ and $\delta(E_h)$, respectively, and peaked in particular directions of momentum space, $\delta(|k_e|)$ and $\delta(|k_h|)$, see Figure 2.1(a). However, elastic and inelastic scattering events randomise momenta within tens of femtoseconds, Figure 2.1(b).

Following photo-excitation the electrons own most of the initial kinetic energy because their effective mass is much lighter than mass of the holes. This means that initially electrons and holes have to be considered as separate systems each with their individual thermal distributions, resulting electron-hole interactions to be weak comparing to other carrier-carrier interactions. Electron-electron and hole-hole collisions are density dependent. For carrier densities greater than 10^{19} cm^{-3} with thermal energy of 1000 K these collisions occur on approximately 10^{-13} s timescale and cause thermalisation of the carriers (time required to establish a carrier temperature) into a Fermi-Dirac distribution, Figure 2.1 (c). Subscripts e, h and L correspond to electrons, holes and lattice, respectively. T and μ describe temperature and chemical potential, respectively.

The distribution functions for electrons, $f(E_e)$, and holes, $f(E_h)$, possess different temperatures which may be higher or lower than the lattice temperature depending on $\hbar\omega_0$. As time evolves the hot carriers lose their excess kinetic energy due to attempts to reach thermal equilibrium with the lattice through various scattering mechanisms. The most efficient mechanism is the optical phonon scattering. Through interaction with the carriers the population of non-equilibrium optical phonons increases and attempts to thermalise on a picosecond timescale with other lattice modes via phonon-phonon interactions.

2.1.2.1 Ultrafast carrier dynamics

Usually, the meaning of *ultrafast dynamics* corresponds to the processes occurring on a sub-picosecond scale. Summarised below are fundamental processes in semiconductors on the femtosecond to tens of nanosecond timescale [3]:

- Carrier-carrier scattering	$10^{-15} - 10^{-12}$ *sec*
- Intervalley scattering	$\geq 10^{-14}$ *sec*
- Intravalley scattering	$\sim 10^{-13}$ *sec*
- Carrier-optical phonon thermalisation	$\geq 10^{-12}$ *sec*
- Optical phonon-acoustic phonon interaction	$\sim 10^{-11}$ *sec*
- Carrier diffusion (0.1 μm)	$\sim 10^{-11}$ *sec*
- Auger recombination (carrier density 10^{20} cm^{-3})	$\sim 10^{-10}$ *sec*
- Radiative recombination	$\geq 10^{-9}$ *sec*
- Lattice heat diffusion (1 μm)	$\sim 10^{-8}$ *sec*

Irradiation of a semiconductor by above band gap energy photons triggers the generation of large non-equilibrium carrier densities and elevated carrier temperatures. Depending on the incident fluence and the photon energy of the employed laser beam, particle densities of several orders of magnitude above the equilibrium value may be reached while carrier temperatures of several thousands degrees can be achieved. This temperature change affects various macroscopic parameters such as those responsible for the optical properties of the system.

Following optical excitation, electrons and holes undergo spatial and temporal evolution with characteristic times being dependent on the number of relaxation processes (as described above). Energy relaxation of carriers occurs primarily by virtue of the emission of optical phonons. In the case of the holes, this interaction includes optical phonons generated in the vicinity of the Brillouin zone centre.

2.1.2.2 Optical properties of excited silicon

Shortly after the excitation, the optical properties of the semiconductor are changed from those of the unexcited state. It is possible to follow these changes by measuring the dielectric constant, ϵ^* or, related to it, refractive index, n. In general, the dielectric constant depends on the concentration of free carriers, however the following physical effects could be regarded as nearly independent while they contribute to ϵ^*: state and band filling, renormalisation of the band structure, and the free-carrier response, according to [23]. The fourth effect, lattice temperature changes, will be described in terms of the refractive index n.

For simplicity, we assume that each mechanism contributes separately to the dielectric constant ϵ^* of the excited material:

$$\epsilon^* = \epsilon_g + \Delta\epsilon_{pop} + \Delta\epsilon_{bgs} + \Delta\epsilon_{fcr}. \tag{2.1}$$

Where ϵ_g is the dielectric constant of the unexcited material, which is for silicon at 800 nm $\epsilon_g = 13.656 + i0.048$, according to [24]. $\Delta\epsilon_{pop}$, $\Delta\epsilon_{bgs}$ and $\Delta\epsilon_{fcr}$ represent the changes of the dielectric constant due to state and band filling, renormalisation of the band gap, and the free-carrier response, respectively.

State and band filling

A characterisation of the state and band filling effect, $\Delta\epsilon_{pop}$, may require a deep understanding of the carrier distribution in the conduction and valence bands. However, due to the high plasma temperature (above 1000 K) it is reasonable to assume that the carriers are nearly homogeneously distributed over the Brillouin zone. Thus, according to Biswas *et al.* [25], the magnitude of $\Delta\epsilon_{pop}$ could be roughly estimated from the ratio of the density

N_{e-h} of excited electron-hole pairs and the total valence-band density N_0, which for silicon is equal to $N_0 = 2 \times 10^{23}$ cm^{-3}, in the unexcited state:

$$\Delta\epsilon_{pop} = -(\epsilon_g - 1)\frac{N_{e-h}}{N_0}. \tag{2.2}$$

For more details, see Appendix B. A rough estimation of this value gives
$\Delta\epsilon_{pop} \approx -(13.6 - 1)\frac{5\times10^{20}}{2\times10^{23}} = -0.03$.

Band-structure renormalisation

Band-structure renormalisation takes into account changes of the single-particle energy due to many-body interactions in the excited plasma. In most cases, these changes are treated as a rigid shift of the band structure resulting in a shrinkage of the energy gap ΔE_{gap} being proportional to the cubic root of the density. Particular deviations from the cubic root law can be expected due to the temperature dependence of ΔE_{gap}. Neglecting this dependence, the changes of the optical properties can be estimated within the rigid band shift model from a corresponding shift of the optical spectra:

$$\Delta\epsilon_{bgs} = \epsilon_g(\hbar\omega + \Delta E_{gap}) - \epsilon_g(\hbar\omega). \tag{2.3}$$

According to Abram *et al.* [26], such band gap renormalisation has order of 50 meV, leading to the following estimation:
$\Delta\epsilon_{bgs} = \epsilon_g(1.55\ eV + 50\ meV) - \epsilon_g(1.55) = 0.01$.

Free-carriers response

Changes of the optical constants (away from the plasma resonance) resulted by the response of the free carriers can be regarded within the scope of the Drude model:

$$\Delta\epsilon_{frc} = -\frac{N_{e-h}e^2}{\epsilon_0\epsilon_{host}m_{opt}\omega^2}\frac{1}{1 + i(\omega\tau_D)^{-1}} = -(\frac{\omega_p}{\omega})^2(1 + i(\omega\tau_D)^{-1})^{-1} \tag{2.4}$$

ϵ_0 is the dielectric constant of vacuum, ϵ_{host} the dielectric function of the host material and ω denotes the photo-excitation frequency. $m_{opt} = (1/m_{eff} + 1/m_{heff})^{-1}$ denotes the optical effective mass of the carriers (m_{eff} and m_{heff} are the mobility effective masses of electrons and holes; thus total mobility, $\mu \propto 1/m_{eff} + 1/m_{heff} = 1/m_{opt}$). τ_D is the Drude damping time and $\omega_p = \sqrt{(N_{e-h}e^2)/(\epsilon_0\epsilon_{host}m_{opt})}$ is the plasma frequency.

The value of optical mass for dense plasma in silicon is calculated [27] and it varies between 0.156 m_e at a plasma temperature of 300 K and 0.205 m_e at 2000 K, respectively. The Drude damping time τ_D is density and temperature dependent. It is found to be on the order of 100 fs for low densities and determined by carrier-phonon collisions. For high density, where dominant collisions are carrier-carrier, these timescales are approximately two orders of magnitude lower.

A rough estimation yields $\Delta\epsilon_{frc} \approx -(\omega_p/\omega)^2 = -0.1$ at $N_{e-h} = 5 \times 10^{20}$ cm^{-3} and $\lambda = 800$ nm. Summarising the contributions, described above, to the dielectric constant, it is possible to conclude that the main influence comes from the free-carrier response and all the rest are negligible and are neglected for the simplicity of calculations, for example see Figure 2.2 below.

More useful than the dielectric function ϵ_g, is the refractive index n, related to ϵ_g as: $\hat{n} = n - ik = \sqrt{\epsilon_g}$. Here, k represents the extinction coefficient and $\hat{n}$ is a complex refractive index.

Moreover, in cases where the absorption rate is low, the collision rate Drude model, see Eq. 2.4, might be simplified by neglecting damping (when $1/\tau_D \ll \omega$), for example see [13]. Thus Eq. 2.1 expressed using the refractive index, n, becomes:

$$n_p = n\sqrt{1 - w_p^2/w^2}. \tag{2.5}$$

Here, n_p denotes the refractive index affected by the electron-hole plasma of the Drude model.

Lattice temperature changes

Changes in the dielectric function due to increased lattice temperature might be estimated empirically [27] using linear thermo-optical coefficient dn/dT_L:

$$\Delta n_{LT} = (\frac{dn}{dT_L})\Delta T_L. \tag{2.6}$$

Here, T_L is a lattice temperature and Δn_{LT} is a lattice temperature change contribution to the refractive index. For wavelengths relevant to our experiment, the temperature gradient is in order of $dn/dT_L = 3.4 \times 10^{-4}\ K^{-1}$ [27]. Thus, for a temperature change of approximately 1000 K, a rough estimation is approximately $\Delta n_{LT} \approx 0.005$. Which leads to $|\Delta n_{LT}| \ll |\Delta\sqrt{\epsilon_{frc}}|$. This makes a lattice temperature contribution to the optical properties of the material minor comparing to the contribution of the free carriers. This allows us to regard this work in the scope of the free-electron picture only.

2.1.3 Optical constants and reflectivity

Generally speaking, an electromagnetic wave interacting with matter can be either reflected, transmitted or absorbed by the matter. The energy conservation requirement leads to the following relation [28]: $T + R + A = 1$, where T, R and A are normalised to unity quantities expressing transmission, reflection and absorption, respectively. The first two are experimentally measurable quantities and the last one has to be extracted through the given probability relation.

The relation between reflection, R and n (and k for absorbing medium) is as follows:

$$R = \frac{(n_1 - n_2)^2 + ik_2^2}{(n_1 + n_2)^2 + ik_2^2}, \tag{2.7}$$

where subscripts *1* and *2* represent first (non-absorbing, $k_1 = 0$) medium and reflecting (and absorbing) medium, respectively. In the non-equilibrium case, the absorption of light in solid silicon is determined by the density, the temperature, and the spatial profile of the excited carrier plasma. In silicon, electron-hole pairs are created by linear and by two-photon absorption. Neglecting recombination and diffusion during and shortly after excitation, carrier generation can be described by the following differential equation for the time and spatial excitation depth dependent intensity $I(z, t)$:

$$dI[\frac{1}{I(z,t) + \alpha_0/\beta} - \frac{1}{I(z,t)}] = \alpha_0 dz, \tag{2.8}$$

with a solution in the form:

$$I(z,t) = \frac{\alpha_0}{[\alpha_0/I_0 + \beta]\exp{(\alpha_0 z)} - \beta}. \tag{2.9}$$

Here z denotes the spatial coordinate perpendicular to the surface and t is the time. α_0 and β describe linear and two-photon interband absorption, I_0 is the maximal amplitude of the intensity peak.

More realistic model could be adopted from the work of Sokolowski *et al.* [23], where equations for the carrier density N_{e-h} and the excitation intensity are given in the following form:

$$\frac{\partial}{\partial z} I(z,t) = -[\alpha_0 + \alpha_{fca}(z,t) + \beta I(z,t)]I(z,t), \tag{2.10}$$

$$\frac{\partial}{\partial t} N_{e-h}(z,t) = \frac{\beta}{2\hbar\omega}[-(I + \alpha_0/\beta)^2 + (\alpha_0/\beta)^2]. \tag{2.11}$$

Here, the intraband free-carrier absorption is included via a space and time-dependent coefficient α_{fca}. Assuming a Gaussian pulse shape of the form $I_0 exp(-(t/t_0)^2)$, the density equation can be integrated in time. In order to calculate the fraction of the incident laser pulse energy being coupled to the material, it is possible to neglect changes of the reflectivity R during the pump pulse, up to certain fluence. Using fluence $F_0 = \sqrt{\pi} t_0 I_0$, the excited carrier density N_{e-h} relates to reflectivity R via:

$$N_{e-h} = F_0 \frac{1-R}{\hbar\omega}[\alpha_0 + \beta F_0 \frac{1-R}{2\sqrt{2\pi} t_0}]. \tag{2.12}$$

Figure 2.2 from Ref. [23] shows theoretical predictions for the reflectivity of silicon as a function of the excited electron-hole density N_{e-h}, at 625-nm wavelength, 49° angle of incidence, and $p-$polarisation. The dotted curve shows contributions due to band-gap shrinkage, state and band filling. The dashed curve shows the pure Drude contribution. The solid curve presents the total reflectivity according to Eq. 2.1.

Figure 2.2: Theoretical predictions for the reflectivity of silicon as a function of the excited electron-hole density, 625-nm wavelength, 49° angle of incidence, and $p-$polarisation. Dotted curve: contributions due to state and band filling and band-gap shrinkage; dashed curve: pure Drude contribution; solid curve: total reflectivity according to Eq. 2.1, from [23].

2.1.4 Time-resolved reflectivity

According to the previous section, exposing a surface to the extremely short (shorter than carrier diffusion and recombination timescale) optical pulse changes optical properties of the reflected beam. In particular, a change in time-dependent reflectivity, $R(t)$, defined as $\Delta R(t) \equiv R(t) - R_0$ (R_0 being reflectivity of an unexcited material) could be expressed [27] via a change in the time-dependent refractive index $|\Delta n(t)| \ll n$ as:

$$\frac{\Delta R(t)}{R_0} = \frac{4ncos(\theta)}{(n^2-1)\sqrt{n^2-\sin^2(\theta)}} Re(\Delta n(t)), \tag{2.13}$$

where $\Delta n(t)$ includes all contributions from free carriers response, lattice temperature changes, band-structure renormalisation, state and band filling. Here, θ denotes the angle of incidence and n is the refractive index of the unexcited matter. The relation between $R(t)$ and the time-dependent excited carriers population $N_{e-h}(t)$ comes from the total dielectric function (and refractive index) change, see Eq. 2.1, which is directly related to $N_{e-h}(t)$.

Figure 2.3 (a) describes transient reflectivity in silicon on the femtosecond timescale, firstly measured by Shank *et al.* [13]. The 90 fs excitation pulse at a wavelength of 1 μm was used to excite an electron-hole plasma below and above the melting energy, E_{TH}. In this case, melting means irreversible degradation of the silicon crystal lattice structure and formation of a temporary "fluid". In the submelting regime (curve marked as 0.63 E_{TH}) the negative change in reflectivity comes mainly from free carrier excitation followed by recombination and lattice heating (saturated part) on a longer timescale.

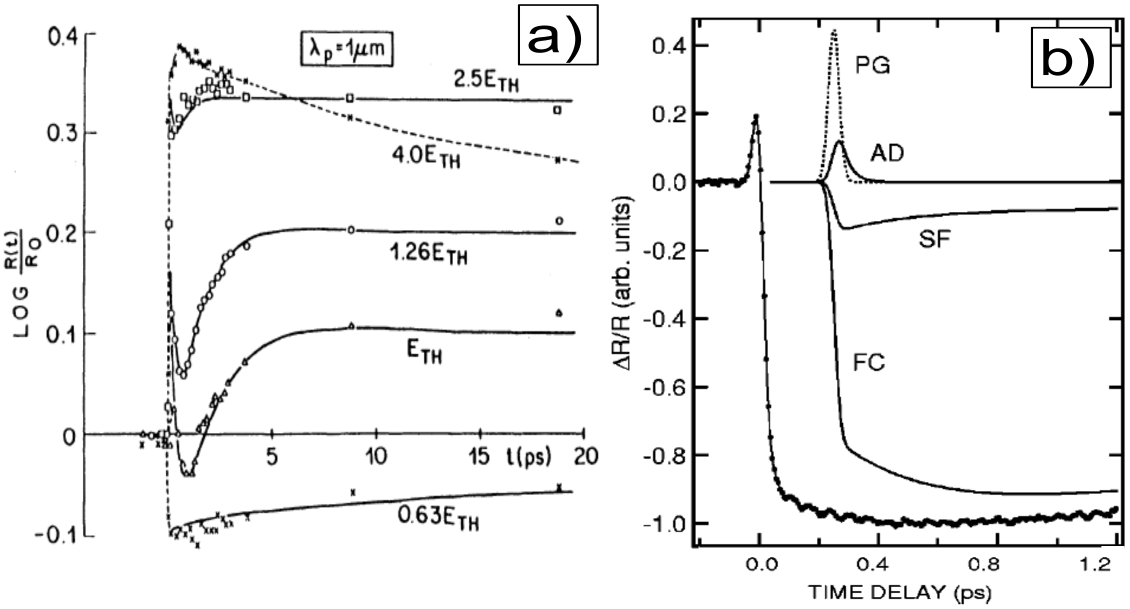

Figure 2.3: Time-resolved reflectivity in silicon. a) below and above surface melting energy (E_{TH}), a 90 fs excitation pulse was used at a wavelength of 1 μm, from [13]. b) Least-squares analysis of Si time-dependent reflectivity. Data, overall fit, and components: free carriers (FC), state filling (SF), polarisation grating (PG) and anisotropic distribution (AD) are shown. The individual components are shifted by 0.25 ps, adopted from [27].

Figure 2.3 (b) shows recent measurements of reflectivity from silicon with even shorter pulses of 28 fs and a fluence of 2.4 mJ/cm^2 (approximately 1.5% of E_{TH}). The authors [27] present a multi-parameter fit to the experimental data. FC depicts the main (and negative) change in reflectivity, which is based on the Drude model, see Eq's. 2.4 and 2.5. Contribution of state filling is depicted by the SF curve.

Polarisation grating (PG) arises from orthogonally polarised excitation and probing pulses leading to an anisotropic initial momentum distribution. This phenomenon was not observed in our work. A degenerate four-wave mixing contribution (AD) comes from the interaction of a probing beam with an anisotropic component of the carrier distribution induced by an excitation beam. According to the authors, this contribution is the smallest, providing us with a legitimisation to neglect it in the present work.

It is easy to see that the contribution of the free carriers to the change of the reflectivity is the major one.

2.1.4.1 Reflectivity from thin films

In the case of thin film layered structures (the compared to the penetration depth of the wavelength into matter), interference effects may affect reflection by increasing it - constructive interference or decreasing it - destructive interference. In the case of a single, thin and non-absorbing layer Eq. 2.7, according to [29], transforms into

$$R = \frac{(n_1^2+n_2^2)(n_2^2+n_3^2) - 4n_1n_2^2n_3 + (n_1^2-n_2^2)(n_2^2-n_3^2)\cos(2\delta_2)}{(n_1^2+n_2^2)(n_2^2+n_3^2) + 4n_1n_2^2n_3 + (n_1^2-n_2^2)(n_2^2-n_3^2)\cos(2\delta_2)}, \tag{2.14}$$

where $\delta_2 = 2\pi n_2 d_2 \cos(\phi_2)/\lambda$ is the change in phase of the beam on traversing the film each time. Here, n_2 and d_2 denote the refractive index and thickness of the film, respectively; ϕ_2 is the angle of propagation of the wave with wavelength λ in the film. Subscripts *1, 2* and *3* represent first (usually air), thin film and third (usually substrate) reflecting media, respectively. In the case of an absorbing film, n_2 should be replaced by the complex refractive index $\hat{n}_2 = n_2 - ik_2$.

2.1.5 Experimental methods

To be able to investigate extremely fast phenomena such as the various carrier dynamics in semiconductors, several ultrafast techniques have been established. For example: the pump-and-probe technique, the streak camera, optical Kerr gate, and up-conversion gate. This section dedicated to a brief description of the mentioned above examples of the most popular techniques [3].

2.1.5.1 Pump-and-probe technique

The meaning of “pump” is the creation of the event by applying a laser pulse that induces in some way an excitation of the sample. The sample is disturbed from its equilibrium state and returns after some time to its initial state. In the pump-and-probe or excite-and-probe technique an ultrashort laser pulse is optically split into a couple of pulses, the pump and the probe, with a variable optical delay between them (Δt). This couple of incident ultrashort laser pulses have to overlap spatially on the sample surface being under investigation. Ideally, the probe beam has to be fully covered by the pump beam. The intense pump pulse excites the sample, causing a change in its properties.

While the optical properties of the sample are changing, the “probing” of the system's response to the excitation event can be done. To observe a complete picture, there is a need to probe the system over the entire cycle of the system's response to the event. Thus, a weaker probe pulse monitors these changes being triggered in the sample by the pump pulse.

The temporal monitoring of the excited state is investigated by varying the time delay Δt, between the pump and the probe pulses. The way the delay setup works is fairly simple: it deploys a retro-reflector on a rail system only. The retro-reflector position along the rail is directed by a stepper motor being directly controlled by a computer. The retro-reflector, positioned in the path of the probe, moves backwards/forwards and prolonging/shortening the path. This path change is nothing else than a delay time between the pump and probe beams, times light velocity in the medium.

It is important to keep pumping the sample at regular intervals that are longer than the response of the sample to ensure that there is no overlap of excitation events from the current pump and the previous pump (accumulation effect).

The pump-and-probe technique may be deployed in investigations of such properties as: *reflectivity*, *transmissivity*, *Raman scattering*, and *induced absorption.*

2.1.5.2 Other techniques

Streak camera

Streak camera is a device converting temporal information from luminous events into spatial information. This technology pioneering has begun more than three decades ago [30]. In our days, streak cameras are capable to measure optical pulses with subpicosecond resolution. A typical streak camera consists of: a streak tube, fast-sweeping electronics, input optics, and output optics.

Its usage mainly lays in the area of ultrafast luminescence measurements. In this technique light emitted from the sample that is photo-excited by an ultrafast laser pulse is focused onto the photocathode of the camera. The flux of the photoelectrons released by the photocathode is proportional to the light intensity incident on the system. The photoelectrons are accelerated and then deflected by an applied voltage that sweeps the electrons across a phosphor screen. These electrons are released at a different time from the photocathode will strike the phosphor screen at different positions. This will cause a track ("streak") characterised by a spatial intensity profile, directly proportional to the incident temporal intensity profile of the photoluminescence.

Optical Kerr gate

An additional research tool for the ultrafast luminescence area is the optical Kerr gate [31], consisting of a Kerr active liquid, such as carbon disulphide. The liquid fills the place between two crossed polarisers. Normally, in the cross polarisation state, the gate (path) is closed. To open the path, a synchronised with the ultrafast laser pulse intense electric field is applied, forcing the molecules of the liquid to experience a short-lived induced birefringence. This birefringence makes the Kerr gate transparent, acting as a mechanical shutter allowing the light path through for a short time only. Thus, an intense laser pulse can be deployed to pick up portions of the temporal profile of the emitted photoluminescence by varying the delay time of the gating pulse. This can be done by integrating a moveable retroreflector into an optical delay line.

The resolution of the optical Kerr gate depends upon the reorientation time of the molecules of the active Kerr medium, which is typically 2 ps.

Up-conversion gate

The idea of parametric up-conversion (meaning frequency sum generation) has been adopted as a mechanism for ultrafast optical shutters [32]. Following an ultrashort pulse excitation of the sample, resulting luminescence is collected, collimated, and combined with part of the excitation pulse in a nonlinear crystal (for example, $LiNbO_3$). The angle of this crystal is set to phase match the frequency of the gating pulse with a selected frequency of the luminescence. Integrated signal consisting of the laser and luminescence frequencies is generated by the crystal and detected by a photomultiplier tube. Varying the delay of the gating pulse and measuring the integrated frequency signal, the temporal profile of the luminescence is achieved with background-free signal. Because of an involvement of virtual electronic transitions in the up-conversion, the gate has a femtosecond response.

2.2 Technical background

Ultrafast laser-based pump-probe techniques are essential in probing of fast carrier dynamics in semiconductor structures. The following four techniques have been broadly deployed: transient reflectivity and/or transmission [33, 34, 35, 36, 37, 38], transient-grating diffraction including two-beam self-diffraction [39, 40, 41, 42], photo-thermal deflection [43, 44] and time-resolved photoemission [45, 46, 47, 48, 49, 50]. In all of these techniques a relatively strong laser pulse or two crossed pulses in the case of transient grating diffraction excites valence-band electrons into the conduction band. The relaxation of these electrons and/or the redistribution of the excess energy initially contained in these excited carriers is then monitored with a time-resolved probe.

Presented below is the technical background for transient reflectivity measurements in silicon and silicon nano-structures.

2.2.1 Ultrafast pulsed lasers

We have utilised commercial femtosecond laser system from Spectra-Physics, equipped with a *Spitfire* amplifier. The *Spitfire* produces pulses with 100 fs pulse duration around a wavelength of 800 nm and with a repetition rate of 1 kHz. The average output power was up to 1 W. Figure 2.4 shows a sketch of the whole laser system including the *Spitfire* part.

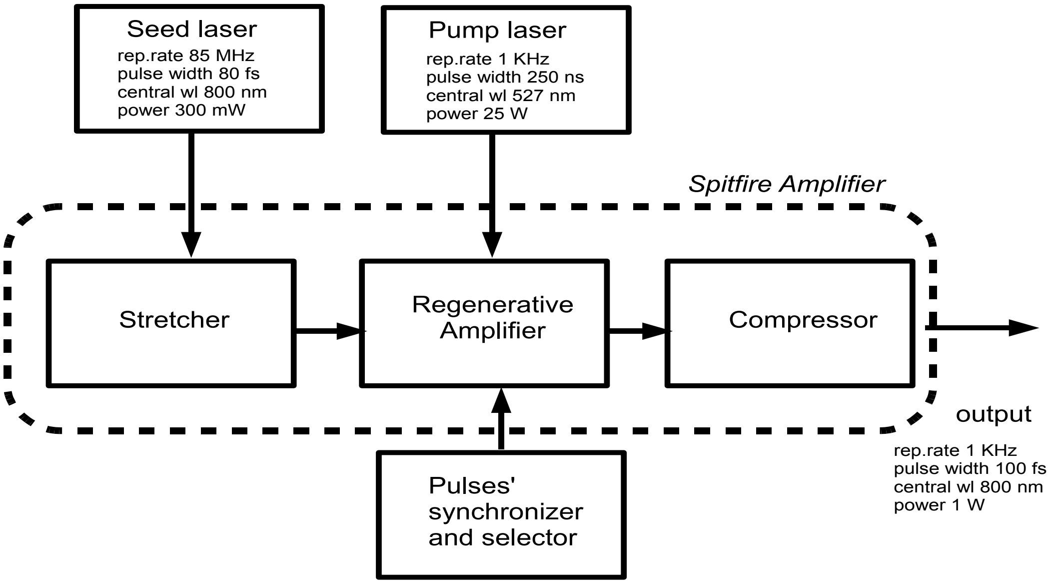

Figure 2.4: Block diagram for femtosecond laser setup including *Spitfire*

The femtosecond laser setup contains the optics and opto-mechanical devices for stretching, selecting amplification and compressing pulses from a seed laser.

Seed laser supplies low intensity femtosecond pulses for further amplification by *Spitfire*. As a seed laser, we have used a mode-locked Titanium-Sapphire *Tsunami* laser supplied by the same maker, generating 80 fs pulses with a repetition rate of 85 MHz and a power of 3.5 nW per pulse. A Titanium-Sapphire crystal has a large gain bandwidth, $660 - 1000$ nm which means it can support femtosecond pulses and a wide tuneable range. The tuneable range of the *Tsunami* is $750 - 850$ nm. An additional advantage of this crystal is its broad absorption band in the blue and green part of the spectrum.

As a pumping laser for *Tsunami* we have used a Nd:YAG laser (not shown in the block diagram of Figure 2.4). The incoming seeding pulses have been stretched in time nearly 1000 times in order to allow intensity amplification by reducing the peak power. Stretching has been possible by means of a grating and a mirror combination. Amplification has occurred in the Regenerative Amplifier area by means of a nanosecond pulsed Pump laser. We have used a *Super Merlin* neodymium-doped yttrium lithium fluoride (Nd:YLF) laser assembled by Spectra-Physics. Its wavelength is 527 nm at a repetition rate of 1 kHz, the pulse duration is 250 ns and the output power is up to 25 W.

The “pulses synchronisation and control” is required to select and capture individual pulses from the train of stretched seed pulses and direct them into the amplifier. Selected and stretched pulses then pass multiple times through the regenerative amplifier. After pulse amplification the “synchronisation and control” unit provides the timing control to direct the amplified pulses into the compressor. The compressor shortens the amplified pulses close to their original duration using a grating/mirror combination in the reverse configuration to that of the stretcher.

2.2.1.1 Diagnostic techniques

The femtosecond time scale is beyond the range of standard electronic display instruments. New methods have to be designed to freeze and time resolve processes as short as a few optical cycles. For example, in our system, an optical cycle corresponding to a wavelength of 800 nm is approximately 2.7 fs.

Discussed below are two main methods to measure an amplitude and duration of a pulse: Intensity and Interferometric correlations [51].

Intensity correlations

The temporal profile $I_s(t)$ of an optical signal can be easily determined, if a shorter reference pulse of known shape $I_r(t)$ is available (practically, it is assumed that $I_r(t)$ has a Gaussian shape with the intensity, polarisation and duration similar to $I_s(t)$ pulse). The method is to measure the intensity cross-correlation: $A(\tau) = \int_{-\infty}^{\infty} I_s(t) I_r(t-\tau) dt$. The Fourier transform of the intensity profile can be defined as $F_j(\omega) = \int_{-\infty}^{\infty} I_j(t) \exp(-i\omega t) dt$, where the subscript j indicates either the reference r or signal s pulse. Thus, the Fourier transform of the correlation $A(\tau)$ related to the intensities is $A(\omega) = F_r(\omega) F_s^*(\omega)$. The shape of the signal $I_s(t)$ can be determined by first taking the Fourier transform $A(\omega)$ of the measured cross-correlation and dividing by the Fourier transform $F_r(\omega)$ of the known reference pulse $I_r(t)$. The inverse Fourier transform of the complex conjugate of the ratio $A(\omega)/F_r(\omega)$ is the temporal profile $I_s(t)$.

Interferometric correlations

For example, for Michelson interferometer measured fields, the correlation is proportional to $G_1(\tau) \propto \int_{-\infty}^{\infty} E_1(t) E_2^*(t-\tau) \exp(iw\tau) dt + c.c.$, where E_1 and E_2 are the electric fields of the separated laser beams. The Fourier transform of the correlation fields is proportional to $E_1^*(\omega) E_2(\omega) + c.c.$. It means that the Fourier transform of the autocorrelation is proportional to the spectral intensity of the pulse. First order field autocorrelation does not carry any other information than that provided by a spectrometer. If we substitute a second harmonic generating crystal (and a filter to eliminate the fundamental harmonic) for the Michelson interferometer detector, we can expect to measure a signal of second order interferometric correlation. This is equal to $G_2(\tau) = \int_{-\infty}^{\infty} [(E_1(t-\tau) + E_2(t))^2]^2 dt$. It can be decomposed into the following second order correlation:

$G_2(\tau) = \mathbb{A}(\tau) + Re\{4\mathbb{B}(\tau)\exp(i\omega\tau)\} + Re\{2\mathbb{C}(\tau)\exp(2i\omega\tau)\}$, where

$\mathbb{A}(\tau) = \int_{-\infty}^{\infty} \{E_1^4(t-\tau) + E_2^4(t) + 4E_1^2(t-\tau)E_2^2(t)\} dt$,

$\mathbb{B}(\tau) = \int_{-\infty}^{\infty} \{E_1(t-\tau)E_2(t)[E_1^2(t-\tau) + E_2^2(t)] \exp(i(\phi_1(t-\tau) - \phi_2(t)))\} dt$,

$\mathbb{C}(\tau) = \int_{-\infty}^{\infty} \{E_1^2(t-\tau)E_2^2(t) \exp(2i(\phi_1(t-\tau) - \phi_2(t)))\} dt$.

This decomposition shows three frequency components of the correlation. They are centred around zero frequency, ω and 2ω, respectively. The detection system of the correlator will act as a low pass filter, leaving only the first term of the expansion. The interferometric correlation reduces then to the sum of a background term and the intensity correlation (such as $\mathbb{A}(\tau)$). Then $\mathbb{A}$, $\mathbb{B}$ and $\mathbb{C}$ can be extracted from experimental data by applying a Fourier transform, selecting data related to the relevant characteristic frequencies and applying inverse Fourier transform.

An autocorrelation is a particular case when $E_1 = E_2 = E$. At $\tau = 0$, the peak value of the function $\mathbb{A}(\tau)$ is $6 \times \int E^4(t)dt$. For delays longer than the pulse duration, the cross product term vanishes, leaving a background of $\mathbb{A}(\infty) = 2 \times \int E^4(t)dt$. Term $\mathbb{A}(\tau)$ of the interferometric autocorrelation (which is an intensity autocorrelation) has a peak to background ratio of 3 to 1. The measurement leading to $\mathbb{A}(\tau)$ is generally referred to as the intensity autocorrelation with background. When all terms of the autocorrelation are recorded, the constructive interference terms at zero delay add to $16 \times \int E^4(t)dt$. The peak to background ratio for the interferometric autocorrelation is 8 to 1.

An autocorrelation of the second harmonic fields defined by $\mathbb{C}(\tau)$, is identical to the intensity autocorrelation for bandwidth limited pulses. As any autocorrelation, the interferometric autocorrelation is a symmetric function. However, as opposed to the background free intensity autocorrelation, it contains phase information.

For qualitative comparison see Figure 2.5. The left panel shows the Intensity autocorrelation and the right panel shows the Interferometric autocorrelation traces for a mode-locked Ti-Sapphire laser pulse after pulse compression. The peak to background ratios of 3/1 and

Figure 2.5: a) Intensity and b) Interferometric autocorrelation traces for the mode-locked Titanium-sapphire laser pulses, from [52].

8/1 for the intensity and interferometric autocorrelations respectively are clearly seen. Figure 2.6 shows a typical, for our setup, intensity autocorrelation profile generated by a second harmonic crystal BaB_2O_4 (BBO) with FWHM = 200 fs (corresponding to a pulse duration of 140 fs).

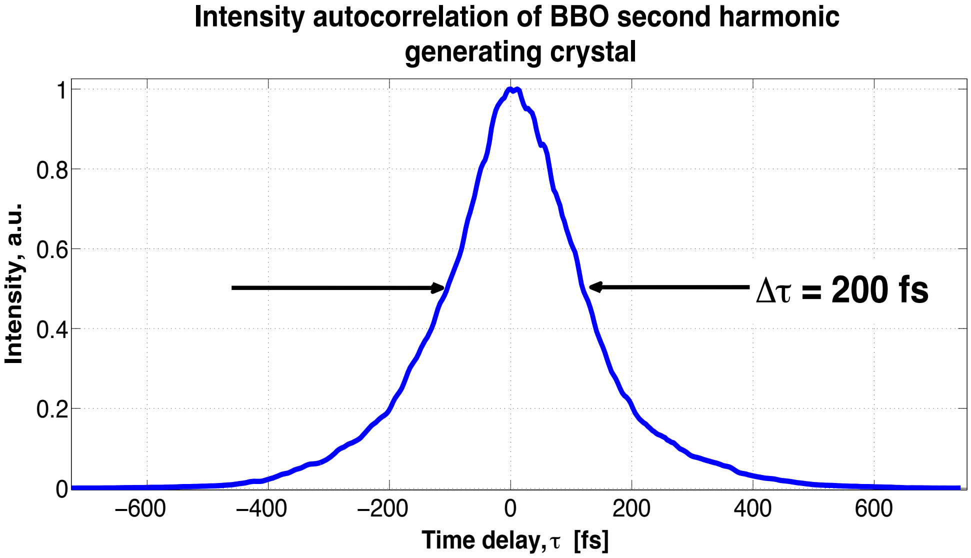

Figure 2.6: Intensity autocorrelation of BaB_2O_4 (BBO) second harmonic generating crystal, profile FWHM is approximately 200 fs, corresponding to a pulse waist of 140 fs.

2.2.2 Experimental setup

The easiest way to describe the experimental setup is to split it arbitrarily into two parts, associated with (*i*) a set of lasers and beams manipulation components and (*ii*) a detection setup providing signal collection and overall control of the measurement process.

2.2.2.1 Lasers and beam handling setup

Figure 2.7 shows a schematic view of the pump-probe time-resolved reflectivity setup. The basic concept of this femtosecond laser system is already described above. The amplifier produces p-polarised pulses of approximately 100 fs duration, 800 nm wavelength and intensity of 1 W. The output beam is split into two equal parts when passing through the beam splitter. Now, one beam passes through an additional path, whose length is controlled by a delay stage, this line is called the “probe”. Next step is polarisation rotation to the s-polarisation state and intensity attenuation by sequential set of of “half wave plate - linear polariser- half wave plate”. In the same manner, the second beam, “pump” beam - which remans fixed on its optical path, is intensity controlled by the similar set of “half wave plate - linear polariser- half wave plate”. Its polarisation remains p-polarised and any s-polarised component is filtered out. The half wave plate in each set allows intensity control of the outgoing beam. A long focus lens, adjustable mirrors and CCD camera (not shown) provide means to achieve spatial overlap of the two beams on the sample surface. The diameter of the focused beams is approximately $\sim 70\ \mu$m.

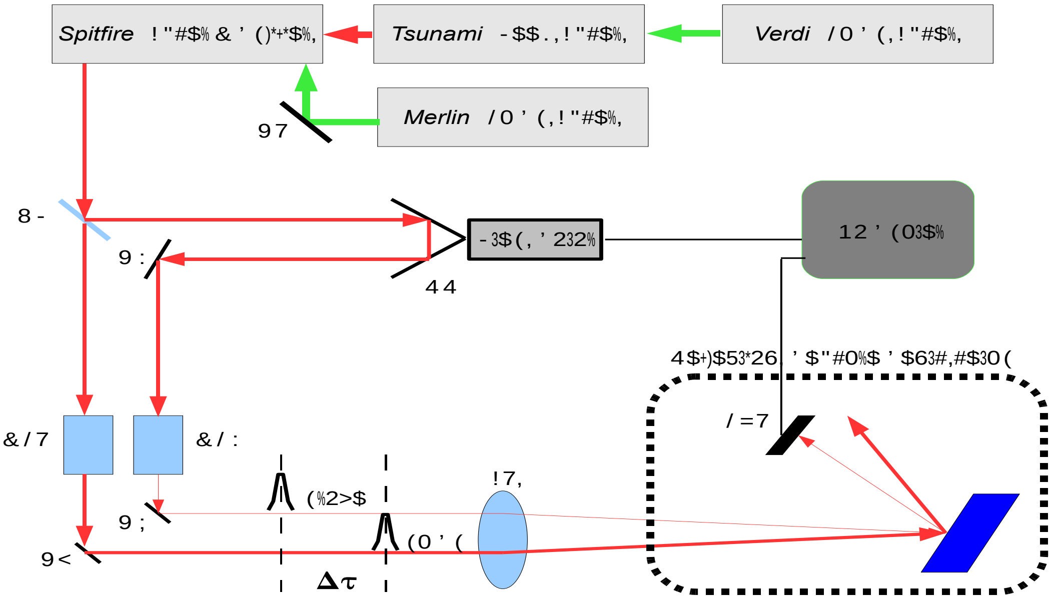

Figure 2.7: Schematic view of the lasers setup for pump-probe reflectivity measurements. Description: M1-M4 mirrors, BS beam splitter, L1 long focus lens, RR step motor based retro-reflector, AP1 and AP2 sets of attenuator and linear polariser. See Figure 2.8 for more details.

2.2.2.2 Signal detection setup

Figure 2.8 shows, in more detail, a schematic view of the pump-probe time-resolved reflectivity measurements setup. A couple of highly sensitive to the infrared radiation silicon pre-amplified photodiodes have been utilised. One of them has been used to monitor power fluctuations by introduction of a fused silica wedge with a diffraction angle of $2°48'$ (to deflect a small part of the probe beam towards the detector). Here, the assumption is that the source of any intensity instability is the laser system, meaning there is no need to monitor the pump beam as they come from the same source. The second photodiode provides detection of the reflected probe beam from the spot on the sample surface being excited by the pump beam.

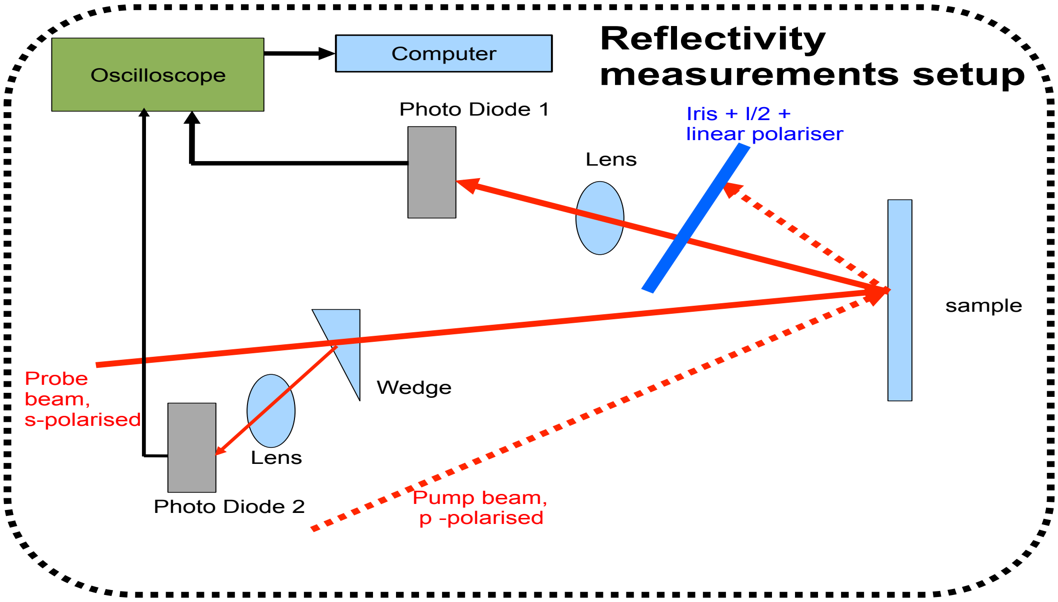

Figure 2.8: Schematic view of the detection electro-optical setup for pump-probe reflectivity measurements. See Figure 2.7 for general view.

In order to cancel unwanted specular and diffused reflection of the pump beam, a set of beam block (iris), half wave plate and linear polariser have been introduced and optimised to the polarisation state of the reflected probe beam. This method allowed us measurements of pump intensity up to twice the threshold intensity, while the probe beam remains two orders of magnitude smaller (which is a required condition for probing without any affect on the excited carriers population).

Signals from both photodiodes have been averaged by a digital oscilloscope and synchronised with the delay stage by home written programs based on *Labview* interface.

2.2.3 Samples

This experimental work has been done on two different silicon nano-structures: crystalline silicon Nanopillars and nano-crystalline silicon inclusions in an amorphous silicon layer. In order to compare measured results we have conducted similar reflection measurements on undoped bulk silicon samples.

2.2.3.1 Undoped crystalline silicon

The undoped silicon wafers were purchased from *Virginia Semiconductor Inc*, VA, USA. Main specifications are:

Surface - double side polished,
Orientation - $< 100 >$,
Oxide thickness - native oxide,
Resistivity - 20 $\Omega \times cm$.

2.2.3.2 Silicon Nanopillars

This sample was provided by B. Lamontagne, *Department of Engineering Physics, Ecole Polytechnique*, Montreal, Quebec, Canada. A nano-imprint assisted dry-etching procedure was employed to fabricate the silicon nanopillars on *Silicon on Insulator* (SOI) substrate as schematically shown in Figure 2.9. Density of the nano-pillars in the nano-mask was $2.5 \times 10^9\ cm^{-2}$. Dry-etched Pillars were slightly oxidised to a depth of approximately 3-5 nm. Figure 2.10 shows Scanning Electron Microscope (SEM) pictures of the sample at various magnifications. Highly ordered structure of nanopillars is well resolved and the following average dimensions are observed: pillar diameter approximately 70 nm and height approximately 200 nm.

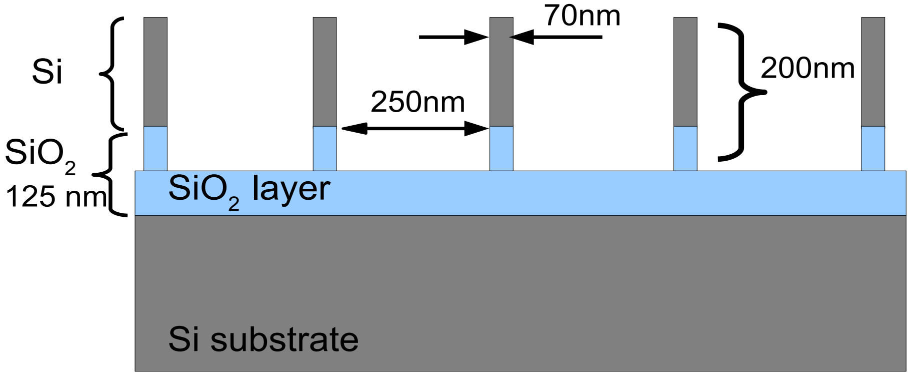

Figure 2.9: Schematic view of Silicon Nanopillars structure.

2.2.3.3 Nano-crystalline silicon inclusions

This sample was produced and investigated by E. Vallat-Sauvain *et al.* [53] as a part of solar cells research. Nano-crystalline formations were grown in amorphous silicon (α-Si) matrix by means of plasma deposition of silane SiH_4 and hydrogen H_2. According to the authors, the shape of this nano-structure can be controlled by a ratio of the deposition gases rate flow, $[SiH_4]/[SiH_4 + H_2]$ as shown in Figure 2.11(a). X-rays and Raman analysis of our sample, carried out elsewhere [78], has shown the nano-crystalline concentration to be 35% in the host layer at an average particle's dimension of 6 ± 2 nm. A schematic view of the sample

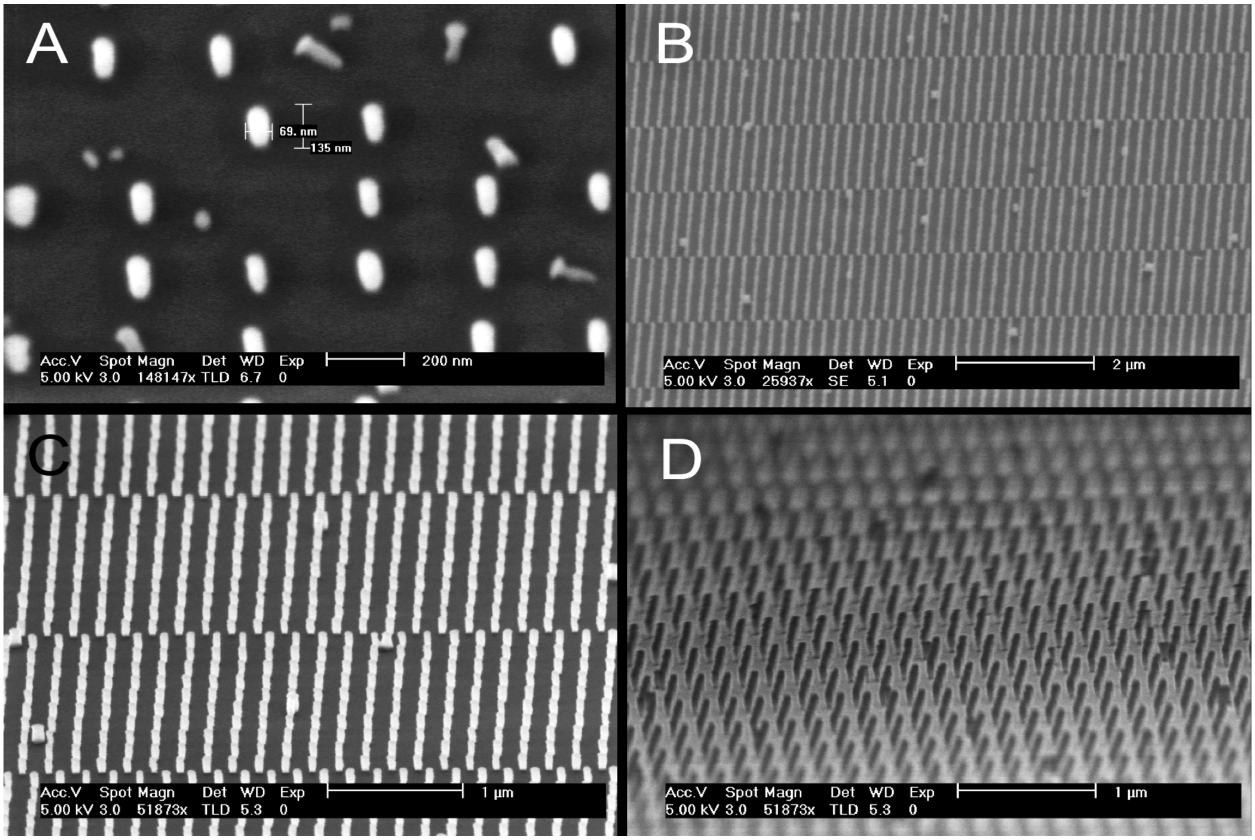

Figure 2.10: SEM pictures of silicon nanopillars made by imprint method. A) 45° tilted view, scale bars = 200 nm, pillar size estimation: 70×200 nm, B) 50° tilted view, scale bars = 2 μm, C) 50° tilted view, scale bars = 1 μm, D) 85° tilted view, scale bars = 1 μm.

structure is shown in Figure 2.11(b). The structures are grown on SiO_2 dielectric layer on top of a silicon substrate.

2.2.4 Main experimental challenges

Low signal-to-noise ratio has played major technical constrain. As it follows from the name, the signal detection issue arises mainly from a couple of sources: an instability of the laser beam ("noise") and weak response ("signal") to the excitation of particular samples. Described below is a critical overview of the deployed system in more detail.

2.2.4.1 System instability

The nominal pulse to pulse stability of the *Spitfire* amplified pulses is below 3%, this is governed mainly by the "multistage amplification" design. Basically, it means that any noise

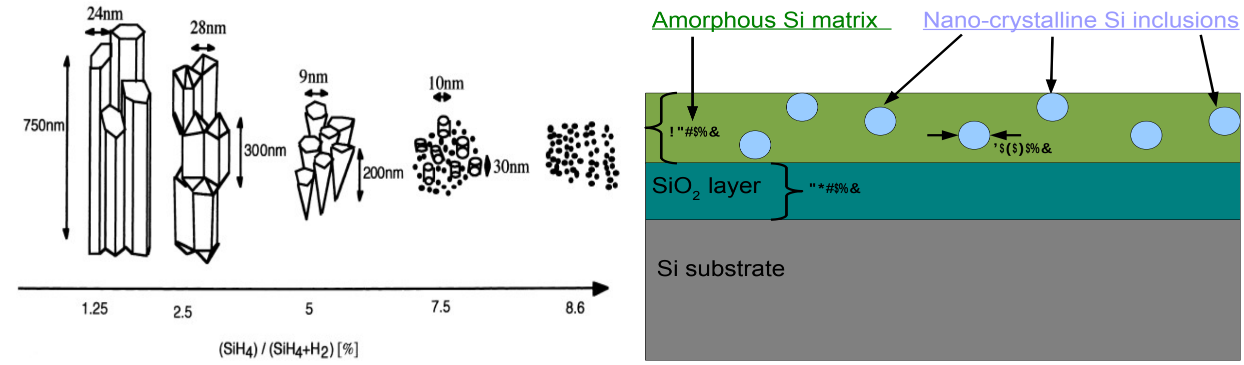

(a) (b)

Figure 2.11: (a) Schematic representation of the evolution of the microstructure of the layers as a function of the silane concentration in the plasma gas phase. The small black dots represent the amorphous phase, from [53]. (b) Schematic view of microcrystalline silicon inclusions structure.

in the first stage will be amplified in the second stage on so on. Furthermore, this laser system has been deployed for over ten years and, despite the frequent alignment services, the efficiency of some parts is degraded. For example, burned high-voltage polarisers (Pockels cells), dust particles flow in the air inside the amplifier box (absence of quasi clean room conditions), unremovable dust accumulated on the large gold gratings' area (being used for stretching and compression of pulses). The highest efficiency in stability of pulse amplification can be reached when the system is saturated, requiring full-power operation of the pump laser (see Figure 2.4). However, this laser has permanent cooling problems and such conditions can not be fulfilled.

As a partial solution of these difficulties, beam intensity monitoring was introduced by means of pulse averaging in real time and each experimentally measured data point was normalised respectively, see Figure 2.8.

Inappropriate optical path

Additional disadvantage of the setup is five meters long optical path. This length was completely unnecessary in the case of reflection measurements but unavoidable due to sharing the beam lines with another experimental setup. In fact, any small beam distortion at the beginning of the path (for example as a result of an optics heating) caused a significant reduction in the signal amplitude because of mismatching of the small photodiode active area (a few mm^2). As a solution, we introduced additional focusing lenses in order to keep the signal and reference beams fixed on the small area of photodiode sensors.

In addition, the maximum delay time range was limited by a distortion caused by movement of the electro-mechanical delay stage of the probe arm. The experimentally acceptable delay range was approximately 100 ps.

Signal-to-noise ratio

Signal beam (reflected from the sample) coupled with the reference beam (reflected from the wedge) have been averaged by means of a digital oscilloscope, providing a decreased in the noise level from 10% down to 1% only during a minute time. However, setting much longer oscilloscope averaging time prolonged the overall experiment while the seed laser required frequent readjustment.

2.2.4.2 Limited sample response

Response of bulk silicon sample to even the highest sub-threshold intensities (less than 170 mJ/cm^2) was marginally above the detection resolution of the system. According to Eq. 2.12 $\Delta R \propto \Delta N$, where $\Delta N = N_v - N_c$ and N_v and N_c are the carrier densities of the valence and conduction bands, respectively. A rough estimation for bulk silicon shows that $N_c/N_v \approx 10^{21}/10^{23} = 0.01$ or 1% ($N_c = \alpha F/\hbar\omega$, where α is an absorption coefficient and F denotes an excitation flux at the energy $\hbar\omega$). The biggest change in reflectivity, due to excited carriers, was about 2% when the system resolution was about 1% only. That is the reason for absence of reflection measurements on silicon under low intensity excitation which, however, are well presented for other samples.

2.3 Experimental results

This section is mainly focused on the femtosecond-resolved changes in reflectivity from silicon-based nano-structures exposed to a strong femtosecond excitation. The nano-structures are Silicon Nano-Pillars and amorphous Silicon embedded Nano-Inclusions. Background or substrate measurements will be presented from the relevant materials: undoped/bare balk silicon and amorphous silicon thin film.

2.3.1 Absolute reflection

To understand time-resolved results, there is a need to know absolute (known as total) reflection R_0 values for each of the investigated samples. The measurements were done in the spectral region of $750 - 850$ nm by means of the *Tsunami* laser operating in CW mode, benefiting from high-power stability. Figure 2.12 shows the results of R_0 measurements in this range. Figure 2.12 (a) clearly shows that the absolute reflection value of undoped crystalline Si at 800 nm is approximately 0.32 ± 0.01 and well corresponds to the previously published value of 0.3 ± 0.01, for example [24].

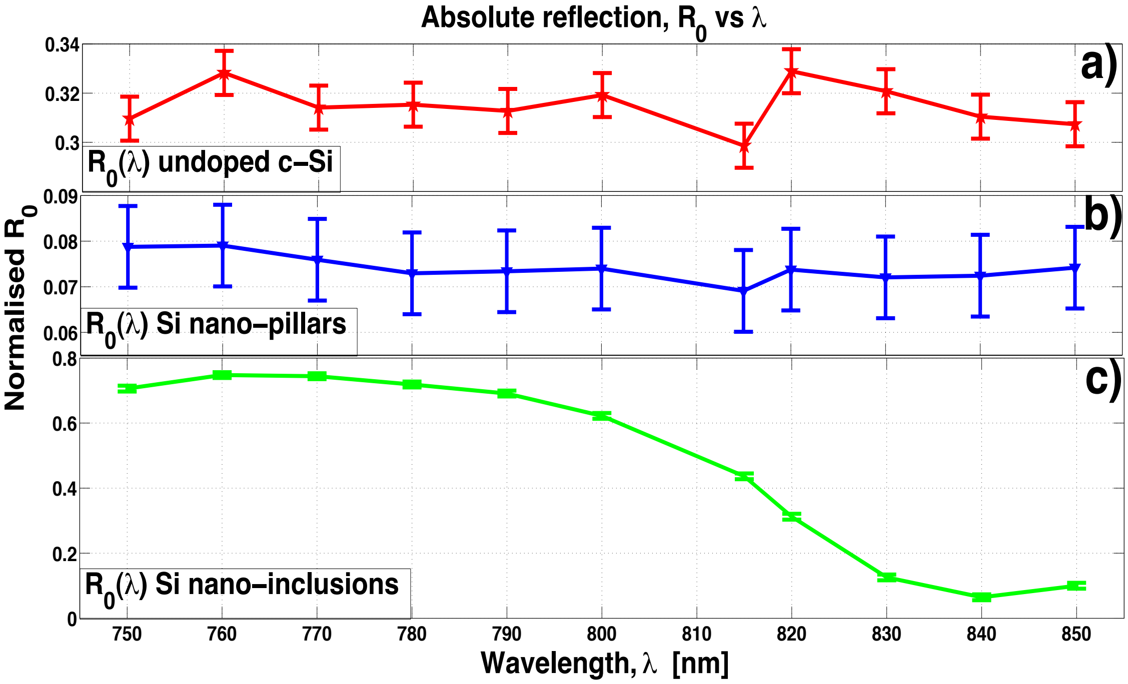

Figure 2.12: Absolute reflection, R_0 vs wavelength, λ of: a) undoped crystalline silicon, b) silicon nanopillars, c) silicon nano-inclusions. Note: different scales on plots.

Shown in Figure 2.12 (b) are results of R_0 of silicon nanopillars, the absolute reflection value at 800 nm is about 0.074 ± 0.01. This low value is in good agreement with other works on nano-pillar structures dedicated to an anti-reflecting coating [54, 55] and photonic-band-gap [56]. According to Landau [57], an array of dielectric ellipsoids can be regarded within an effective medium approximation. A "mixture" of crystalline silicon pillars, with known dimensions, and a medium (air) act as a layer with optical properties (such as refractive index) driven, in particular, by the physical dimensions of the nanopillars. Matching refractive indices of such effective layer and a substrate can lead to low reflectivity (anti-reflecting coating) at corresponding wavelength band.

Figure 2.12 (c) shows results of R_0 for Si nano-inclusions embedded into an amorphous silicon layer of approximately 510 nm thickness. Due to the layered structure, it is possible to recognise a part of an oscillation of R_0 versus wave length, λ (note, the periodic oscillations occur in the reciprocal space, $1/\lambda$). In addition, this sample was scanned by other means [58] in a wider range of $200 - 2000$ nm and a clear interference picture was observed, see Figure 2.19. The mean value of R_0 at 800 nm could be estimated as 0.4 which fits well to the published value [24] of 0.375 for amorphous silicon, at the same wavelength. The actual value of R_0 at 800 nm is approximately 0.6.

2.3.2 Time-resolved reflectivity from undoped crystalline silicon

The time-resolved reflectivity, $R(\tau)$, presentation begins with the results obtained from bulk undoped Si sample. Temporal variable, τ, denotes the delay time between pump and probe. Figure 2.13 shows the change in the time-dependent reflectivity $\Delta R/R_0$, where $\Delta R \equiv R(\tau) - R_0$. Here, R_0 is the unexcited value of $R(\tau)$ when $\tau \ll 0$ (much earlier than an arrival of the excitation pulse). The upper panel of this figure shows this change corresponding to various fluencies (F) of the pump pulse in units of the silicon damage threshold (melting) fluence, F_m, which is determined experimentally to be 170 mJ/cm^2. Each curve represents a different physical point on the sample surface. The lower panel shows the same measurement carried out at a single place on the sample's surface.

Each curve might be split into three time regions. The first one is prior to excitation between -1500 and roughly -500 fs, where no change in $R(\tau)$ occurs. The second region corresponds to changes in $R(\tau)$ during the excitation time. Excitation (fall) time might be estimated from the full pulse width at a half maximum (FWHM) being approximately $150 - 200$ fs. The last region begins when the excitation pulse is "switched off" and the

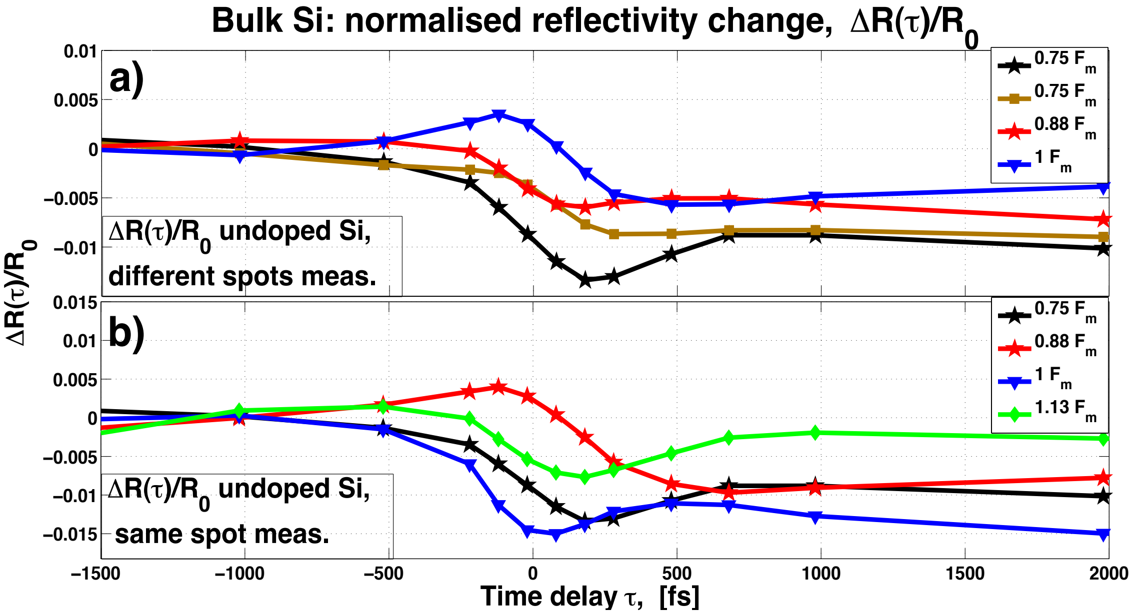

Figure 2.13: Normalised change in the time-resolved reflectivity of undoped crystalline silicon in the vicinity of the melting fluence, F_m: a) randomised probing, b) same spot probing.

excited carrier population undergoes thermalisation with the lattice, followed by electron-hole recombinations.

The overall maximum $|\Delta R/R_0|$ value does not exceed 1.5%, while the experimental sensitivity has been about 1%. As a result, there is no clear signal repeatability and fluence dependence in the vicinity of the melting threshold and phase transition. This occurs despite the fact that the plasma frequency exceeds the probing frequency, growing an imaginary index of refraction and changing the sign from negative to positive of the full free carriers contribution to $R(\tau)$, see Eq's. 2.5 and 2.13.

2.3.3 Time-resolved reflectivity from silicon nanopillars

In this section results of $R(\tau)$ measurements on the sample containing silicon nanopillars have been presented. The absolute reflection, R_0, broadly speaking, is four times less than one from the flat surface undoped Si sample, see Figure 2.12.

2.3.3.1 Time-resolved reflectivity below melting fluence

Figure 2.14 shows the change in $R(\tau)$ recorded at consecutive pumping fluence values below the melting threshold, F_m. Each fluence is depicted in F_m units of bulk Silicon. $\Delta R/R_0$ transients show a clear dependence on the pump fluence. $\Delta R/R_0$ magnitude reaches approximately 8% at near the threshold fluence of 0.94 F_m. This value happens with a delay time of 1 ps after the excitation pulse. Here and later on, we determine zero delay time, $\tau = 0$, as the centre of the pump pulse.

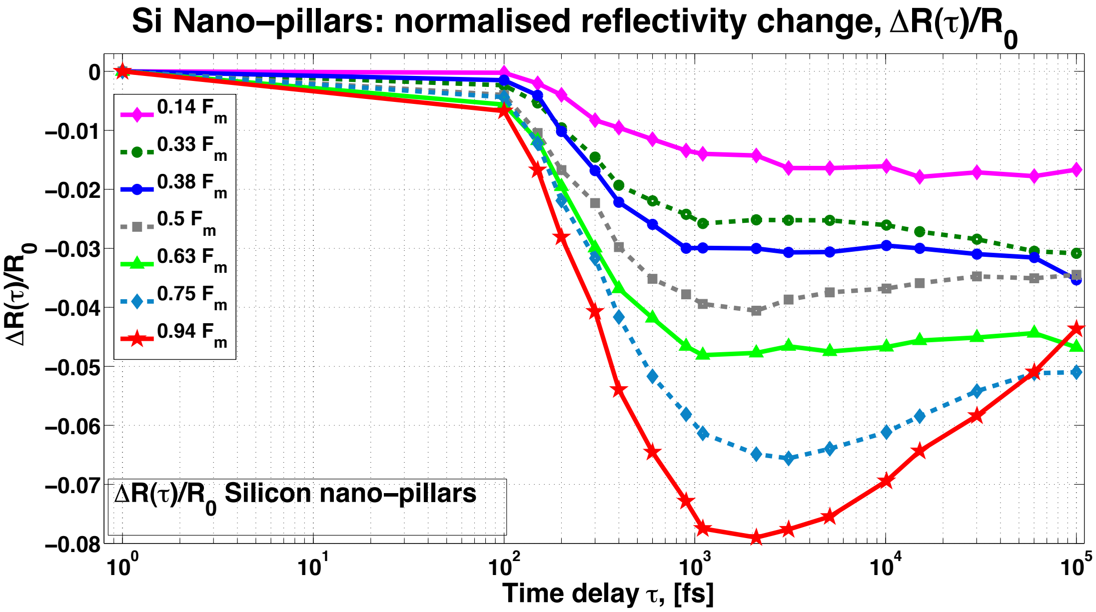

Figure 2.14: Normalised change in the time-resolved reflectivity of silicon nanopillars below the melting fluence, F_m.

The negative sign of the observed $\Delta R/R_0$ corresponds to the contribution of free carriers absorption to the dielectric function. According to Eq's. 2.5 and 2.13, $\Delta R \propto \Delta n \propto -(\omega_p/\omega)^2 \propto -N_{e-h}$. Thus, an increase of the plasma density, N_{e-h} leads to the decrease in the reflectivity.

2.3.3.2 Time-resolved reflectivity in the vicinity of melting fluence

Figure 2.15 shows changes in $R(\tau)$ at a fluence of $F = 1\ F_m$ which is attributed to a melting of the surface and phase transition. Melting leads to an irreversible surface damage, which is confirmed by the later sample's surface check. For comparison, representative data from the sub-melting regime (already depicted in Figure 2.14) is presented. The depicted melting curve corresponds to the fluence magnitude of 0.16 J/cm^2. The melting fluence of silicon at 800 nm is known to be 0.17 J/cm^2, for example [23]. The positive change in $R(\tau)$ is about 18% and its maximum occurs at the delay time of approximately 1 ps. This variation becomes noticeable at τ = 200 fs when initially negative reflectivity change (according to the Drude model, when $\omega_p/\omega < 1$) alter its behaviour due to a structural phase transition from solid to liquid.

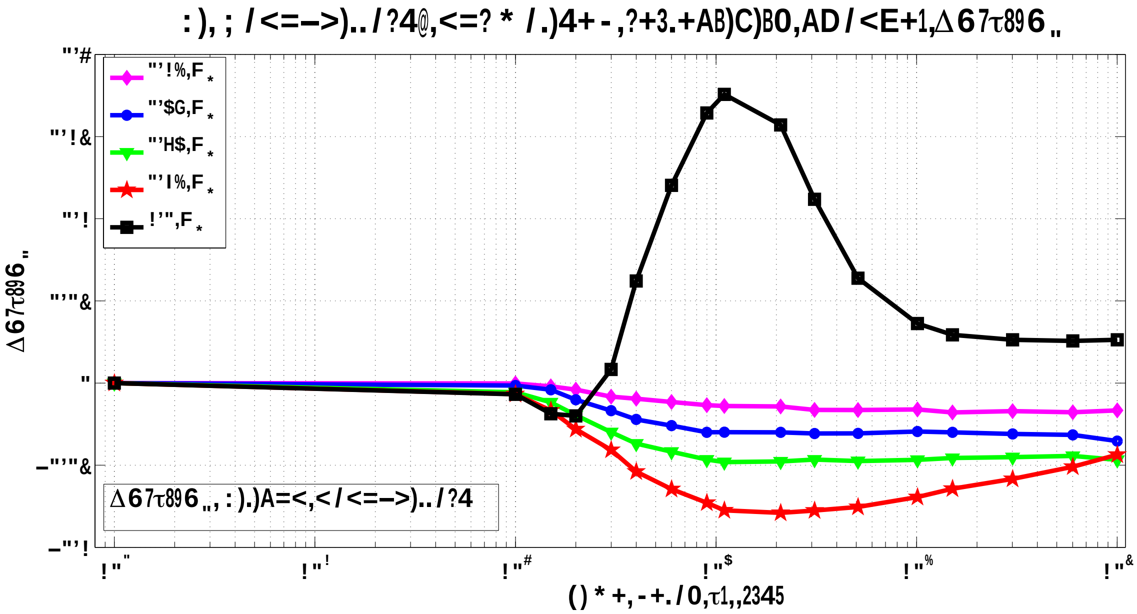

Figure 2.15: Normalised change in the time-resolved reflectivity of silicon nanopillars in the vicinity of the melting fluence, F_m. The black curve represents affected by the surface melting (variation in) reflectivity.

2.3.4 Time-resolved reflectivity from crystalline silicon nano-inclusions

Presented below are investigated results of another nano-structured sample - nano-crystalline silicon inclusions in an amorphous silicon (α-Si) layer. Figure 2.16 shows a time-resolved reflectivity, $R(\tau)$ for two samples: Si nano-inclusions in an amorphous layer and α-Si only. Both measurements have been done at a fluence of $F = 0.25\ F_m$. It was technically impossible to resolve any meaningful change in $R(\tau)$ of α-Si, while $\Delta R/R_0$ of the nano-inclusions was up to 8%. This fact allows us to believe, that the origin of such relatively strong change in $R(\tau)$ comes from the crystalline silicon nano-inclusions rather than from the host material and the silicon substrate.

Figure 2.16: Time-resolved reflectivity of Si nano-inclusions and amorphous Si, α-Si below a melting fluence, F_m.

2.3.5 Excitation and response time

In order to follow the response of the excited nano-structures to the excitation pulse, the following presentation has been adapted. Figure 2.18 shows a normalised (to minus unity) change of the time-resolved reflectivity $\Delta R/|\Delta R_{max}|$. Where $|\Delta R_{max}|$ denotes the absolute value of the maximum ΔR in the vicinity of zero delay time (up to the first few ps). Such rescaling makes the comparison of the time dependent $\Delta R/R_0$ between samples easier and more obvious. In addition, a schematic presentation of the 200 fs autocorrelation profile, measured by a photo-excitation of the second harmonic generating crystal, was depicted by the black dashed curve. A resulted $\Delta R/|\Delta R_{max}|$ of the nano-inclusions is presented by the green curve and two results of the nanopillars are depicted by the blue and red curves accordingly. All measurements were carried out at a fluence of 0.6 F_m. The nanopillar sample has a lower signal-to-noise ratio than the nano-inclusion sample. The uncertainty in τ might be up to ± 100 fs. However, within the experimental accuracy, it is possible to notice that the nanopillars sample achieves the excitation minimum in slightly longer time than the inclusions sample.

Figure 2.18: Net change in the time-resolved reflectivity of silicon nano-inclusions, *Si NI* and nanopillars, *Si NP* at the same fluence, 0.6 F_m. Pump pulse is depicted as a result of second harmonic generation measured from second harmonic generating crystal. The nano-structures sample shows slightly shorter excitation response ("fall time"), than the nanopillars sample.

2.4 Analysis and discussion

The following discussion will be focused on the role of a multilayer interference in the high value of the $|\Delta R|$ of the amorphous silicon-based nano-inclusions sample. Relaxation and recombination characteristic decay times will be presented for both nano-inclusions and nanopillars samples utilising the Drude model.

2.4.1 Silicon nano-inclusions

2.4.1.1 Interference phenomena

Constructive (and destructive) interference in a layered structure might affect the reflection value, as follows from Eq. 2.14. Inspired by a simple one layered structure, we would like to discuss the possibility to change a value of the absolute reflection, R_0, by modifications in the interference conditions followed by the carrier photo-excitation. Thus, adopting the undamped Drude model, Eq. 2.5 will be transformed into

$$n_p = n\sqrt{1 - \omega_p^2/\omega^2} \Longrightarrow n_p(t) = n + \delta n(t) \approx n - \omega_p^2/2\omega^2 = n - \frac{(2\pi ec)^2}{2\epsilon_0 m_{eff}} \times \frac{N_{e-h}(t)}{\lambda^2} \quad (2.15)$$

where $\delta n(t)$ reflects changes in n_p due to the free carries absorption. For simplicity, an effective electron mass, m_{eff}, is kept independent on the excited (free) carriers density N_{e-h}. The upper panel of Figure 2.19 shows experimentally investigated [58] reflection behaviour from the SiNI sample for a broad spectral range, as depicted by the red line. The interference phenomenon is well resolved. Now, let us have a look at any sharp slope of this curve, for example at $\lambda = 800$ nm. A small change in optical properties of the investigated material might cause a non-negligible change in the reflection due to the high $\partial R/\partial\lambda$ value in this range.

Utilising Eq's. 2.5 and 2.14 the interference affected reflectivity has been calculated assuming an absence of absorption in the "$air - \alpha\text{-}Si - SiO_2$" layered structure. The assumed effective carrier mass according to [27] was set to $m_{eff} = 0.2\ m_e$. Values of the relevant refractive indexes were taken at $\lambda = 800$ nm, which makes simulation results mostly realistic in the vicinity of this wavelength. Results of the simulation of reflection from "$air - \alpha\text{-}Si - SiO_2$" structure are depicted by the green, magenta, blue and black colour curves for the carrier densities of $N_{e-h} = 0$, 1×10^{19}, 1×10^{20} and 3×10^{20} cm^{-3}, respectively. It is easy to notice, that value of the reflectivity changes drastically with the carrier density (for example, at $\lambda = 800$ nm).

Figure 2.19: Upper panel: Reflection from Si nano-inclusions as measured [58] (red curve) and simulated for $air-\alpha\text{-}Si-SiO_2$ layered structure based on the Drude model of e-h plasma for various carrier densities. Lower panel: simulation of e-h plasma affected refractive index, n_p, of $\alpha - Si$ upon wavelength for various carrier densities.

There is a need to emphasise a sensitivity of the interference conditions to the carrier density. The lower panel of Figure 2.19 shows calculated, ignoring absorption, spectrally dependent refractive index $n_p(\lambda)$ of the α-Si layer for a number of carrier densities, according to Eq. 2.5. These densities are similar to those which have been used in simulations shown in the upper panel of Figure 2.19. The decrease in the value of n_p is a direct prediction of Eq. 2.5. When $n_p = 0$ the complex refractive index becomes pure imaginary (not shown).

Since the central wavelength of the excitation pulse is at $\lambda = 800$ nm, we would like to analyse qualitatively the reflection dependence on the carrier density and film thickness at this wavelength only. Figure 2.20(a) shows such simulations. Presented in the upper panel is the reflection dependence on the carrier concentration for various film thicknesses. It is easy to recognise beatings of the reflection in the region of $N_{e-h} \approx 10^{18} - 3 \times 10^{20}$ cm^{-3}, with corresponding plasma frequency of $N_{e-h} \simeq 3.5 \times 10^{20}$ cm^{-3} (sharp increase in right part, when the refractive index becomes pure imaginary). The density region where reflection exhibits these beatings overlaps with the experimentally achieved density values. According to our estimations, $N_{e-h} \geq \times 10^{20}$ cm^{-3} is related to the fluence of $F = 1\ F_m$. The relation between N_{e-h} (just after the relaxation to the bottom of the conduction band [37]) and F is linear and described as $N_{e-h} = F(1-R)\alpha/\hbar\omega$. Here α denotes a linear absorption coefficient. Furthermore, value of an unexcited reflection, R_0, is strongly dependent on the film thickness as can be seen from the lower panel of Figure 2.20(a). A three-dimensional (3-D) simulation of the reflection dependence on the film thickness, d, and carriers density, N_{e-h}, is depicted in 3-D presentations in Figure 2.20(b). The value of R is given in percents.

In summary, the high value of $|\Delta R|$ is explained due to the strong $R(N_{e-h})$ dependence taking place when $|\partial R/\partial \lambda|$ is sufficiently high due to the interference occurring in the multilayered structure. Broadly speaking, an absolute reflection, R_0, value can be strongly modified (e.i. either amplified or cancelled) by relatively small variation of one of the following: layer(s) thickness (for example, piezoelectric material), incoming wavelength and free-carriers density (by changing intensity of the second beam, pump excitation).

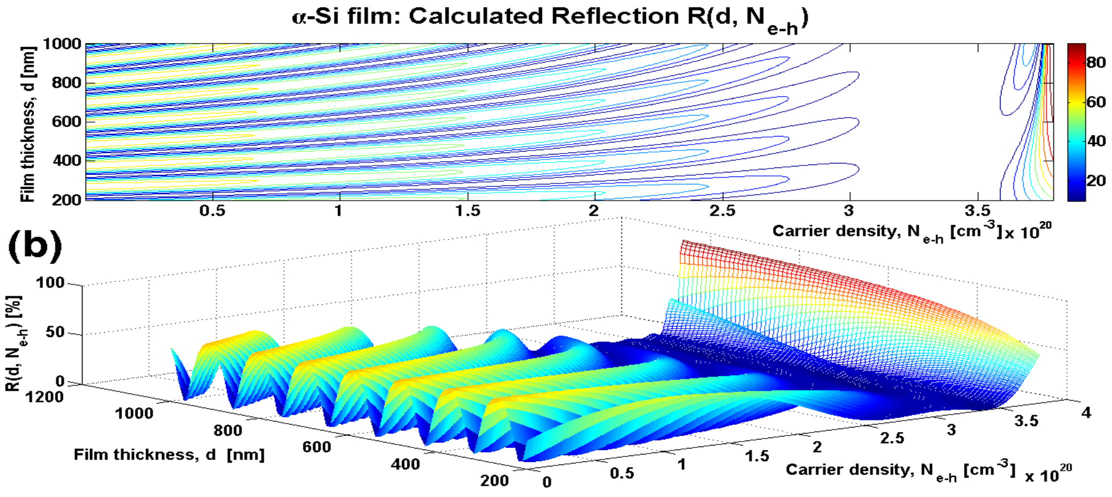

Figure 2.20: Simulation of reflection value at $\lambda = 800$ nm from air - α-Si - SiO_2 layered structure based on the Drude model of e-h plasma: (a, i) as function of carrier density at various film thickness values, (a, ii) as function of film thickness at $N_{e-h} = 10^{14}$ cm^{-3}. (b) 3-D view, colour bar reflects magnitude of reflection in percents.

2.4.1.2 Electron-hole plasma cooling and crystal thermalisation

We would like to deduce typical recombination and electron-phonon interaction times by means of the following empiric equation, deployed by Sabbah *et al.* for analysis of the femtosecond carrier dynamics in silicon [27]. This model describes the free carrier temperature dependent contribution, $\Delta R_{FC}(\tau)/R_0$ to the total change in reflectivity, $\Delta R(\tau)/R_0$, defined as

$$\frac{\Delta R_{FC}(\tau)}{R_0} = \int_{-\infty}^{\infty} |E_x^p(t-\tau)|^2 dt \times \int_{-\infty}^{t} A_{FC}(t-t')|E_y^e(t')|^2 dt', \tag{2.16}$$

where $E_x^p(t)$ and $E_y^e(t)$ are the (envelope) electric fields associated with the probe and excitation pulses, respectively and τ is the time delay between them. Both pulses could be approximated by Gaussian function ($E(t) \propto \exp(-(t/\tau_p)^2)$), where τ_p is $2\ln(2)$ times the time duration at the FWHM of the pulse. The response function $A_{FC}(t)$ is defined as

$$A_{FC}(t) = -A_{FC}^0 \frac{1}{1+(m_{1985}^*/m_{300}^* - 1)\exp(-\tau/\tau_{e-ph})} \frac{1 + C\exp(-\tau/\tau_r)}{1+C}. \tag{2.17}$$

Here $-A_{FC}^0$ denotes the initial magnitude of the response function. Hot carriers equilibrate with the lattice within time τ_{e-ph}, which represents the effective electron-phonon interaction time. The carrier temperature dependence is introduced by means of the effective optical mass, $m^* \equiv (1/m_{eff} + 1/m_{heff})^{-1}$, where m_{eff} and m_{heff} are host effective masses of electrons and holes, respectively. Thus, the initial room temperature carrier optical mass is $m_{300}^* = 0.156\ m_e$ and the optical mass at the assumed maximum temperature of approximately 2000 K is $m_{1985}^* = 0.205\ m_e$. The last term of the above equation describes *e-h* recombination, that can be approximated by an exponential decay with τ_r the effective recombination time and C a model fitting parameter.

Assuming Gaussian form for the electric fields and conditions of $\tau_p \ll \tau_r$ and $\tau_p \ll \tau_{e-ph}$, Eq.2.16 could be approximated to the following form:

$$\frac{\Delta R_{FC}(\tau)}{R_0} = \frac{\Delta R_{FC}^{max}}{R_0} \frac{(erf(\tau/\tau_p)+1)/2}{1+(m_{1985}^*/m_{300}^* - 1)\exp(-\tau/\tau_{e-ph})} \frac{1+C\exp(-\tau/\tau_r)}{1+C}. \tag{2.18}$$

The first term, $\frac{\Delta R_{FC}^{max}}{R_0}$ represents a maximum change of the reflectivity.

The upper panel of Figure 2.21 shows such $\Delta R_{FC}(\tau)/R_0$ fit to the experimental $\Delta R(\tau)/R_0$ data. According to this fit, the recombination time is around $\tau_r \approx 9$ ps. The electron-phonon interaction time is found to be $\tau_{e-ph} \approx 300$ fs in agreement with published values for crystalline Si at similar conditions: 240 fs [20] and 400 fs [59]. A pulse width of the excitation time is $\tau_p = 150$ fs, $\frac{\Delta R_{FC}^{max}}{R_0}$ scales to -0.5 and the fitting parameter is $C = 4$.

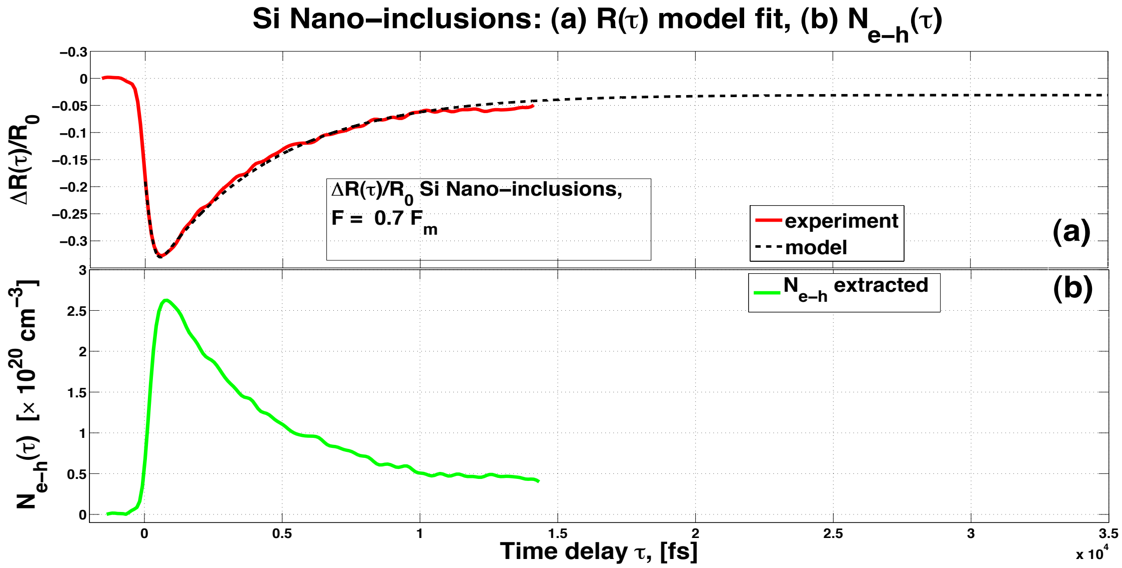

Figure 2.21: Upper panel: change in time-resolved reflectivity of Si nano-inclusions, experimentally measured and fitted using the free carrier model. Lower panel: time-resolved carriers density extracted from measurements of reflectivity (upper panel) using undamped *e*-*h* plasma model.

The lower panel shows carrier density as a function of the delay time. It was extracted from experimental data, depicted in the upper panel, utilising relations between $\Delta R(\tau)/R_0$ and N_{e-h}, determined by Eqs. 2.5 and 2.13. The *e*-*h* plasma is regarded within the undamped Drude model (see Eq. 2.5).

2.4.2 Silicon Nanopillars

2.4.2.1 Suppressed diffusion process in Silicon Nanopillars

In order to analyse the temporal parameters of the $\Delta R(\tau)/R_0$ experimental data, we have adopted the already mentioned free carrier model described by Eq. 2.18. The upper panel of Figure 2.22 shows experimental results obtained at fluence $F = 0.6\ F_m$. The dashed line represents the fit of the $\Delta R_{FC}(\tau)/R_0$ contribution to the experimental curve. The extracted carrier density dependence on delay time, $N_{e-h}(\tau)$ is presented in the lower panel of Figure 2.22. It was estimated using the Drude model describing an undamped electron-hole plasma, see Eq. 2.5. According to this fit, the electron-hole recombination time is $\tau_r \approx 700$ ps and the electron-phonon interaction time is $\tau_{e-ph} \approx 300$ fs. The pulse excitation time is $\tau_p = 150$ fs, $\frac{\Delta R_{FC}^{max}}{R_0}$ scales to -0.103 and the fitting parameter is $C = 100$.

It was impossible to fit the experimental data corresponding to fluences below 0.75 F_m

The left panel shows the dependence of the recombination time, τ_r on the plasma density, N_{e-h} depicted by the black and red curves for nanopillars and nano-inclusions respectively. The recombination time of the nano-inclusions sample remains slightly changed, from ~ 20 ps to ~ 5 ps, in the range of $N_{e-h} = 0.5 - 5 \times 10^{20}$ cm^{-3}. The recombination time of the nanopillars sample decreases approximately two orders of magnitude, from ~ 10 ns to ~ 300 ps, in the range of $N_{e-h} = 1 - 6 \times 10^{20}$ cm^{-3}. A linear fit in logarithmic scale to this data is depicted in the inset by the pink line, indicating $1/\tau_r \propto N_{e-h}^2$. This recombination behaviour is attributed to the Auger decay process, being $1/\tau = \gamma \times N_{e-h}^2$ with γ to be the Auger coefficient. Extraction of the Auger coefficient from the SiNP data shows $\gamma = 2 \times 10^{-31}$ cm^6/s in agreement with the published value of 3.8×10^{-31} cm^6/s [47].

The right panel shows the (fast) thermalisation time, attributed to the electron-phonon interaction time, τ_{e-ph}. The results for the nanopillars and nano-inclusions samples are depicted by the blue and green curves respectively. Due to the high uncertainty in the fitting procedure, it is possible to conclude that both samples show an independent behaviour on N_{e-h} with the typical decay time of a few hundreds of femtoseconds.

Figure 2.23: Decay times for silicon nanopillars (SiNP) and nano-inclusions (SiNI) samples vs *e-h* plasma density. Left panel: *e-h* recombination time (note: semi-logarithmic scale) Inset: linear fit to SiNP recombination decay, logarithmic scale. Right panel: electron-phonon interaction time.

2.5 Conclusions and future work

2.5.1 Silicon nano-inclusions - summary

Summarising the experimental results of time-resolved reflectivity from Si nano-inclusions, the following points could be noticed:
- relatively high value of absolute reflection, $R_0 \equiv R(\tau \ll 0)$; it is $R_0 = 60\%$
- extremely high change of time-resolved reflectivity, $\Delta R(\tau)/R_0$; up to $\Delta R/R_0 = 50\%$

High absolute reflection can be attributed to the constructive interference occurring in the α-Si matrix with an average thickness of 510 nm. The typical value of the absolute reflection from α-Si at $\lambda = 800$ nm is approximately 40%, while we have experimentally found this value to be increased by a factor of 1.5. This observation has been supported by qualitative simulations, see upper panel of Figure 2.19. In the case of strongly excited carriers, the simulation shows dependence of the interference phase (and as a result magnitude of R_0 at $\lambda = 800$ nm) on the excited free carrier concentration, N_{e-h}. The pump induced ΔR change has been attributed to the high magnitude of $\partial R/\partial N_{e-h}$ originated from the beatings of R_0 in the calculated range of $N_{e-h} = 1 \times 10^{19} - 1 \times 10^{21}\ cm^{-3}$ as shown in the upper panel of Figure 2.20(a). However, measurements of $\Delta R/R_0$ carried out in this carrier density range, did not show (quasi) periodic beatings of $\Delta R/R_0$.

Optical reflection and transmission (optical properties) control by variation of the excited free carriers population in conjunction with a strong interference phenomena between multilayered structure, can be adopted in research areas of optical modulation problems.

The relaxation time, being in order of 300 fs, has been attributed to the electron-phonon interactions. This value is in good agreement with other published results for strongly excited crystalline silicon [20, 59]. Due to relatively long excitation pulse duration of 150 fs, the electron-electron interaction (occurring on $30 - 40$ fs scale) was not resolved. Electron-hole recombination time was found to be $\tau_r = 9$ ps, almost two orders of magnitude shorter than diffusion-free result of the nanopillars sample, indicating non-negligible interaction of the excited carriers with the host matrix of amorphous silicon. Within the experimental accuracy, no $\Delta R(t)$ was observed from "pure" amorphous silicon structure.

2.5.2 Silicon nanopillars - summary

Bulk diffusion-free measurements of carriers dynamics are done by means of time-resolved measurements of a confined electron-hole plasma. The electron-hole recombination time of silicon nanopillars is 700 ps, which is more than two orders of magnitude longer than analogous time of crystalline silicon nano-inclusions. While the electron-phonon interaction time (300 fs) remains similar to both nano-structures.

The long recombination process has been attributed to the two physical phenomena: (*i*) strong suppression of the diffusion rate, which could be understood directly from Figure 2.9, Si nanopillars are grown on SiO_2 insulator which prevents electron diffusion from the semiconductor nanopillars, (*ii*) a homogenous excitation of the material in the nanopillars, preventing “quicker” recombination.

The recombination is found to be two-particle Auger process. The Auger constant has been extracted and is in good agreement with the literature value.

Fitting of the data has been done by the two-exponential decay empiric model introduced by Sabbah *et al.* [27], alternatively, a three-levels model of the dynamics is brought. Both models show similar decay time results.

The analysed silicon nano-structure acts as carrier density-tuneable antireflective coating at near infrared spectrum.

2.5.3 Future work

Nano-inclusions

Experimental verification of $\Delta R(\tau)$ dependence on thin film interference might become clearer after measuring samples of various film thickness and excitation at a broader range of wavelengths.

Silicon direct band gaps excitation can be achieved by an optical energies above 3.4 eV and 4.2 eV, providing reach relaxation and recombination dynamics. Application of much shorter than 150 fs, for example, $10 - 30$ femtosecond pulses, can resolve electron-electron interactions being in order of $30 - 40$ fs.

Nanopillars

Variation of nano-pillars density and form-factor can enhance the antireflection quality of the nanopillars layer. Addition proof of a diffusion suppression due to low dimensionality of the structure could be achieved by means of a semiconducting substrate instead of an insulating one.

Comparison of these results to the reflectivity from the actual grown substrate (bulk silicon or SOI substrate) should be essential. The latter one could by achieved directly by means of polishing and SEM feedback.

Technique

Introduction of a lock-in amplifier instead of monitoring of two channels by means of an oscilloscope, should in principle, increase the sensitivity of the signal, according to our estimations it should be well below 0.1%. This allows observation of fast electron dynamics in the fluence range of $F \ll F_m$.

Chapter 3

Time-resolved photoluminescence

3.1 Introduction

3.1.1 Overview

Amorphous silicon nitride thin films have been widely utilised in the semiconductor device industry for a long time [60]. Additional scientific attention this material has received with a development of the nanoscale field in the semiconductor industry for its suitability to be a dielectric host material for silicon nano-particles. An application of silicon nitride SiN_x matrix with embedded nano-crystalline silicon (nc-Si) particles can be found in future generation of optoelectronic devices [61, 62, 63] and in an improvement of the efficiency of solar cells [64, 65, 66, 67]. From a fundamental point of view, an efficient wavelength adjustable photoluminescence (PL) has been observed from SiN_x based thin films [60]-[69]. However, the nature of this PL has rather quite complex explanations based on various models.

The visible PL adjustment is believed to be based on the size of the embedded nc-Si particles, with negligible influence of the SIN_x matrix. For example, quantum confinement of nc-Si grown inside the SiN_x film host has been pointed out as the main PL trigger, but not always being supported by the structural analysis [60, 63, 65, 66]. There are cases when visible PL has been attributed to: defect states [64, 70], surface states at the nc-Si$-$$SiN_x$ interface (particle-matrix interface) [61] and radiative recombination between localised band-tail states [68, 69].

To emphasise the SiN_x based PL complexity, there is an example of sixfold PL spectrum from Si-rich SiN$_x$ film investigated at room temperature by Liu *et al.* [71] depicted in the panel A of Figure 3.1. Authors attribute multiple transitions to silicon dangling bonds and defect states of $N - Si - O$ and Si/SiO_2 interfaces. See energy diagram in the panel B of Figure 3.1.

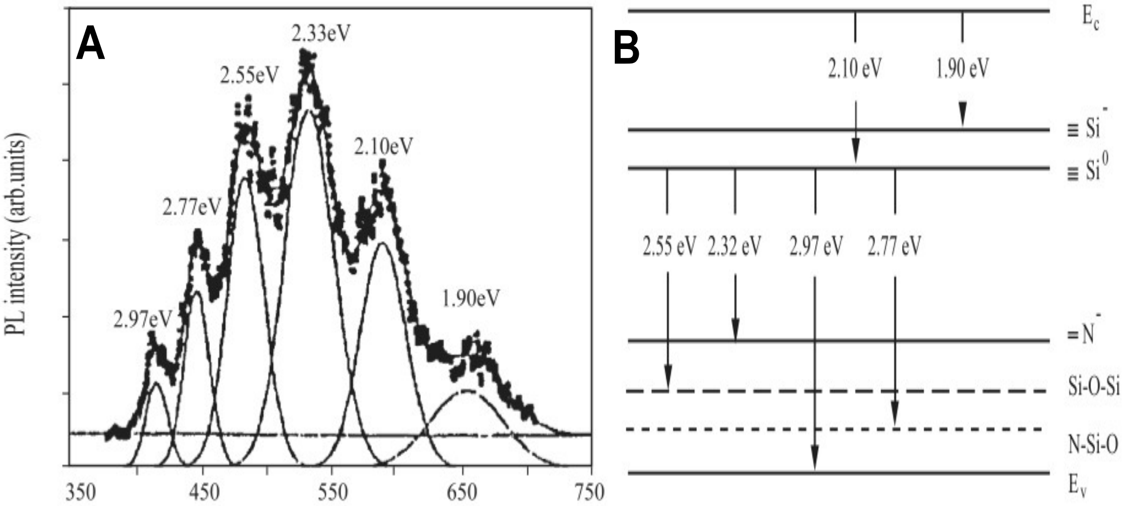

Figure 3.1: Photoluminescence from Si-rich SiN$_x$ films: (A) Sixfold visible photoluminescence peak spectrum, (B) Energy state diagram: multiple transitions correspond to silicon dangling bonds and defect states of $N - Si - O$ and Si/SiO_2 interfaces. Adopted from Liu *et al.* [71].

3.1.1.1 The aim of this work

This work is based on the SiN$_x$ thin film structures grown by plasma enhanced chemical vapour deposition, while no pure nc-Si phase has been observed. The aim of this work is to investigate electron-hole relaxation dynamics of SiN$_x$ by means of time-resolved photoluminescence, TRPL (as a part of collaborative experimental analysis of sub-band gap absorption states of SiN$_x$ thin film, see Appendix A).

3.1.2 Time-resolved photoluminescence

Photoluminescence measurement technique is a commonly known tool for band structure investigation in quantum systems. Ideally, emitted photons would contain information about inter-band and inter-level energy separation. Practically, one should pay attention for level broadening, which is corresponded with finite temperature, imperfections and impurities (in solid state systems).

Time-resolved PL method [45, 46, 47, 48, 49, 50] provides information about carrier

3.1.2.2 Non-exponential photoluminescence decay

Two-level picture of an electron-hole recombination dynamics from a valence to a conduction level ought to be of an exponential behaviour. However, for more complex cases involving sub-band energy levels associated with high percentage of impurities and imperfections in bulk materials or open bonds in amorphous structures, the characteristic decay models are more complex.

Slight deviation from the exponential behaviour can be described by "stretched" exponential decay functions [73, 76]:

$$I(t) \propto (\tau/t)^{1-\beta} exp[-(\tau/t)^{\beta}], \tag{3.1}$$

and respectively

$$I(t) \propto (\beta/\tau)(\tau/t)^{1-\beta} exp[-(\tau/t)^{\beta}], \tag{3.2}$$

where I is the PL intensity, t the time, τ the effective life-time and β is parameter taking values between zero and one. This parameter arises from a generalisation of the exponential function, $exp(-t/\tau)^{\beta}$, which is called *stretched* when $0 < \beta < 1$ (and *compressed* when $\beta > 1$).

Strongly non-exponential PL intensity decay forms can be represented in so called life-time distribution manner, suggested by Tsang and Street [77]. The life-time distribution is given in the following form:

$$G(\tau) \propto I(\frac{\partial lnI}{\partial ln\tau}) \tag{3.3}$$

For example, strongly non-exponential PL decay from various amorphous SiN_x samples investigated by Seol *et al.* [73], is depicted in the panel A of Figure 3.3. The joint lower graph is $\tau * G(\tau)$ vs τ distribution of the above decay. In addition, these authors show a life-time distribution upon a photoemission spectrum as depicted in the panel B. Indicating the longest life-time to be exponentially red-shifted, effective energy decay factor indicated by $\gamma = 316$ meV. This phenomena has been associated with a non-radiative hopping process of the photo-excited carriers within the localised states at the band tails.

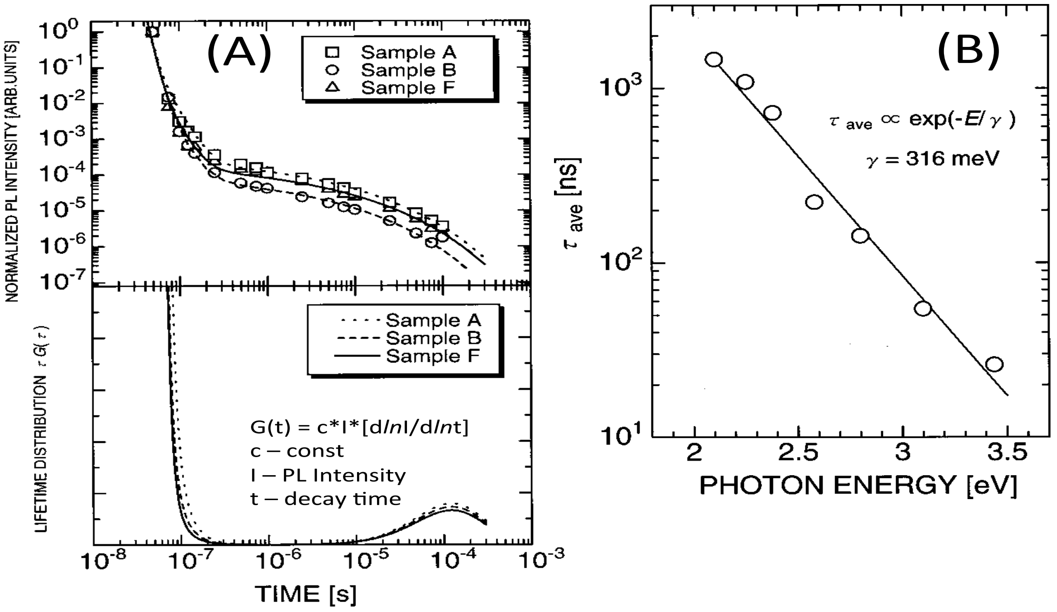

Figure 3.3: Time-resolved photoluminescence of $\alpha - SiN_x$ samples: (A, upper panel) normalised decay intensity, (A, lower panel) lifetime distribution $t * G(t)$ with fast and slow components. (B) Average lifetime distribution summary of the fast, nanosecond, component vs photoluminescence energy, characterised by an effective energy decay factor γ. Adopted from Seol *et al.* [73].

3.2 Technical background

3.2.1 Samples

Samples being used in the TRPL experiment are commercially produced by [78]. The SiN$_x$ thin film layers have been grown by plasma enhanced chemical vapour deposition (PECVD) on a silicon substrate. Summary of the deposition conditions and electronic properties of the thin films is listed in Table 3.1.

Table 3.1: Deposition conditions and resulting properties of the SiN_x films, information provided by [78]. Gas flow rates of silan (SiH_4), ammonia (NH_3) and nitrogen (N_2). Stoichiometric ratio x = N/Si. Photoluminescence peak: central energy (E_{PL}) at FWHM (ΔE_{PL}); normalised signal of the photo-excitations at 532 nm (I_{PL}^{532nm}) and 405 nm (I_{PL}^{405nm}), respectively. Tauc band gap energy (E_T), Urbach tail energy (E_U) and d film thickness.

Sample	SiH_4 $[\frac{cm^3}{min}]$	NH_3 $[\frac{cm^3}{min}]$	N_2 $[\frac{cm^3}{min}]$	N/Si [%]	E_{PL} $[eV]$	ΔE_{PL} $[eV]$	I_{PL}^{532nm} [%]	I_{PL}^{405nm} [%]	E_T $[eV]$	E_U $[meV]$	d $[nm]$
SiN_x231	9	8.5	50	-	1.53	0.44	100	100	2.37	-	210
SiN_x256	6	9	60	-	1.61	0.46	227	500	2.6	214	150
SiN_x274	18	20	181	78	1.49	0.39	923	920	2.35	-	370
SiN_x276	16	20	181	84	1.55	0.53	1563	774	2.32	190	440
$GaAs$	-	-	-	-	1.4	0.03	-	-	-	-	∞

In addition, visible PL data has been available at monochromatic excitation laser energies of 2.33 eV and 3.06 eV leading to PL emission centred around 1.5 eV, see Figure 3.4. Extracted PL peak waist information is indicated in the table as well. Furthermore, PL signal from bulk GaAs has been utilised for calibration reasons and is introduced in the above table and figure by the pink curve.

Cross section images of two samples taken by Scanning Electron Microscope (SEM) at scale bars of 50 nm are shown in Figure 3.5. Note, absence of nc-Si phase is based on X-rays analysis and higher magnification of SEM analysis by the maker.

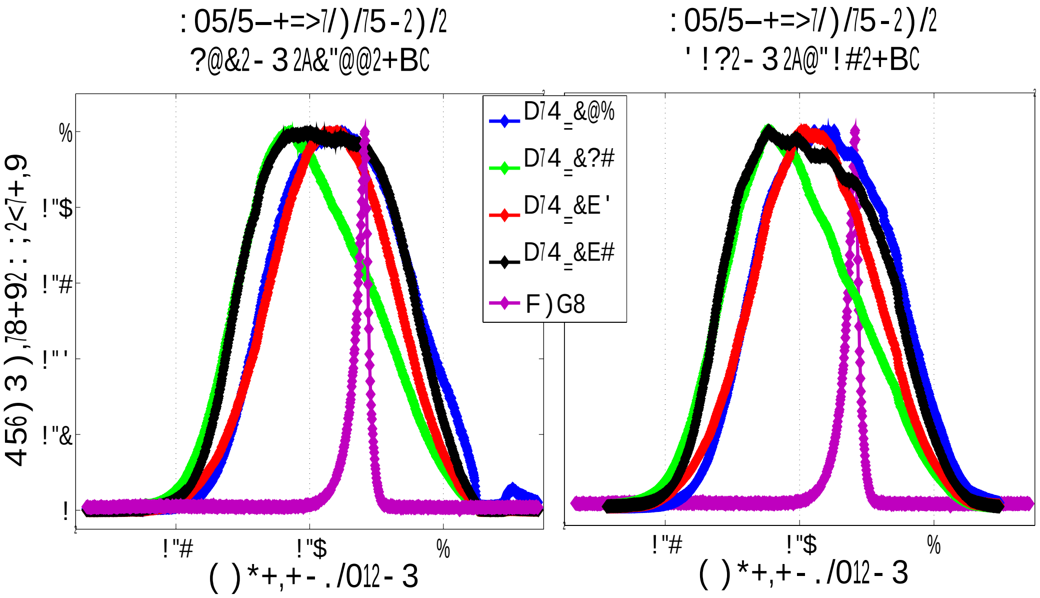

Figure 3.4: Photoluminescence signal from SiN_x samples and GaAs as a reference. Left panel: photo-excitation at 532 nm (2.33 eV) and 10 mW. Right panel: photo-excitation at 405 nm (3.06 eV) and 2 mW, provided by [78].

Figure 3.5: Cross section images of SiN_x274 and SiN_x276 samples taken by scanning electron microscope, scale bars = 50 nm. The thin layer thickness is indicated by a perpendicular line. Provided by [78].

3.2.2 Experimental setup

Pulsed super-continuum laser Fianium SC-450-pp [79], has been utilised as an excitation source. Repetition rate was set to 1 MHz at average pulse duration of 6 ps. The actual pulse duration depends on the selected wavelength. Excitation wavelength band of $450 - 600$ nm, well above the optical band gap see Table 3.1 was selected from the whole spectrum (approximately $450 - 2000$ nm) by a set of extended efficiency optical filters. The samples have been subjected to 4.6 mW focused excitation beam at the angle of incidence equal to 45°, see Figure 3.6. Estimated fluence per pulse in this configuration is in order of 30 μJ/cm^2 for a spot of approximately 100 μm × 100 μm.

For single photon detection, cooled high-speed photo-multiplier tube (PMT) detector has been used. The PMC-100-20 model, designed by Becker&Hickl GmbH [80], has been developed to work at visible and extended infrared spectrum range of $300 - 900$ nm. The PMT sensitivity is adjusted by a high-voltage unit being controlled remotely by a software program. A response time of this devise, within the operating settings, has been 0.5 ns. This time slot is much longer than excitation pulse duration laying in a few picoseconds regime. Therefore, particular uncertainty in the pulse width does not affect the measurement process.

The PMT photo-event counting has been achieved deploying 4 GHz multiple-event time digitiser. The computer-based model P7887, made by Fast ComTec GmbH [81], has a time-bin resolution of 250 ps. This accuracy determines time resolution of the measurement apparatus. Additional apparatus limitation is 0.5 ns dead (triggering) time coming from the PMT sensor and electronics response.

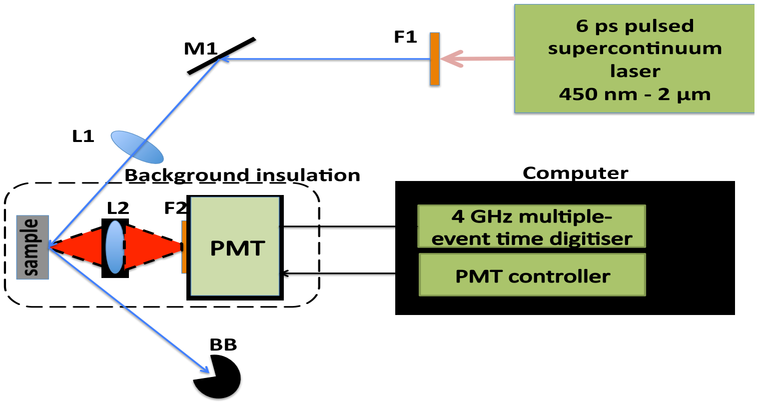

Figure 3.6: Schematic view of the time-resolved photoluminescence experiment. Description: L1-L2 focusing lenses, M1 plane mirror, F1/F2 excitation wavelength pass/stop filters respectively, BB beam block.

3.3 Experimental results

3.3.1 System calibration

In order to start PL measurements with a new system, there was a need of a "sanity check" based on a well-known PL source. To fulfil this task, commercially available Rhodamine 110 chloride ($C_{20}H_{14}N_2O_3HCl$) dye has been chosen. It has been outstanding for high luminescence emission at 520 nm for an excitation at 498 nm in methanol medium [82]. The results of TRPL are shown in Figure 3.7. The blue curve represents the PMT detector response to the excitation pulse. It has almost symmetric (gaussian-like) profile with the FWHM = 0.5 ns. Rhodamine 110 TRPL decay is depicted by the green curve. Decay time at which the signal reduces by 1/e times is approximately 1.5 ns, in partial agreement with published elsewhere [83] value of 4 ns at room temperature, deploying single molecule excitation technique. While the long range decay behaviour (depicted in the inset in the semilogarithmic scale) scales with a decay time of 0.7 ns. This range is not accessible for the single molecule excitation technique due to small event counting numbers (weak statistics).

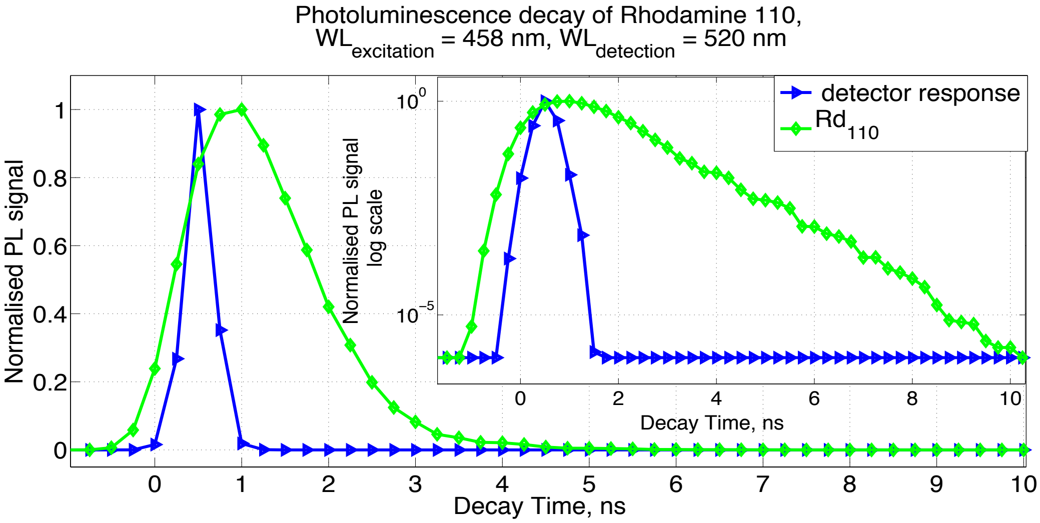

Figure 3.7: Photoluminescence decay of Rhodamin 110 chloride dye, Rd_{110}. Inset: semi logarithmic scale for eye guide.

For a better TRPL guidance, a bulk GaAs sample has been chosen as a semiconductor origin PL source with an emission wavelength similar to silicon nitride optical properties. In analogy with the format presentation of the previous figure, TRPL data for GaAs is depicted in Figure 3.8 by the red curve. The extracted exponential decay time is about 0.5 ns, in

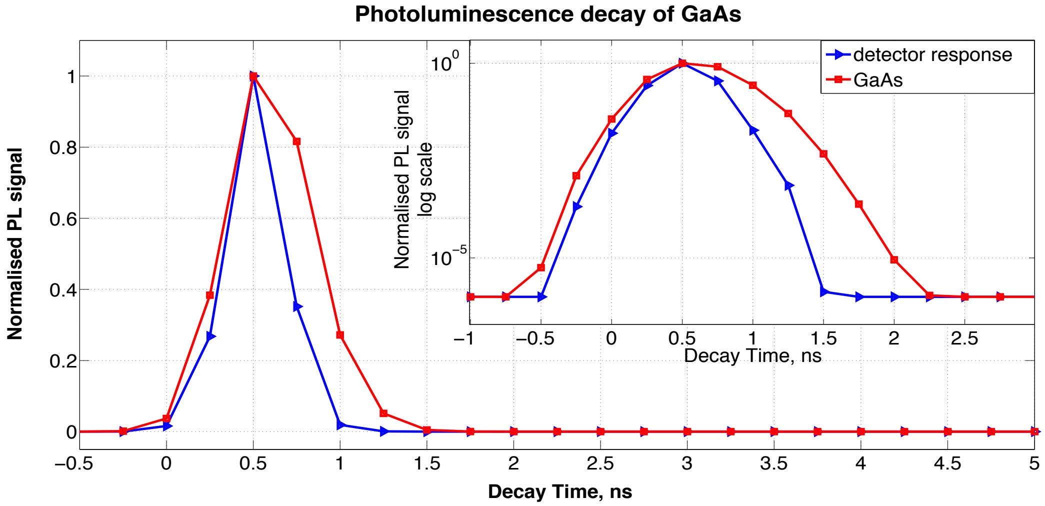

Figure 3.8: Photoluminescence decay of GaAs. Inset: semi logarithmic scale for eye guide.

general agreement with the known [84] values of 1 ns investigated at room temperature for similar to the currently investigated e-h plasma densities range below 10^{17} cm^{-3}.

3.3.2 Silicon Nitride results

Demonstrated in Figure 3.9 are normalised to unity TRPL results for all four SiN$_x$ and GaAs samples taken at similar conditions. The detector response curve is depicted for eye guidance as well. All samples have been subjected to the highest available fluence of 30 μJ/cm^2. Yield rate of the integrated PL is given in kilo counts per second (Kc/s) at particular photo-amplification voltage. For SiN$_x$ 231, 256, 274 and 276 the yield rates are: 50 Kc/s, 5 Kc/s, 250 Kc/s and 260 Kc/s respectively; the highest detected yield rate is 300 Kc/s for GaAs sample. The maximum PL amplitude decrease by 1/e occurs during 0.6 ns in all four samples. It is noticeable, that a decay form of SiN$_x$ 274 and 276 samples has a second peak (shoulder) approximately 3 ns after the excitation.

The long range decay times, τ, have been extracted fitting exponential decay, as can be seen in Figure 3.10. For eye guidance, the exponential decay of 1 ns is depicted by the dashed line as well as the results of Rhodamine dye and the detector response. The extracted decay times are as follows: SiN$_x$231 $\tau = 0.24$ ns, SiN$_x$256 $\tau = 0.29$ ns, SiN$_x$274 $\tau_1 = 0.28$ ns for the main peak and $\tau_2 = 0.32$ ns for the secondary peak, SiN$_x$276 $\tau_1 = 0.26$ ns for the main peak and $\tau_2 = 0.30$ ns for the secondary peak, GaAs sample decay time is $\tau = 0.1$ ns.

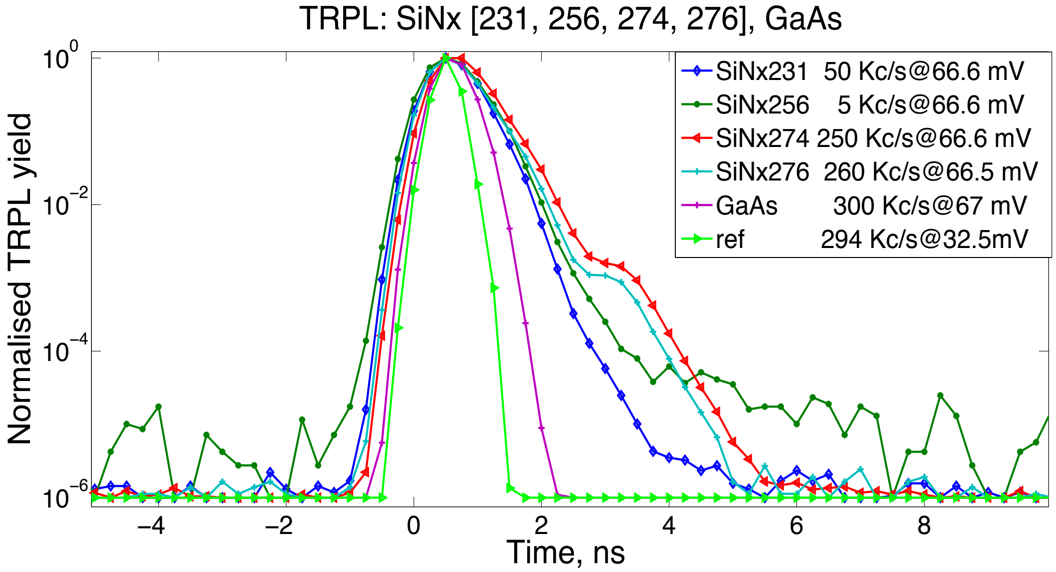

Figure 3.9: Time-resolved photoluminescence decay of SiN_x231, SiN_x256, SiN_x274, SiN_x276 and GaAs. Yield rate (kilo counts per second) is provided alongside the photo-amplification voltage (mV). Detector's response to the excitation is depicted by the "ref" curve.

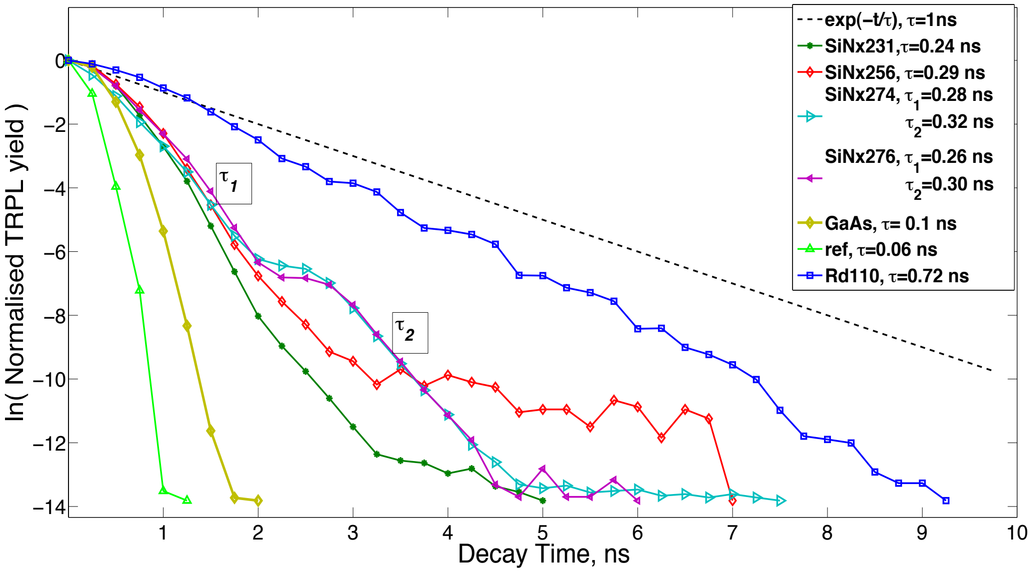

Figure 3.10: Exponential decay time constants extraction from time-resolved photoluminescence data.

3.3.2.1 Secondary decay peak

There is a need to make sure that an origin of the secondary TRPL decay peaks, coming from SiN$_x$274 and 276 samples, is not artificial but represents a certain physical process. Being unable to significantly vary the excitation intensity (as well as the temperature regime) in order to increase the PL rate, there was an option to change gradually a sensitivity level of the detector. Namely, sensitivity level of a PMT detector is being controlled directly by the applied high-voltage potential to dynodes, providing signal amplification.

Results for TRPL versus variable sensitivity are presented in Figures 3.11 and 3.12 for samples SiN$_x$274 and 276 respectively. It is clearly seen that magnitude of the secondary peaks scales well with the sensitivity and counting PL rate. An issue with the single counting devises is that at certain high level of events the counting becomes no more "single" and avalanche effects can affect measurements. To check this condition, similar sensitivity level variable measurement has been done on the GaAs sample. This sample provides generally higher PL rate than all SiN$_x$ samples. The results of this trace are depicted in Figure 3.13 showing no evidence of an artificial effect. Bearing this in mind, it is likely to conclude that secondary peaks can be detected only at the high sensitivity level, while they describe a natural process rather than an artificial one.

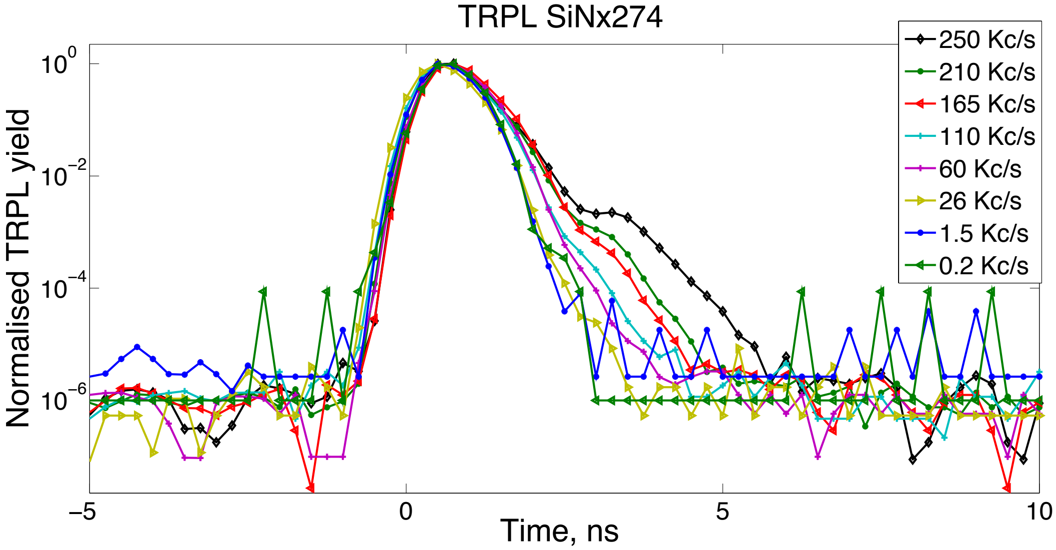

Figure 3.11: Time-resolved photoluminescence decay of SiN$_x$274 at various signal amplification settings.

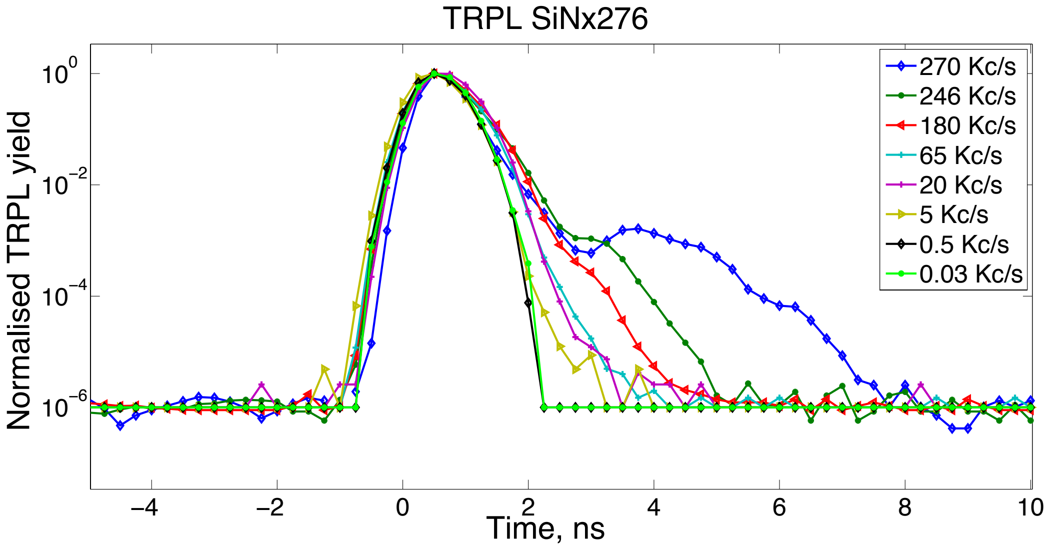

Figure 3.12: Time-resolved photoluminescence decay of SiN$_x$276 at various signal amplification settings.

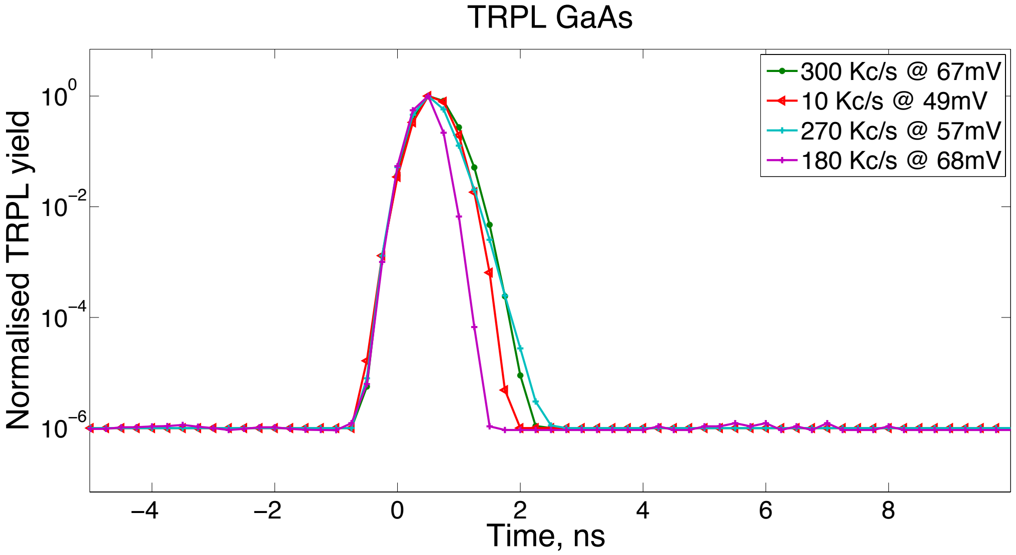

Figure 3.13: Time-resolved photoluminescence decay of GaAs at various signal amplification settings. No artificial behaviour for $t > 3$ ns up to the highest photo-amplification regime (68 mV).

3.4 Analysis and discussion

3.4.1 Radiative recombination

Observed radiative recombinations occur within $1.4 - 1.8$ eV energy range while the band gap energies of all SiN$_x$ samples are above 2.3 eV. The PL results show electron-hole recombination taking place at the subband gap states originated by various impurities of the amorphous silicon-nitride structures. Above band gap excited carriers thermalise toward subband gap sates and recombine, in majority, within typical time of 0.6 ns. The PL decay was fitted with exponential decay times of $0.24 - 0.32$ ns. The PL decay was experimentally observed during $5 - 7$ ns decreasing almost 6 orders of magnitude.

3.4.2 Secondary radiative decay process

We would like to focus on the secondary TRPL peak phenomena of SiN$_x$274 and 276 samples. The extracted decay times are shorter by one order of magnitude than the time at which the secondary decay begins (at $T_d \approx 3$ ns). Although the contribution of the secondary peak to relative yield is about 1% it is well observed due to its "delayed" (PL followed) electron-holes recombination. This dynamics can not be described by just two levels model (valence and conduction bands) and requires more complex solution. It was technically impossible to produce energy-resolved TRPL measurements in order to achieve more clear energy levels diagram. However, we would like to describe the secondary PL decay nature assuming the following scenario based on "long charging - quick discharging" model depicted schematically in Figure 3.14. While the main excitation and recombination processes occur between Ground (valence) and Upper (conduction) bands characterised by a decay time T_1. A small fraction of the e-h pairs being localised (with effective accumulation time T_2) on the Intermediate level. Furthermore, this localisation takes place during relatively long time T_d followed, after $t > T_d$, by a relatively fast recombination, characterised by a decay time T_3. Numerical factors P_1 and P_2 describe the probability to recombine to the ground band or to be localised on the intermediate level respectively. A recombination process from the intermediate level is allowed by a step-function time-dependent probability $P_3(t)$, with a step time T_d. The rate equations of this model are given by the following differential set:

$$\frac{dN_U(t)}{dt} = -\frac{P_1 N_U(t)}{T_1} - \frac{P_2 N_U(t)}{T_2} + F(t), \tag{3.4}$$

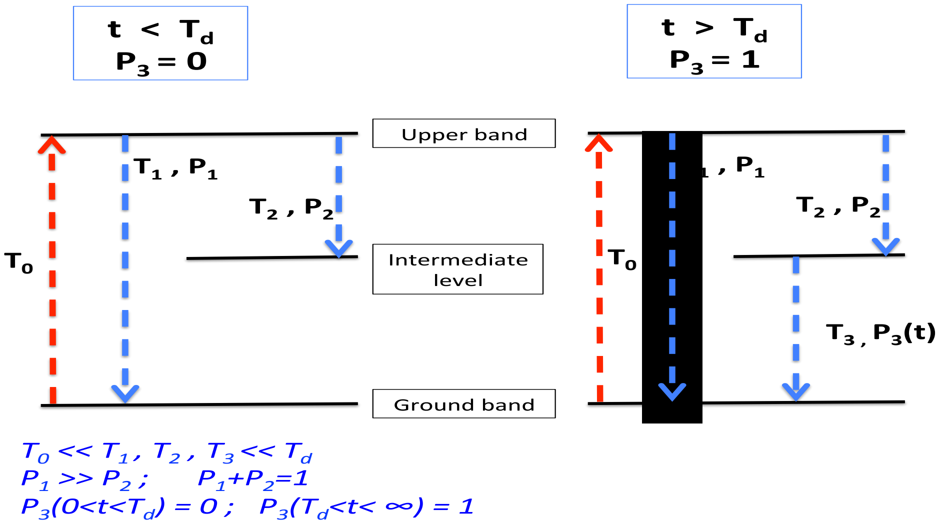

Figure 3.14: Double TRPL described by "long charging - quick discharging" model.

$$\frac{dN_M(t)}{dt} = \frac{P_2 N_U(t)}{T_2} - \frac{P_3(t) N_M(t)}{T_3}, \tag{3.5}$$

$$\frac{dH_G(t)}{dt} = -\frac{P_1 N_U(t)}{T_1} - \frac{P_3(t) N_M(t)}{T_3} + F(t), \tag{3.6}$$

where N_U and N_M denote excited electrons on the upper and intermediate levels respectively, while H_G is a number of holes; initial population F is created by an excitation pulse. The following relations and initial conditions must be fulfilled:

$$\begin{aligned} N_M(t) + N_U(t) + H_G(t) = 0, \\ H_G(t=0) = N_M(t=0) = N_U(t=0) = 0, \\ P_1 + P_2 = 1, \\ P_3(t < T_d) = 0 \quad \& \quad P_3(t > T_d) = 1. \end{aligned} \tag{3.7}$$

Shown in Figure 3.15 is temporal evolution of the main parameters in this model. Described in the panel A is an excitation FWHM = 6 ps pulse occurring at t = 10 ps. Panel B: probability of recombination ("discharging") from the intermediate level. Panel C: population of the upper level. Panel D: population of the intermediate level. Panel E: holes population on the ground level, decreases with the taking place recombination process. Panel F: an error in the fulfilment of the first condition of the Eq.3.7 (total charge is zero in the system).

Fitting of the $H_G(t)$ term to the experimental results is presented in Figure 3.16. While Table 3.2 brings a summary of the decay constants extracted via exponential decay and

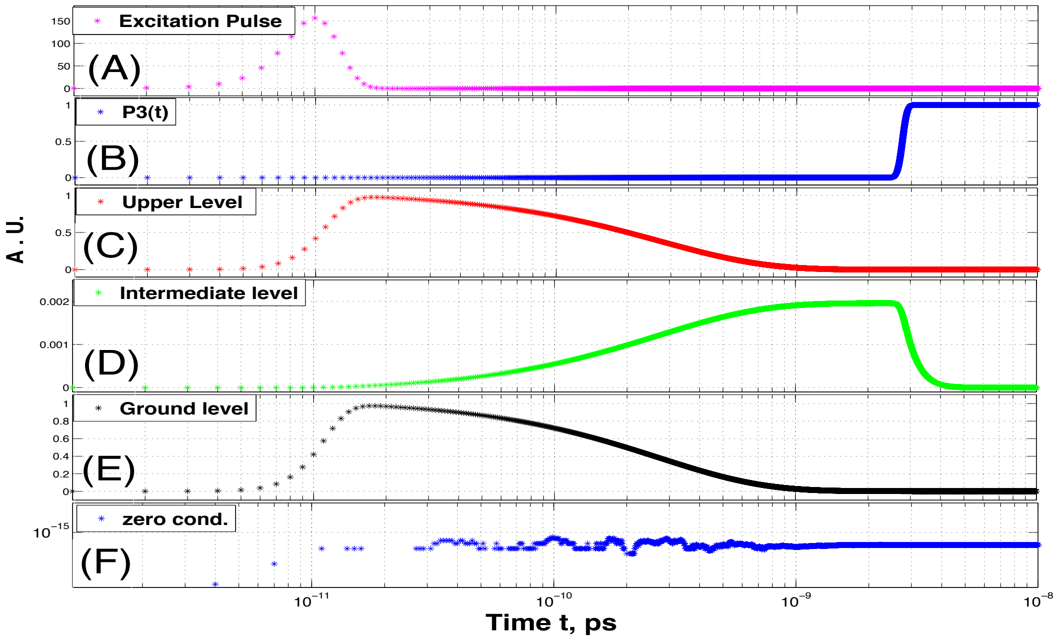

Figure 3.15: Temporal dynamics of the "long charging - quick discharging" model. (A) An excitation pulse (FWHM = 6 ps) occurring at $t = 10$ ps. (B) Probability of recombination ("discharging") from the intermediate level. Transition time from 0 to 1, T_{P3} is shown in Table 3.2 (C) population of the upper level. (D) population of the intermediate level. (E) holes population on the ground level. (F) Total charge error (fulfilment of the first condition of the Eq.3.7).

parameters characterising the presented model. The decay constants T_1 and T_3 show good agreement between both methods.

There are a few main independent processes [76] affecting e-h recombination mechanisms: thermalisation, Coulomb interaction and distribution of localised states. The intermediate level can be associated with a sub-band gap level caused by open/broken bonds in amorphous structures, for example, such as α-Si [85], SiN$_x$ [68, 69, 76, 86], SiO$_x$N$_y$ [76] and SiC$_x$ [74, 75]. These sub-band gap states are called tail-states described by the Urbach tail energy [87]. While largest amount of the excited carriers are forced [88] to recombine locally, some of them can thermalise towards a relatively small number of the lowest sub-band deep energetic sates during relatively long life-time and then recombine via radiative transition, described by the radiative tunnelling model [74, 73, 90, 91].

Thus within this assumption, experimentally observed time T_d is a thermalisation time, while both T_1 and T_3 represent radiative recombination timescale from across the full and reduced band gap respectively.

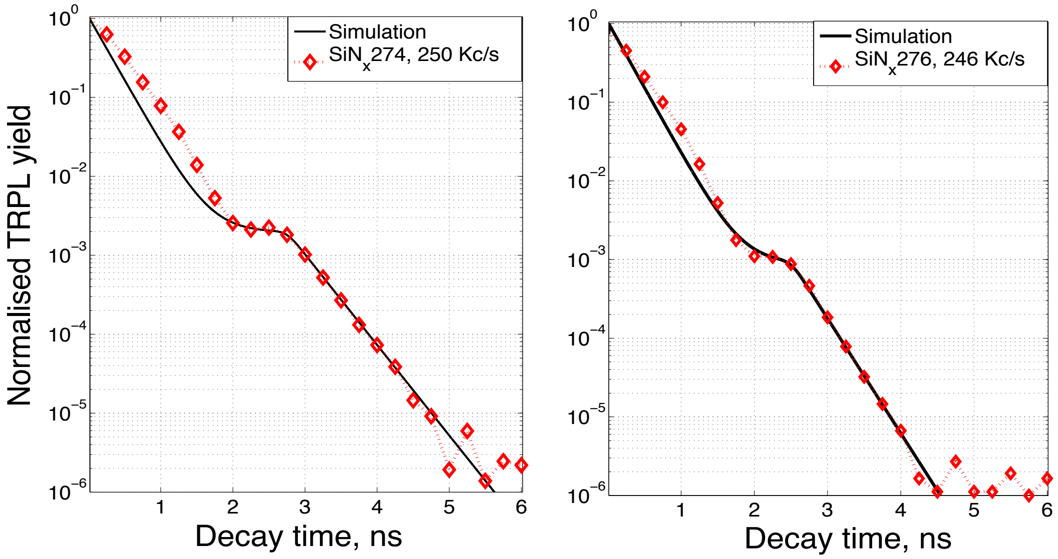

Figure 3.16: Fitting of the "long charging - quick discharging" model to the experimental data. Left panel: SiN$_x$274. Right panel SiN$_x$276.

Table 3.2: Exponential decay times and simulation model parameters summary for SiN$_x$ 274 and 276 samples. T_1 main decay time, T_2 e-h accumulation effective time for the secondary peak, T_3 secondary peak decay time, T_d actual time for e-h accumulation at the intermediate level, T_{P3} transition time from $P_3(t) = 0$ to $P_3(t) = 1$, P_1 probability to recombine directly from the upper band, P_2 probability to be localised at the intermediate level.

Samples/ parameters	T_1 [ps]	T_2 [ps]	T_3 [ps]	T_d [ns]	T_{P3} [ps]	P_1	P_2
SiN_x274 exp. decay	280	-	320	-	-	-	-
SiN_x274 sim. model	270	400	380	2.75	235	0.9971	0.0029
SiN_x276 exp. decay	260	-	300	-	-	-	-
SiN_x276 sim. model	260	350	300	2.5	235	0.9988	0.0012

3.4.3 Decay times comparison

Investigated PL signal was observed at 1.5 eV while an excitation energy band was $2-3$ eV. Both fitting methods, the exponential decay and double radiative model (relevant for samples SiN$_x$274, 276), provide us with sub-nanosecond decay timescale at room temperature.

Group of Deshpande *et al.* [70] reported three characteristic exponential time constants of SiN$_x$ films PL decay: 0.8, 3.5, and 14.0 ns. An excitation energy was 2.3 eV and room temperature conditions. The authors conclude that relative contribution to the decay from the shorter time constants increased with increasing nitrogen content in the structure.

Published, by Seol *et al.* [73, 76] see Figure 3.3, SiN$_x$ films PL decay times results have been shown the fastest decay component to be of nanosecond order (1.4 ns), while the slowest process occurs on millisecond timescale. The authors utilised 5 eV excitation energy for energy selected TRPL investigation. According to this research, fastest PL component corresponds with 3.5 eV and slowest one being exponentially redshifted towards 1.5 eV. These results had been obtained at 20 K slowing down thermalisation processes and increasing decay timescale [89]. In addition, the fitting procedure based on the "stretched exponential decay" defined by Eq. 3.1 with $\beta = 0.4$, making the "stretched decay constant" effectively longer than one defined by the exponential decay.

These make our fast decay results to be in good agreement with the discussed above.

3.5 Conclusions

Time-resolved visible and near infrared photoluminescence measurements have been done on silicon nitride thin films samples. This structure has shown strong PL intensity making its usage as a matrix material for silicon nano-particles not the ideal host. These observations are in agreement with recently published work of Kistner *et al.* [88].

The photoluminescence life-time has been found on a sub-nanosecond timescale for all investigated SiN$_x$ thin films in good agreement with previously published results. Some structures have shown a secondary decay peak approximately 3 ns after the excitation took place. The secondary decay peak has been attributed to the deep sub-band tail states originated by the open bonds of the amorphous structure and leading to the long radiative transition.

Chapter 4

Surface plasmon assisted oxygen dissociation

4.1 Motivation

During recent years a new surface analysing tool, called photo-emission electron microscope (PEEM) [92], has been developing. For example, it can be used for an investigation of a spatial near field distribution [4] or to be adopted into a design of an attosecond nanoplasmonic-field microscope [5]. The technical drawback of this tool is a long-term drift of a sample position with respect to the PEEM detector, making nanometer scale measurements particularly challenging. Furthermore, current financial costs of such system are hardly accessible, preventing this system to be wildly used.

Presented work is an initial step to a potentially alternative apparatus for an investigation of surface interactions on a nanometer-scale. An imaging method of photoemission detection benefits from static design avoiding mechanical issues addressed in the PEEM deployment [4]. The idea is based on an adaptation of the well-established Velocity Mapping Imaging technique [93] to the needs of surface plasmonics, allowing a mapping of the local field distribution down to nanometer-scale objects. The success of the imaging would be based on the strong enough local electric fields, being enhanced by surface plasmon resonances. The key for the electric fields mapping is a presence of external electrically neutral molecules of gas. If the molecules can be ionised by the surface (strong enough) fields they will carry momentum proportional to the product of the action time and the initial surface field distribution. Thus by projecting ions of an external gas in the momentum and spatial coordinates and providing arriving time from the time-of-flight technique (ToF) it may allow to map spatial and field distribution down to the scale of nano-particle objects.

4.1.1 The aim of this work

The aim of this work is to show an experimental evidence of molecular dissociation of oxygen by means of surface plasmon fields only: "Surface Plasmon energy" $+ O_2 \longrightarrow O^+ + O^-$. Experimental work is based on molecular dynamics imaging and energy spectrometry techniques in a high vacuum.

4.2 Theoretical background

Generally speaking, this work is dedicated to find experimental conditions for successful *creation* of charged *particles* by means of strong electromagnetic field of *surface plasmon resonance* with an attempt to adopt this phenomena for electric field distribution microscopy on a nanometer scale. By meaning "particles" one can imagine anything from as light weight as Hydrogen atom to heavy fullerenes of C_{70}. Meaning *creation* should be attributed with ionisation or dissociation (if applicable) process of initially neutral externally injected *particles.* As far as a dissociation process requires molecules build of at least a couple of atoms it is not applicable to molecules consisting of a single atom only (for example, Hydrogen). And lastly by *surface plasmon resonance* should be regarded surface plasmon polaritons (running on metallic "infinite" surfaces) as well as localised surface plasmons (taking place at sharp surface roughness and nanoscale metallic particles).

This work is focused on dissociation of Oxygen molecules by surface plasmon resonance created by photo-excitation of a gold periodic grating with an asymmetric pattern.

An exposure of gold grating to relatively strong laser light causes an unavoidable electron photo-emission, in addition, being enhanced by surface plasmon field. This phenomena will be investigated for possible influence on the oxygen dissociation process.

4.2.1 Basic principles of surface plasmonics

Surface plasmon resonance is a coherent excitation of electrons occurring on the boundary between metal and dielectric surfaces. In this case, *metal* - means a medium with a negative real part of dielectric function, while *dielectric* - is a medium characterised by a positive real part of dielectric function. Surface plasmon resonance can be excited by an externally injected electron beam or a light beam [94]. Light-assisted surface plasmon resonance is often called Surface Plasmon Polariton. Although this work is based on optical excitations only, for simplicity reasons, this phenomenon will be addressed by the name Surface Plasmon (SP) only.

4.2.1.1 Resonance conditions

Let us regard a metal-dielectric boundary, as shown in Figure 4.1. Surface charge displacement due to an external excitation originates an electromagnetic field passing from one medium to another. This field has to obey a momentum conservation and conserve its energy, as defined by Eq's. 4.1 and 4.2 respectively. Each equation set describes the above conditions in the metallic, m and dielectric, d mediums alongside the charge displacement in parallel, x, and orthogonal, z, directions. This problem remains two-dimensional if there is no charge perturbation in the third y direction.

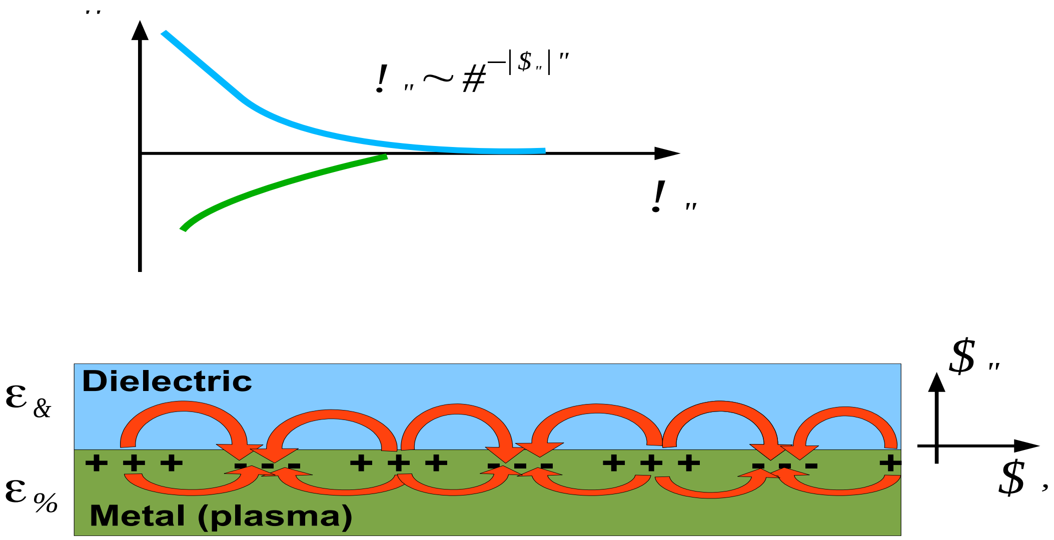

Figure 4.1: Schematic diagram of surface plasmon existing on the plain between metal and dielectric mediums. Strength of resulting perpendicular to the surface electric filed decays exponentially: in metal on the scale of penetration depth, in dielectric medium on the scale of excitation wavelength. Adopted from [95].

$$\begin{aligned} k_d^x &= k_m^x \\ k_d^z/\epsilon_d &= k_m^z/\epsilon_m(\lambda) \end{aligned} \tag{4.1}$$

$$\begin{aligned} (k_d^x)^2 + (k_d^z)^2 &= \epsilon_d * (\omega/c)^2 \\ (k_m^x)^2 + (k_m^z)^2 &= \epsilon_m(\lambda) * (\omega/c)^2 \end{aligned} \tag{4.2}$$

A solution of the above set of equations in the parallel to the surfaces, x direction is

$$k_x = \frac{\omega}{c}\sqrt{\frac{\epsilon_m(\lambda) * \epsilon_d}{\epsilon_m(\lambda) + \epsilon_d}} \tag{4.3}$$

here ω denotes an excitation frequency, ϵ_d is a dielectric constant of the dielectric medium while metallic medium can be described by an excitation wavelength, λ dependent complex dielectric function:

$$\epsilon_m(\lambda) = \epsilon_m^{'}(\lambda) + i\epsilon_m^{''}(\lambda) \tag{4.4}$$

Metal dielectric functions of gold and silver [96] are depicted in panel A of Figure 4.2 by the blue and red curves respectively. Adopting this data for glass Au and glass Ag interfaces ($\epsilon_{glass} = 1.5$), surface plasmon dispersion curves are plotted in panel B. The black line shows light in the vacuum, while the red and blue curves describe the Ag and Au dispersion behaviour respectively.

Figure 4.2: A) Dielectric function of Au and Ag, data is taken from [96]. B) According to Eqs. 4.3 surface plasmon dispersion for metal-glass interfaces of Au and Ag. Light in the vacuum ($c * k$) line is depicted for eye guidance.

4.2.1.2 Excitation of the surface plasmon resonance

Regarding SP phenomena in the k-space, it is all about matching a k-vector of the hosting metal, k_p with an excitation k_{exc}. In the small, but non-zero, k range the k-vector of a light in the vacuum does not match the k-vector of SP in the commonly used metals. For example, the SP dispersion curve of Au is depicted in panel C of Figure 4.3 (as well as in Figure 4.2). Light in the vacuum, which is depicted by the black line, has the linear slope equal to c, while the SP dispersion curve for Au is depicted by the dotted blue curve. The mismatching of k_p and k_{exc} vectors can be solved out by two principal methods.

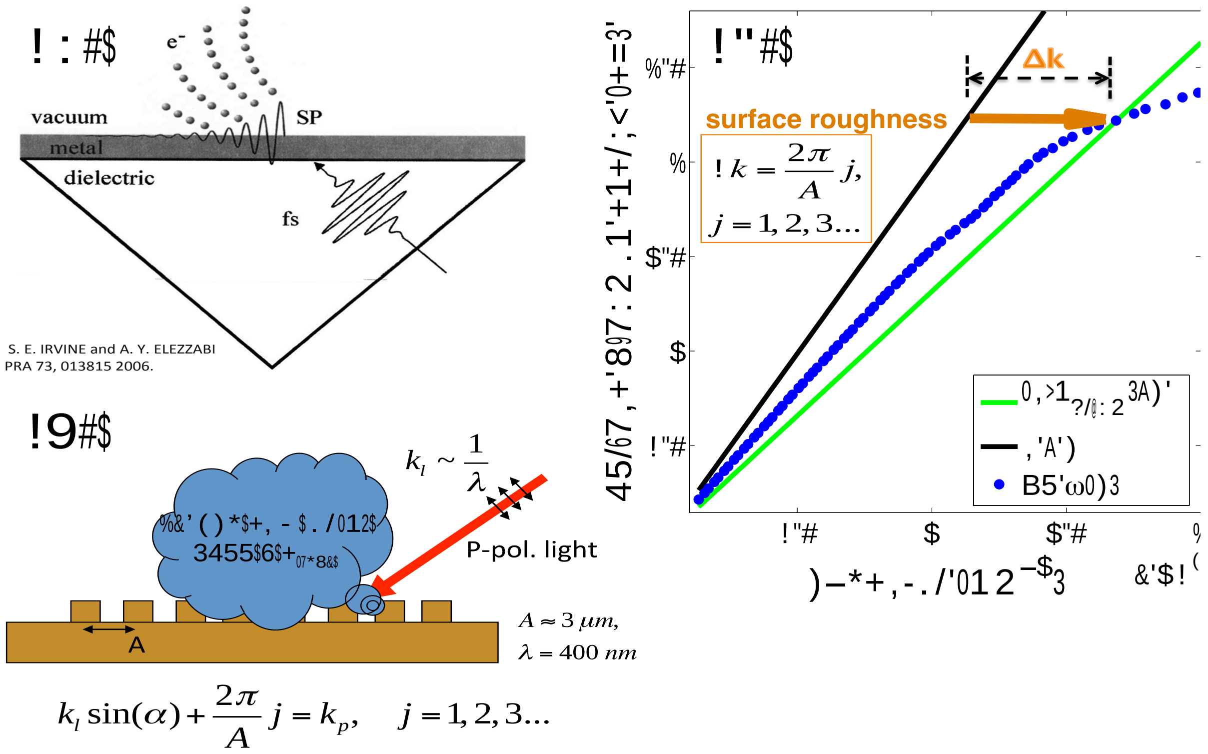

S. E. IRVINE and A. Y. ELEZZABI PRA 73, 013815 2006.

Figure 4.3: Surface plasmon excitation methods and dispersion diagram. Panel A: excitation of a surface plasmon resonance by virtue of a glass prism, Irvine *et al.* [97]. Panel B: excitation of a surface plasmon on a gold grating. Panel C: Energy vs k-vector diagram for Au thin film and k-vector matching conditions: green line corresponds to the glass prism method, arrow corresponds to the surface roughness momentum of the periodic grating, black line denotes light in the vacuum. Au data is taken from [96], see Figure 4.2 for more details.

The first method [98] is based on the slowing down the light in the vacuum, introducing a dielectric medium (characterised by a refractive index n) with an effective light velocity $c/n < c$, leading to matching the SP slope with the metal dispersion curve. The convenient way to excite SP in this way is to use a glass prism. Light is passing through the dielectric glass (with dielectric constant greater than a dielectric constant of the external medium, usually air or water) and creates the SP propagating in the film [95], see Figure 4.3 (A).

The second method is based on a gaining of an additional momentum, which is a mismatching the difference $k_p - k_{exc}$ [99]. This additional k-vector can come from a periodic surface roughness of the metal. An ideal "roughness" is a grating with a known periodicity parameter, A, providing additional k-vector $k_{grating} = \frac{2\pi}{A}j$, while j being an integer. An excitation k-vector is defined as a projection of the inverse laser wavelength, $1/\lambda$ on the grating surface, $k_{exc} = 1/\lambda * \sin(\alpha)$ and α being an incidence angle. This method is sketched basically in the panel B of Figure 4.3.

4.2.1.3 Ponderomotive potential

This work is based on an ultrashort pulsed SP excitation. The z-component of SP has an evanescent field. For example, works of Irvine *et al.* [97], and Wynne *et al.* [100], have been dedicated to SP enhanced electron emission from Au thin film. In their studies, femtosecond laser pulses are directed through a prism and impinge on a metallic film. This optical pulse is coupled to SP oscillations at the metal vacuum interface, resulting in an enhanced electric field that decays exponentially into the vacuum. Electrons, ejected via multi-photon absorption, are emitted at the same location as the SP wave and are accelerated via the evanescent field, see panel A of Figure 4.3.

Complete derivation of the oscillating electromagnetic field away from the surface is brought elsewhere, [101] here only the basic principals will be shown. Let us suppose a magnitude of the electro-magnetic field due to SP to be E_{SP}, thus the evanescent oscillating field in the z direction is $E(z,t) = E_{SP}\cos(\omega_0 t)e^{-z/\lambda}$. The Lorentz force on the emitted electrons is $F(z,t) = eE(z,t)$. This equation can be written in the differential form with respect to z direction: $\ddot{z} = eE_{SP}/m_e \cos(\omega_0 t)e^{-z/\lambda}$. For photo-excitations by a femtosecond laser the fast oscillation period is 2.7 fs leading to a very small z displacement [100]. This allows a separation of the electrons coordinate into slow and fast changing in time parts [102]: $z(t) = z_s(t) + z_f(t)$ respectively, requiring $z_f \ll z_s$ and $\ddot{z}_s \ll \ddot{z}_f$. Using first order Taylor expansion at z_s we obtain $\ddot{z} = \ddot{z}_s + \ddot{z}_f = eE_{SP}/m_e cos(\omega_0 t)(e^{-z_s/\lambda} + z_f \partial(e^{-z_s/\lambda})/\partial z)$. Initially, using the approximations above this equation can be reduced to $\ddot{z}_f = eE_{SP}/m_e \cos(\omega_0 t)e^{-z_s/\lambda}$ and solved for $z_f = -eE_{SP}/(m_e\omega_0^2)\cos(\omega_0 t)e^{-z_s/\lambda}$. Putting this solution back, we can solve initial expansion for z_s only, obtaining $\ddot{z}_s = -e^2E_{PS}^2/(m_e\omega_0^2)\cos^2(\omega_0 t)e^{-z_s/\lambda}\partial(e^{-z_s/\lambda})/\partial z$. Averaging over oscillation period $\omega_0 t$, $\ddot{z}_s = -e^2E_{PS}^2/(2m_e\omega_0^2)e^{-z_s/\lambda}\partial(e^{-z_s/\lambda})/\partial z$. Looking for a potential, U generally defined as $m_e\ddot{z} = -\partial U/\partial z$ and assuming $z(t) \approx z_s(t)$ the ponderomotive potential, U_{pond} takes form:

$$U_{pond} = \frac{e^2 E_{SP}^2}{4 m_e \omega_0^2} e^{-2z/\lambda}. \tag{4.5}$$

Note: an effect of additional electrons acceleration due to "positive oscillation phase" (half a cycle of fast evanescent oscillation acting outwards from a surface) is addressed by these authors [103], however this phenomena lays out of the scope of this work.

4.2.1.4 Ponderomotive shift

An energy shift in the emitted electrons spectra corresponded to the life time of the accelerating electric field on the surfaces is called Ponderomotive shift [104]. Theoretically, this shift is proportional to the time that a carrier is spending in the presence of the field and limited to the maximum value of the Ponderomotive potential, see Eq. 4.5. Additional phase sensitive effects can affect this limit during half a cycle, causing an energy broadening [103]. A SP field lifetime is strongly correlated with the excitation laser pulse duration, and being exponentially decreased by relaxation dynamics, such as plasmon-phonon interaction taking place on a hundred femtosecond timescale [105, 106].

Figure 4.4: Ponderomotive shift in the photoelectron yield from Au due to longer pulse duration at fixed laser intensity, 3.2×10^9 W/cm^2: (a) 60 fs, (b) 190 fs, (c) 400 fs and (d) 800 fs. From Kupersztych *et al.* [104].

The following authors [104] presented experimental work about ultrafast photoemission from gold grating, showing controlled ponderomotive shift by excitation pulse duration, see Figure 4.4. Deploying pulses of 60 fs, 190 fs, 400 fs and 800 fs an energy shift has been achieved approximately by 1.5 eV, 16 eV, 18 eV and 25 eV respectively, assuming a four-photon process and initial free electron energy of 1.1 eV (4 photons of 1.55 eV minus Au work function of 5.1 eV).

4.2.2 Photoemission from gold

4.2.2.1 Time-resolved photoemission

Lifetime measurement of surface plasmon excited on gold grating has been done by Kupersztych *et al.* [104]. Authors deployed autocorrelation measurements of photoemission by ToF method. Sample grating was subjected to a couple of collimated equal intensity delayed in time pulses. Angle of incidence $\alpha = 65^o$ was matched with SP resonance. The results are shown in Figure 4.5 for pulse durations of 60 fs and 400 fs. Central peak is a results of temporal and spatial overlap of two excitation pulses at non-linear absorption regime. Theoretically, an increase in the photo-electron yield scales with the power of multi-photon process, NL. Namely, for gold (work function 5.1 eV) irradiated by a couple of 800 nm (1.55 eV) laser pulses $NL = 4$ and the ratio between sum of two temporally overlapped and well temporally separated pulses (with intensity I_1 and I_2 for each beam) is $(I_1 + I_2)^4/(I_1^4 + I_2^4)$. In the case when beam intensities are equal $I_1 = I_2$ this ratio obtains a maximum value of 8, as can be seen in the background to peak contrast ratio for both pulse durations. In general, this contrast ratio, CR can be written in the following form:

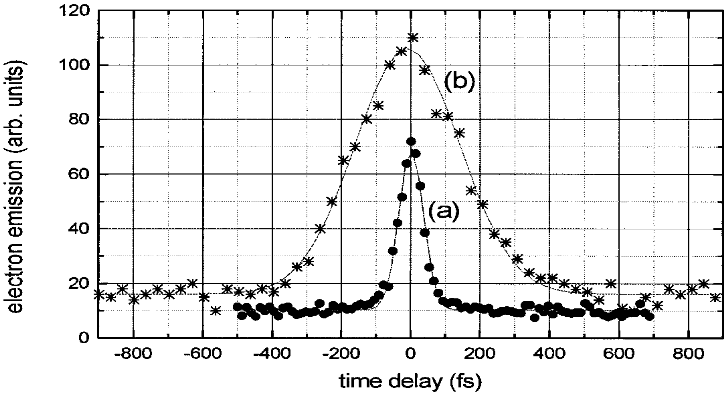

Figure 4.5: Measurement of plasmon lifetime by autocorrelation technique: two collimated equal intensity 800 nm (1.55 eV) laser pulses hits Au grating surface at $\alpha = 65^o$. Electron signal emitted in the presence of a surface plasmon resonance, as a function of relative delay between pulses for two pulse durations: 60 fs (a); 400 fs (b). From Kupersztych *et al.* [104].

$$CR = (I_1 + I_2)^{NL}/(I_1^{NL} + I_2^{NL}) \tag{4.6}$$

4.2.2.2 Nonlinear photoemission

The following authors Elezabbi and Irvine [107] have shown nonlinear photoemission from Au and Ag films at presence of SP resonance. Work functions of Ag and Au are 4.26 eV and 5.1 eV respectively, thus photo-excitation by 800 nm (1.55 eV) femtosecond pulses results multi-photon emission of order $NL = 3$ for Ag and $NL = 4$ for Au. Experimental results, see Figure 4.6, show agreement with multi-photon emission at relatively low intensity range below 5 GW/cm^2. Above this intensity, NL index drops to $NL = 1.26$ for Au and $NL = 1.47$ for Ag films. The authors suggest tunnelling ionisation mechanism [108] to be responsible for photoemission at strong fields. This mechanism is SP independent, as being shown by Toth *et al.* [109] during SP-free Au photoemission experiment.

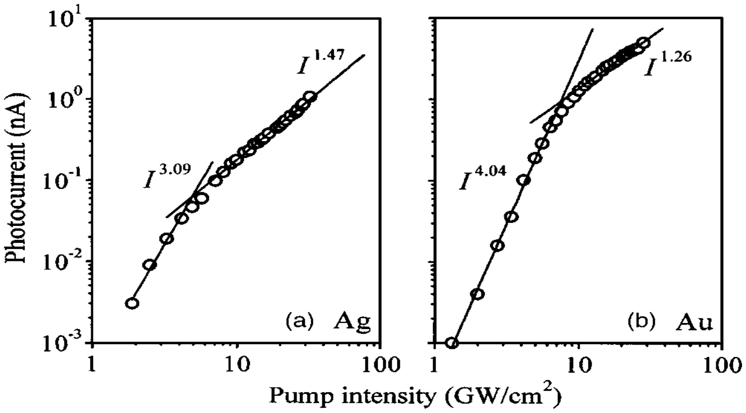

Figure 4.6: Nonlinear photocurrent dependence on excitation intensity of 800 nm (1.55 eV) pulse for: (a) Ag film (work function 4.26 eV), (b) Au film (work function 5.1 eV). From Elezabbi and Irvine [107].

4.2.2.3 Photoemission from non-symmetric gratings

Surface plasmon enhanced electron emission from metals has been intensively investigated during past 50 years, see, for example, a textbook written by Raether [95]. A femtosecond scale time-dependent approach has been done but not limited to the following groups. Perturbative by light photoemission from Cu by Kirschner and coworkers [110], angular resolved photoemission by Elezabbi and Irvine [97, 107], evanescent acceleration photoemission by Wynne *et al.* [100], multi-photon anomalous photoemission from Ag including work on image states by the group of Parmigiani [111], laser-assisted photoelectric effect from surface by the group of Saathoff [112, 113]. Spatial two-dimensional photoemission distribution has been investigated by the group of Kirchmann [114]. Gold grating has been used to show ponderomotive shift by the group of Kupersztych [104].

To the best of our knowledge, no group has deployed non-symmetric gratings for spatial, angular and temporal photo-emission analysis. The work of Kreiter *et al.* [115], was dedicated to absorption resonances in asymmetric gold gratings based on the reflectivity measurements only. The authors address this phenomena to the surface plasmon origin and provide supportive theoretical calculations.

4.2.3 Surface plasmon assisted oxygen dissociation

This work is based on the utilisation of the SP enhanced electric field on a metallic surface. Presented below results show that it is possible to find experimental conditions to satisfy SP assisted dissociation of oxygen avoiding direct photo-dissociation. See Figure 4.7 for visual explanation. Here we would like to bring some estimations supporting the idea.

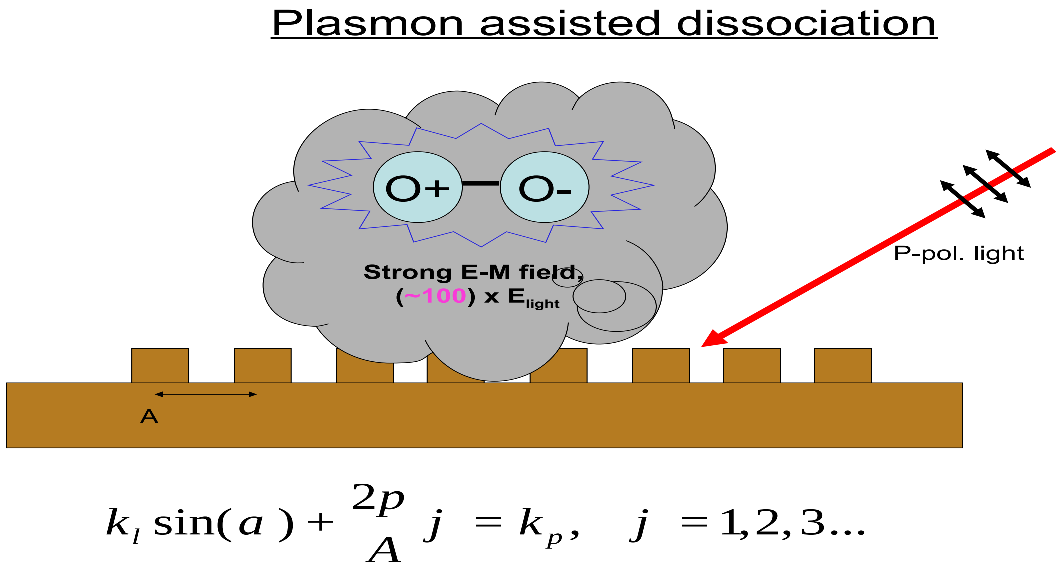

Figure 4.7: Basic principle of surface plasmon assisted molecular dissociation. Entering into an oscillating strong plasmonic resonating electric field ions of oxygen, O^+ and O^- being dissociated. An excitation beam intensity ought to be below (direct) photo-dissociation threshold.

A dissociation energy of oxygen is 498.4 kJ/mol [116] providing 5.18 eV per molecule. The Van der Waals radius of O_2 is approximately 1 $\AA$ [117]. Thus a threshold dissociation field would be the value of a dissociation energy in eV divided by the interatomic distance: 5.2 V/(2×1$\AA$)=2.6×10^{10} V/m. Optical electric field enhancement, γ, at a metal-air interface due to SP is estimated to be [118]:
$\gamma^2 \equiv |E^2_{SP}|/|E^2_{light}| \approx \epsilon'^2_m/(\epsilon''_m\sqrt{-\epsilon'_m - 1})$. Here E_{light} and E_{SP} are laser and SP electric fields respectively, while ϵ_m is given by Eq. 4.4. In the visible spectrum $\gamma \approx 10 - 100$ for gold (see Figure 4.2 for $\epsilon_m(\lambda)$ behaviour). Thus, in order to achieve SP-assisted dissociation: $E_{SP} = \gamma \times E_{light} = 2.6 \times 10^{10}$ V/m. In other worlds, the main conditions for SP-assisted O_2 dissociation are: $E_{light} << E_{SP}$ and $\gamma >> 1$. Where γ is SP resonance strength factor depending on a grating parameters (surface roughness structure), an excitation wavelength and an angle of incidence.

4.3 Technical background

4.3.1 Measurement apparatus and techniques

New femtosecond laser apparatus being utilised in this experiment is principally similar to the apparatus described in the Section 2.2.1. Shorter pulse duration of 60 fs and much better stability are the main advantages which are relevant to this experiment. This system is provided by Coherent Inc [119]. Laser beams handling methods are common to the described in Section 2.2.2.1.

Deployed ultrahigh vacuum system is equipped with Time-of-Flight (ToF) and Velocity Map Imaging (VMI) drift tube devices both dedicated to analyse dynamics of charged particles. For general overview of the experimental system see Figure 4.8. The VMI part of the apparatus is depicted on the left side of the sketch and the ToF part is on the right. The same picture is presented in the panel B of Figure 4.9 in order to get a practical understanding.

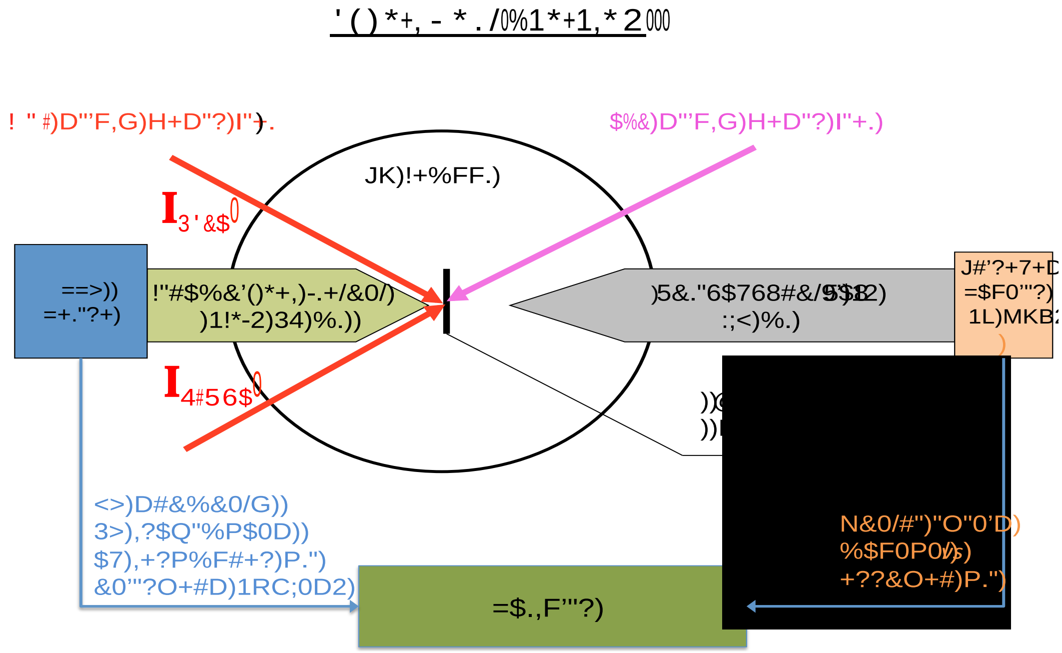

Figure 4.8: Rotation by 180° of the sample holder sets data collection from either Velocity Mapping Imaging (VMI) or Time-of-Flight (ToF) apparatus. Data combination of two regimes provides spacial, velocity and temporal information from a homogeneous sample.

A sample can be subjected to femtosecond delay controlled excitation beams at 45° from both sides of the VMI setup and from one input of the ToF setup. The VMI beams are marked as I_{left} and I_{right}, allowing femtosecond-resolved autocorrelation measurements, see

Section 4.3.1.1 for more details. Optical input ports can be better seen in Figure 4.9 panels A and B for the VMI and panel C for the ToF input. In order to switch between the setups sample holder has to be rotated by 180°.

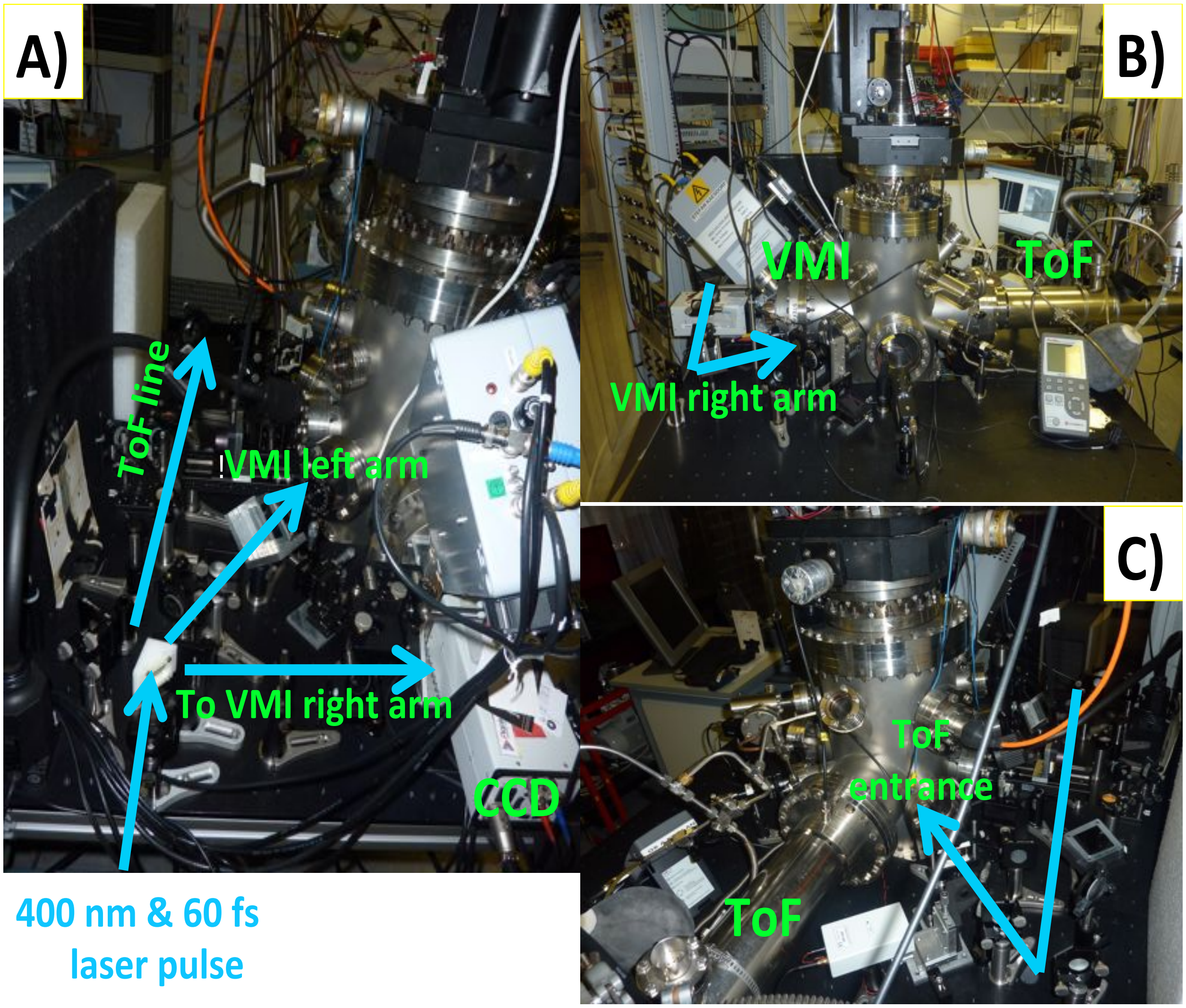

Figure 4.9: A): input of 400 nm and 60 fs laser beam, split by a beam splitter to the VMI "left" and "right" inputs and the "ToF line". The VMI accumulation imaging is done by a cooled "CCD" camera. B): side view, the VMI on the left side and the ToF on the right side of the ultra high vacuum chamber. The VMI "right" beam entrance is indicated. C): the ToF single laser entrance is indicated.

The ToF is a commercial [120] 103 cm long linear mass and energy spectrograph with energy resolution of 50 meV and time-of-flight resolution of approximately 3 ns. Signal reading is done by 4 GHz (250 ps) ultrafast single event counting A/D card provided by

FastComTec [81]. There are two static high-voltage potentials for repelling and focusing of ions and electrons towards 1-inch diameter Micro-Channel Plate (MCP) detection unit.

The VMI system is custom designed commercial [121] 25 cm long linear drift tube with position sensitive detector allowing spatial two-dimensional accumulation at a minimal time slot of 60 ns (trigger activation time). This allows two-dimensional temporal slicing of any three-dimensional ionisation event with acceptable resolution of 0.1 eV for ions. Regarding oxygen ions, the energy resolution is 0.1 eV at the range of 1 eV and 2.5 eV at the range of 30 eV of an initial ions kinetic energy. Accelerated charged particles being focused on (or spread over) 2 inch diameter MCP detector, then converted into an enhanced electron bunch projected towards photo-luminescent screen and finally detected by a cooled CCD camera as a two-dimensional image (3D slice). The design is unsuitable for time and energy resolution of electrons requiring sub-nanosecond temporal resolution. Set of four high-voltage electrostatic potentials allows to operate this devise in “Spatial” and “Velocity” modes projecting ions with respect to the initial position (spatial coordinates) or the initial velocity (momentum coordinates, k-space).

4.3.1.1 Femtosecond pump-pump photo-excitation

Meaning “pump-pump” requires additional explanation because there is no commonly used experimental technique with this name in the photonics area. To the best of our knowledge, first semiformal usage of pump-pump notation was done in the experiment carried out by Kupersztych *et al.* [104], utilising collinear beam line (in fact, it was intensity autocorrelation only). Here, we adopt these authors concept with some generalisation: pump-pump corresponds to spatially and temporary overlapped two monochromatic beams with the same intensity, wavelength and pulse duration. Within this chapter, intensity magnitude of each beam remains equal (±10%) to each other. However, not to be confused with the pump-probe conditions where the probe intensity ought to be non destructive, i.e. a few orders of magnitude lower than the pump one (see Section 2.1.5.1 for more details). Thus, a detection of emitted charged particles and further interpretation can be enriched when a temporal domain is introduced. The temporal domain is basically a delay time between two excitation pulses, similar to the pump-probe technique.

In summary, the pump-pump excitation concept includes individual control and variation of intensity and polarisation of each laser beam as well as relative delay time, where each beam produces a perturbation to the investigated system.

4.3.2 Velocity mapping method

The Velocity mapping method was firstly introduced to investigate an ions dynamics by Helm and co-workers in 1993 [93] and since that time has received scientific interest and additional development for both ions and electrons applications, which is, for example, summarised in the book of B. Whitaker [122]. Here we will discuss main basics of this method applicable to the experimental work.

4.3.2.1 Newton sphere

Light assisted dissociation of two particles with mass A and B, for instance mass A < mass B, can be written in the following form [122]: $AB + h\nu \rightarrow A + B$. Supposing photodissociation taking place in the single coordinate point, the momentum distribution of the both products creates so called Newton Spheres for each mass. For example, photodissociation created by a linearly polarised laser light is presented in Figure 4.10. Each mass A and B donates randomly distributed particles into an upper and lower hemisphere, finally creating a $cos^2\theta$ like distribution for each mass, as shown in the left panel. Thus radius of the Newton Sphere is directly proportional to the absolute value of the dissociated product speed, while angular distribution denotes its direction.

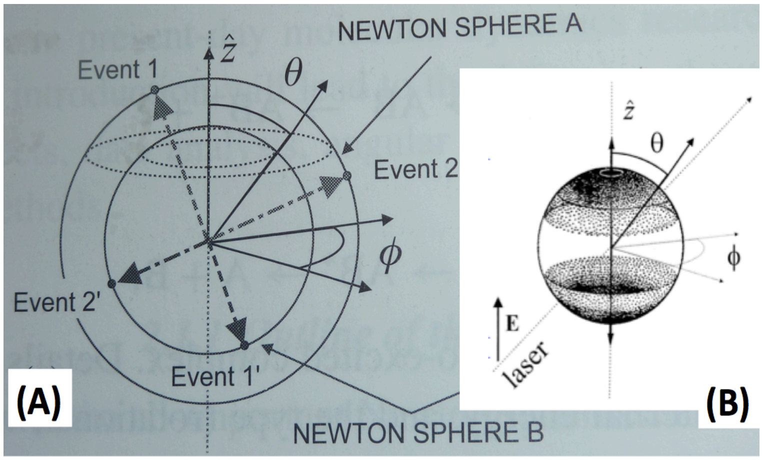

Figure 4.10: Newton spheres from laser photodissociation of particle A and B, where mass A < mass B. The distribution has $cos^2\theta$ behaviour due to linearly polarised excitation field alongside z axis. Panel A: sphere B denotes B particles distribution with shorter radius comparing to the distribution of lighter A particles. Panel B: accumulated in time distribution statistics for a single sphere only. Images are adopted from [122, 123].

4.3.2.2 Newton sphere projection

A projection of the Newton spheres of Oxygen photodissociation is shown in Figure 4.11. There are two different methods for the projection [122]. The first one is simply applying a linear electrostatic field attracting the dissociation (charged either positive or negative) by-products toward the detection screen, as indicated in the upper sequence of this figure. Basically, this is nothing else rather than an ion microscope, or simply a microscope mode.

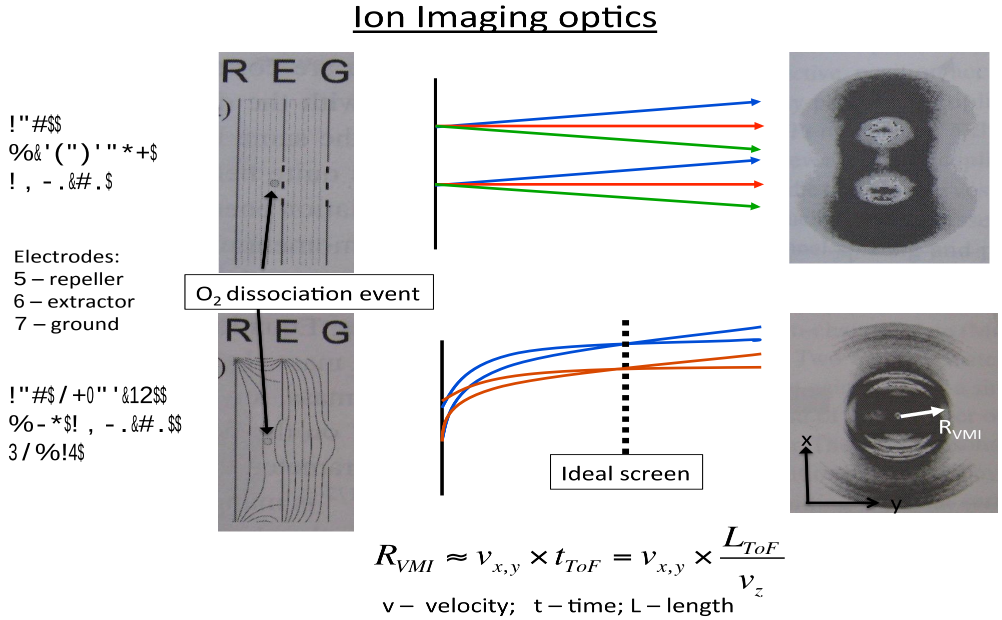

Figure 4.11: Basic principles of ion optics on the example of oxygen, O_2 photo-dissociation. Oxygen ions of the same charge being accelerated by three electrodes toward a screen. Upper part: microscope mode, linear field has been applied on the ions by the electrodes. Lower part: velocity mapping mode, non-linear field has been created by the electrodes. Images are adopted from [122].

The second method, the VMI, is based on an application of an inhomogeneous electrostatic field "focusing" charged particles in respect to their Newton spheres into 2D rings on the detection screen. The radius of such a ring will be proportional to the detector's time-of-flight axis length, parallel to the screen velocity (being proportional to the perpendicular component of the applied electrostatic field), see the lower set of Figure 4.11.

4.3.2.3 Mathematical principle

The VMI regime is valid when a few assumptions are practically fulfilled during a Newton sphere projection. Here, we would like to point out these assumptions according to [124].

Let us regard a projection process of particles originated at the coordinates $x_0 = y_0 = z_0 = 0$ towards a screen with coordinates X and Z separated a distance L in the ŷ direction. See Figure 4.10 as coordinate system and presumable process references. An initial velocity vector can be written in the following form $v_0 = \{v_0 sin(\theta)cos(\phi), v_0 sin(\theta)sin(\phi), v_0 cos(\theta)\}$ and initial kinetic energy of $E_{k0} = mv_0^2/2$ with a particle mass m and charge e. Applying a homogeneous electric field E towards the screen alongside the ŷ direction the X and Z coordinate transformations are:

$X = \frac{2Lsin(\theta)cos(\phi)}{\rho}(\sqrt{sin^2(\phi)sin^2(\theta) + \rho} - sin(\phi)sin(\theta))$,
$Z = \frac{2Lcos(\theta)}{\rho}(\sqrt{sin^2(\phi)sin^2(\theta) + \rho} - sin(\phi)sin(\theta))$, where $\rho \equiv \frac{eEL}{E_{k0}}$.

These equations can be rewritten with respect to the angular co-ordinates $\phi^{\pm}$ and $\theta^{\pm}$:
$\theta^{\pm} = arctan\{\frac{X}{Zcos(\phi^{\pm})}\}$, $\phi^{\pm} = arctan\{\frac{-2\pm\sqrt{4(\rho+1)-\rho^2(X^2+Z^2)/L^2}}{\rho X/L}\}$.

From the above equations, it follows that two different original trajectories corresponding to the same initial kinetic energy can lead to the same projected point on the detector. Providing that an actual photodissociation area (typically 100 μm^2) infinitesimally smaller than the detector's area (order of 100 cm^2) it makes the momentum mapping independent on the initial spatial position.

In order to get a positive root from the last equation a radius $R = \sqrt{X^2 + Z^2}$ of the projected image has to be limited by $R \leq 2L\frac{\rho+1}{\rho}$ value. Practically, a detector with an effective radius R_0 will define a minimal value for ρ, namely $\rho_{min} = \frac{1+\sqrt{1+R_0^2/L^2}}{R_0^2/2L^2}$. For large ρ it can be reduced to $\rho_{min} = (\frac{2L}{R_0})^2$.

The simplest case for a 3D back reconstruction (to be discussed in details in Appendix D) of the X and Z projection is when $\rho \to \infty$, reducing X and Z to be $X = 2Lsin(\theta)cos(\phi)/\sqrt{\rho}$ and $Z = 2Lcos(\theta)/\sqrt{\rho}$. This makes the technique suitable for particles' initial energy much smaller comparing to the applied electromagnetic fields as it follows from the definition of ρ.

4.3.3 Samples

The main samples are two commercial holographic asymmetric gold gratings from different makers. A periodic pattern of the first sample is 300 grooves/mm at a blazing angle of 8°36′ according to the manufacturer [125]. The second sample characteristics are 150 grooves/mm at a blazing angle of 26.7° as provided by the maker [126]. A schematic view and basic definitions of an asymmetric grating are depicted in the Figure 4.12. A positive grating direction denoted with respect to the blazing angle and is indicated by an arrow. Thus negative grooves direction is the opposite direction of the arrow. Typical bare gold film thickens is $200 - 500$ nm.

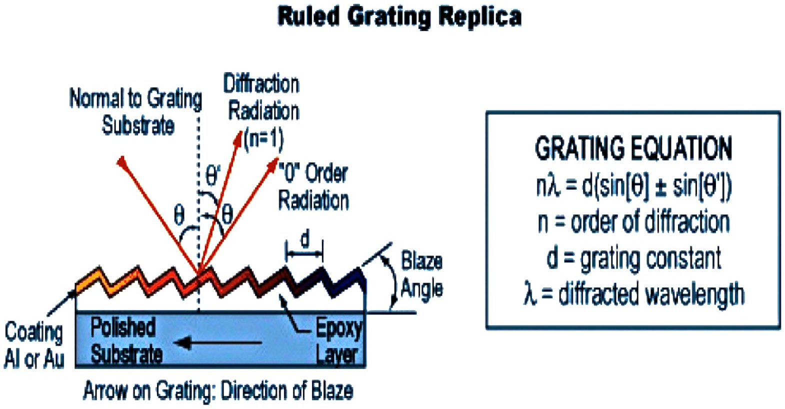

Figure 4.12: Schematic description of the asymmetric gold grating, taken from the maker's technical data [125].

4.3.3.1 Surface plasmon resonance strength characterisation

Plasmon excitation efficiency characteristic in the $410 - 750$ nm wavelength range has been measured alongside the positive and negative directions to the grooves blaze. This has been achieved by a reflectivity measurements of non-zero order for linearly $p-$polarised and $s-$polarised light. Results are presented in Figure 4.13 as a normalised difference between S and P reflected beams of non-zero orders. Namely, the ratio is $(R_s - R_p)/(R_s + R_p)$, ranging theoretically from 0 to 1 and indicating either an absence or maximal possible (100% light resonant absorption) SP resonance. As it follows from the solution of Maxwell equations, for example [127], only p-polarised light can couple to SP, here we disregard a local SP effect which is polarisation independent [128]. For this measurement cooled CCD camera has been utilised, while its wavelength spectral response (quantum efficiency of the CCD array, lens, etc.) has been taken into account. Due to different optical components being used for the visible and near infrared spectrum, the presented curves show a discontinuity in the vicinity of 680 nm. Nevertheless, general behaviour is consistent between visible and near infra red measurements for the overlapping range (670 – 690 nm) apart from the negative direction of the 300 grooves/mm grating, depicted by the green curves.

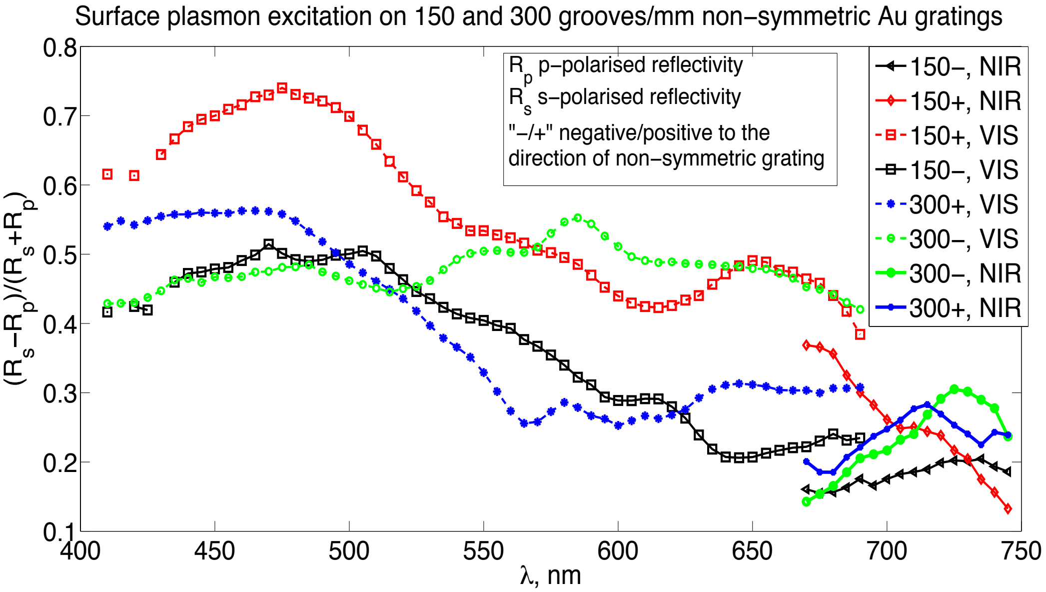

Figure 4.13: Reflectivity measurements of non-zero order for 150 and 300 grooves/mm gold gratings. Normalised difference in *s*- and *p*- linearly polarised light beams represents surface plasmon excitation efficiency in the visible and near infrared spectrum of 410 – 750 nm.

As can be seen from Figure 4.13, the highest contrast ratio between irradiation by $s-$ and $p-$polarised light is achieved in the 410 – 525 nm region for both gratings, indicating stronger SP excitation. As a result, most of the experimental work has been done at 400 nm excitation wavelength, providing good SP resonance condition. However, choosing this wavelength introduces particular asymmetry in the SP resonance strength when the negative and positive directions have been chosen for the irradiation. This subject will be addressed in the experimental results discussion paragraph.

4.3.4 Basic apparatus tests

In order to ease understanding of the experimental results brought in the next paragraph, we would like to present two typical experimental outputs by the VMI and ToF setups. Presented below are "test-mode" measurements of Oxygen photo-dissociation by the VMI apparatus and gold grating ablation detected by the ToF apparatus.

4.3.4.1 Oxygen photodissociation

Typical Velocity Map Imaging measurement has been done by means of a very strong (comparing to the surface plasmon measurements) pulse of 1.5 W per 100 μm (an equivalent of 1.5×10^5 GW/cm^2 for future reference) in diameter of the spot cross section. An infra red 800 nm (1.55 eV) 100 fs pulsed beam has been focused in the vacuum with oxygen gas pressure of 1×10^{-6} mbar. The 2D projected velocity mapping is depicted in the Figure 4.14. Oscillating electric field has been applied in parallel to the VMI entrance (parallel to the projection screen as well). Strong field caused random separation of the oxygen molecules into O^+ and O^- atoms alongside the oscillation direction. Negative electrostatic potentials have been applied to bring the positive products to the imaging screen, getting all negative ions to be lost for detection. Both opposite peaks form the accumulated positive oxygen products being accelerated toward both ends of the oscillating field. Due to mass difference of the detected ions, momentum separation it is clearly seen between O^+ and heavier O_2^+ clusters. Central spot corresponds with a background of H^+ atoms. The image presented in the accumulation regime, when time-triggering (3D slicing) is not in use.

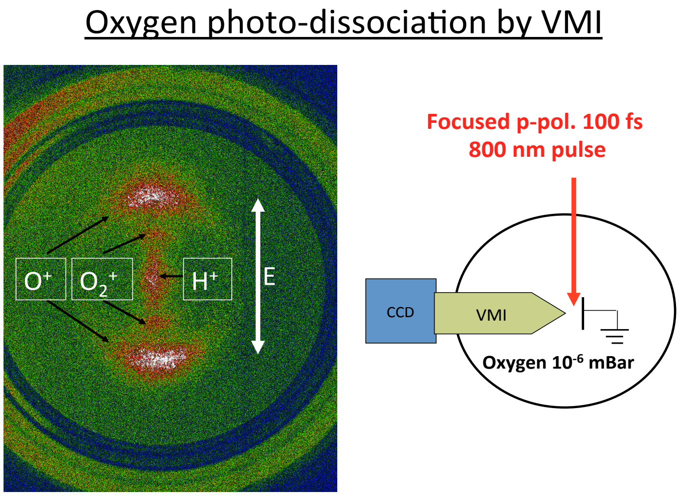

Figure 4.14: Oxygen photodissociation using dense 800 nm (1.55 eV) pulse resolved by Velocity Map Imaging. The byproducts in the 2D velocity coordinates: (light) Hydrogen ions, H^+, O^+ and (heavy) O_2^+ clusters. Schematic view of the experiment depicted on the right. Electric field oscillation direction depicted by the E labeled arrow.

4.3.4.2 Gold film ablation

In order to treat correctly the ToF results of various mass ions, an ablation measurement from the Au 150 gr/mm grating has been done. The recorded data is presented by the red curve in the Figure 4.15. Various ablation products are indicated by the text boxes near corresponding yield peaks. Peaks with 100% understanding are mainly consisted of Hydrogen, Carbon and gold clusters. The time-of-flight of these clusters has been matched with simulation results produced by commercial electromagnetic projection software tool, Simion v8 [129]. The calibration curve matching is presented in the inset of Figure 4.15. The initial ions/clusters energy for the simulation has been associated with up to 1 eV, providing an error margin below 5%. The energy scale order of 1 eV arises from an estimation of the initial kinetic energy of O_2 dissociation products by means of a two-photon photo-dissociation: $2 \times 3.1 - 5.2 = 1$ eV. Here first term reflects two-photon energy and the second term is a work function of gold in eV.

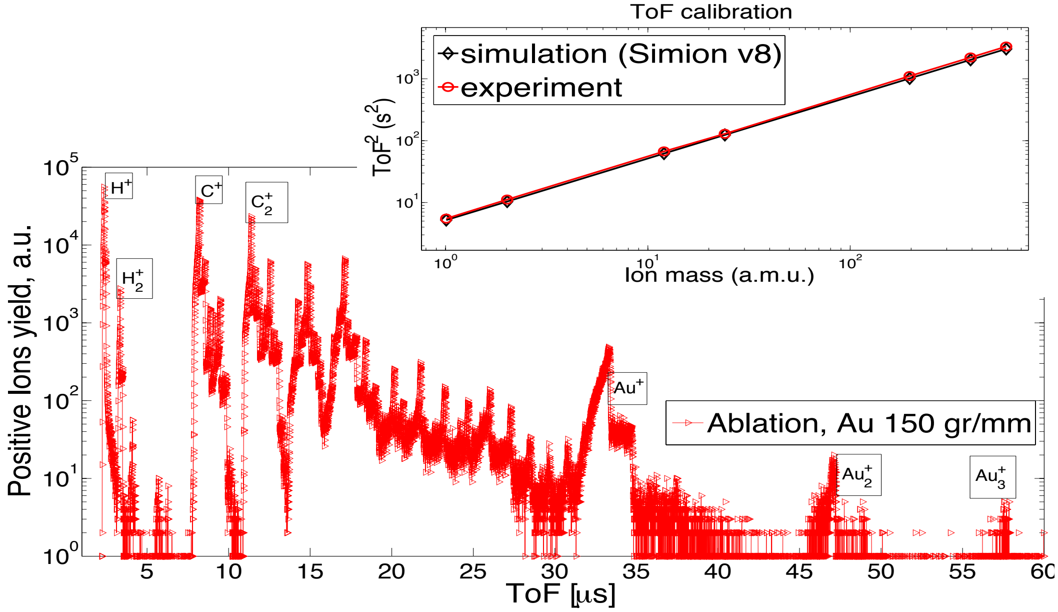

Figure 4.15: An ablation from Au 150 gr/mm grating. Main products of H, C and Au are indicated. Inset: calibration of a time-of-flight to the products mass is calculated using commercial software ions trajectory simulation tool, Simion v8.

4.4 Experimental results

Data presented in this paragraph is organised in the following order:

- *Surface plasmon enhanced photoelectron emission* part is dedicated to electron emission analysis by the VMI and ToF tools.
- *Surface plasmon assisted oxygen dissociation* part shows evidence of oxygen dissociation as detected by the VMI and ToF tools.
- *Time-resolved Surface plasmon assisted oxygen dissociation* part describes autocorrelated oxygen dissociation analysed by the VMI apparatus.

4.4.1 Surface plasmon enhanced photoelectron emission

An observation of SP enhanced electron emission from Au gratings is, probably, the simplest way to get qualitative knowledge of a strength of the SP resonance fields required for the oxygen dissociation.

4.4.1.1 Electron emission and reflectivity from gold grating

Spatial two-dimensional projection measurements of an electron yield from Au surface detected by the VMI system is depicted in Figure 4.16. Projections have been accumulated for various linear polarisation states: beginning from s-polarised towards p-polarised and further towards s-polarised by gradual rotation of a half wave plate. Gold 300 grooves/mm grating was subjected to linearly polarised 800 nm (1.55 eV) and 60 fs pulse width at 30 GW/cm^2 per pulse beam passing through polarisation controlling half wave plate. Assigning s-polarisation to be 0° and p-polarisation respectively 90° (with a full period of 180°). There are 18 snapshots each taken with a 10° step (5° when rotating a half wave plate). Significant qualitative change in the electrons yield can be easily noticed as the light polarisation changes towards conditions required to match one of the SP resonance modes. When light projection polarisation becomes perpendicular to the grating grooves, the resonance achieves its maximum.

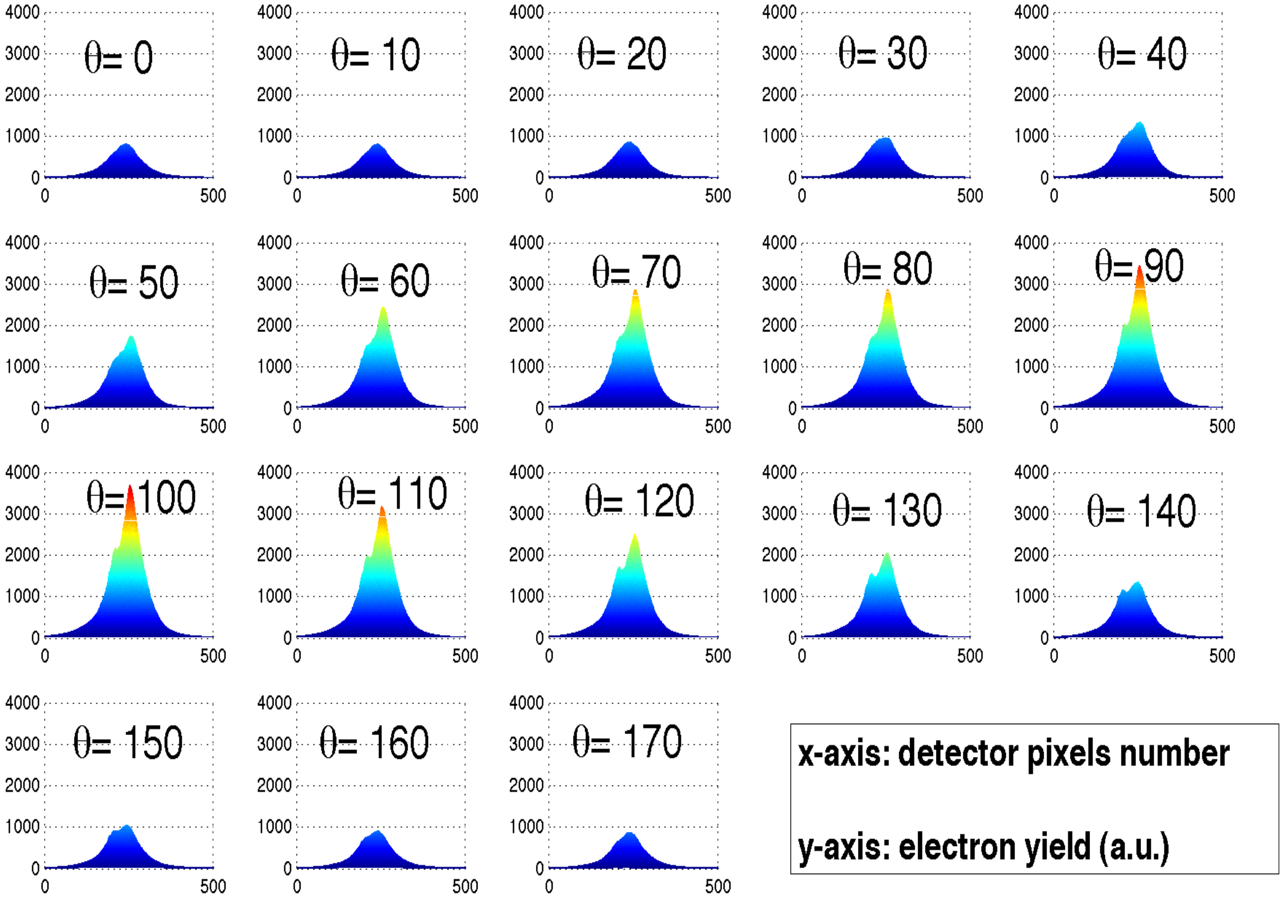

Figure 4.16: Spatial 2D projection of an electron emission yield from gold, 300 grooves/mm, grating vs linearly polarised 800 nm at 60 fs excitation pulse. Angle of approximately 90° denotes pure p-polarised light, while pure s-polarisation is achieved at approximately 0° and 180°.

Quantitative summary of the 18 snapshots of the electron yield is depicted in the left panel of Figure 4.17. Presented two curves denote a couple of various settings of the electrostatic lenses conditions of the VMI system. In addition to the electron yield, simultaneous reflectivity measurement has been taken and shown in the right panel of Figure 4.17. Reflectivity minima shows matching of the SP resonance mode and coincides, within an experimental accuracy, with the enhanced electron emission due to the SP excitation.

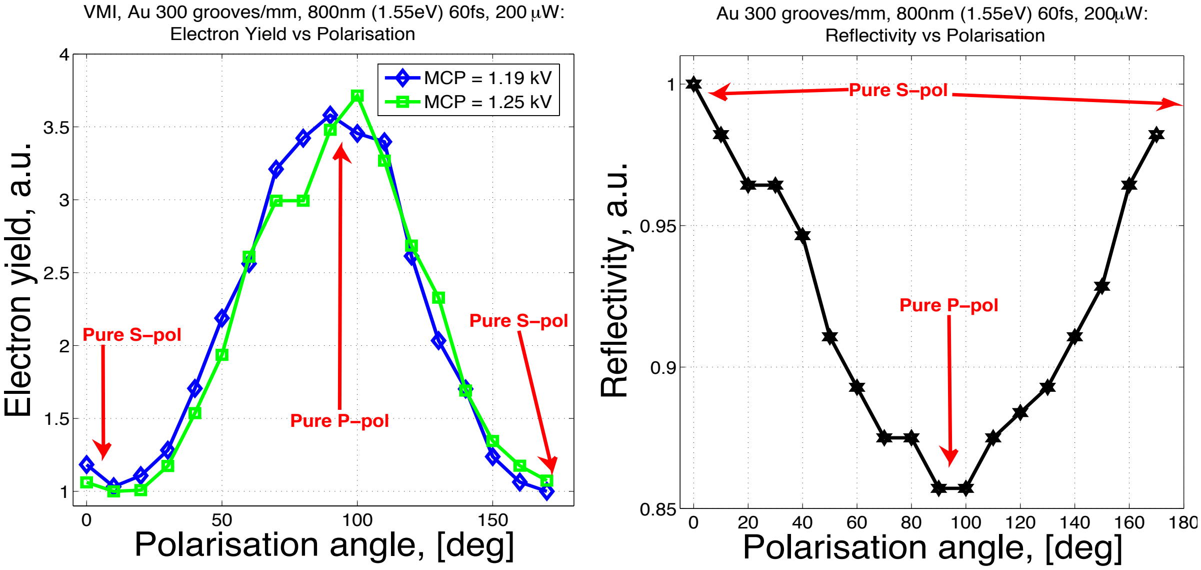

Figure 4.17: Electron emission yield (left panel) and light reflectivity (right panel) from gold, 300 grooves/mm, grating vs linearly polarised 800 nm (1.55 eV) excitation beam. Angle of approximately 90° denotes pure *p*-polarised light, while pure *s*-polarisation is achieved at approximately 0° and 180°.

The above surface plasmon enhanced electron emission picture is essential for understanding the main principe of the carried out experiment and correct result treatment.

4.4.1.2 Order of nonlinear emission at low-intermediate intensity range

Meaning of “low”, up to 10 GW/cm^2, and “intermediate”, $10 - 100$ GW/cm^2, intensity ranges have been assigned due to observed differences in the emission behaviour.

The work function of gold is 5.1 eV according to Sommer [130] requiring, in the case of non-thermal emission, a two-photon precess for 400 nm (3.1 eV) light source. Presented in Figure 4.18 is an electron yield from Au gratings 150 and 300 gr/mm being exposed to the 400 nm laser pulses at various intensity range of $2 - 100$ GW/cm^2.

Nonlinear behaviour of all three curves can be divided into a couple of regions. The first region with lower excitation intensity corresponds to a two-photoelectron emission with a nonlinearity order of $NL = 1.8$ and 1.9 for Au 150 and 300 gr/mm respectively. The second region represents high intensity and indicates nearly one-photon photoemission from Au 150 gr/mm grating, providing $NL = 0.8$. These results for gold are in good agreement with the published data [107], see Section 4.2.2.2. The authors report $NL_1 = 4.04$ and $NL_2 = 1.26$ deploying 800 nm (1.55 eV) excitation of gold film (factor of 2 need to be taken into account due to 3.1 eV/1.55 eV excitation energy difference); photo-emission at the NL_2 region being attributed to a tunnelling ionisation [108] of Au film.

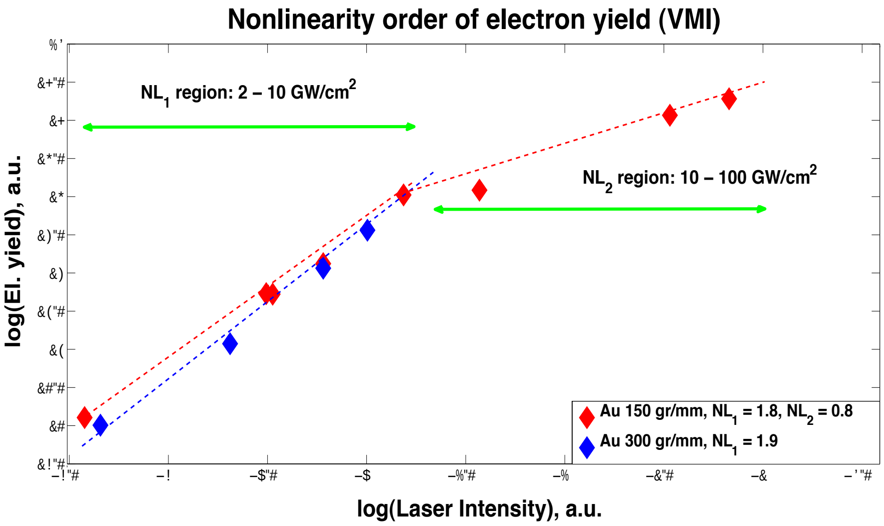

Figure 4.18: Nonlinear photoelectron yield from gold 150 and 300 gr/mm gratings for excitation intensities of $2-100$ GW/cm^2. NL_1 region merges with NL_2 region at approximately 10 GW/cm^2. Note, data is presented in a logarithmic scale.

4.4.1.3 Order of nonlinear emission at high intensity range

High intensity range, of approximately $200 - 800$ GW/cm^2, is a typical range for detection of oxygen dissociation. This measurement provides knowledge of the background electron emission nature important.

The time-of-flight spectrum measurements have been done focusing on the photoemission from Au 150 gr/mm grating. The ToF apparatus can indicate not only emission yield magnitude but also initial kinetic energy of free electrons. The results are brought in Figure 4.19. Shown in panel A is ToF spectrum at both p- and s-polarisations. The clearly seen emission peak corresponds to the kinetic energy of 1.7 eV and FWHM of $\Delta E_k = 0.2$ eV. Summary of electron yield magnitude as a function of excitation intensity is presented in the panel B, indicating an order of nonlinearity to be $NL = 1.2$. The difference between order of nonlinearity at the intermediate range, $NL = 0.8$ (see Figure 4.18) and high intensity range, $NL = 1.2$ remains unclear. A reference to these values will be done along the lines of oxygen dissociation discussion in the following sections.

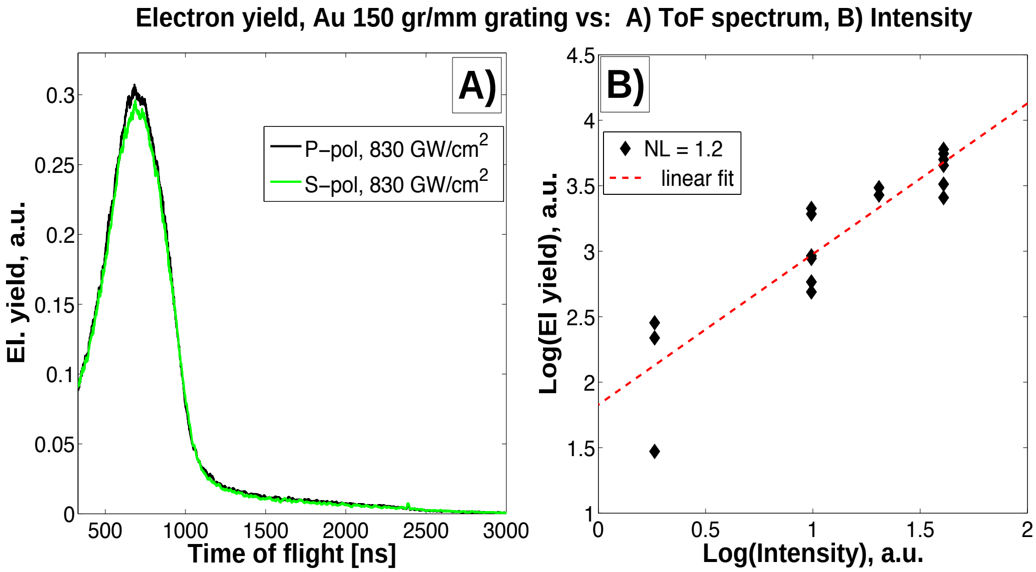

Figure 4.19: Electron yield from Au 150 gr/mm grating: A) Time-of-Flight spectrum for 830 GW/cm^2 p- and s-polarised photo-excitation. The emission peak corresponds to the kinetic energy of 1.7 ± 0.1 eV. B) As function of intensity in the $200 - 830$ GW/cm^2 range. Order of nonlinearity is $NL = 1.2$.

4.4.2 Surface plasmon assisted oxygen dissociation

This paragraph is dedicated to the experimental evidences of dissociation of oxygen molecules by means of photo-excited sufficiently strong surface plasmon fields, keeping the excitation intensity below the photodissociation threshold (approximately 5000 GW/cm^2, see also Section 4.3.4.1). The dissociation byproducts, O^+ and O^- ions have been analysed in both Time-of-Flight and Velocity Mapping Imaging mass-spectrographs. The nature of this process has strong non-linear behaviour followed by high level of noise and low rate of repeatability of the results. In average, the extracted nonlinearity order is found to be $NL = 4 \pm 0.5$.

4.4.2.1 Oxygen dissociation evidence by VMI setup

Imaging of an angular distribution of $O^\pm$ has been conducted by the VMI apparatus deploying it in the microscope mode (see Section 4.3.2.2). Each distribution corresponds to the positive or negative oxygen ions as a result of SP assisted dissociation. Figure 4.20 describes the 2D projection process on the example of O^- ions yield being detected from Au 150 gr/mm grating when p-polarised 400 nm and 60 fs laser beam at typical intensity of 300 GW/cm^2 has been applied. An excitation laser beam is focused on approximately $10^4 \mu$m^2 spot area

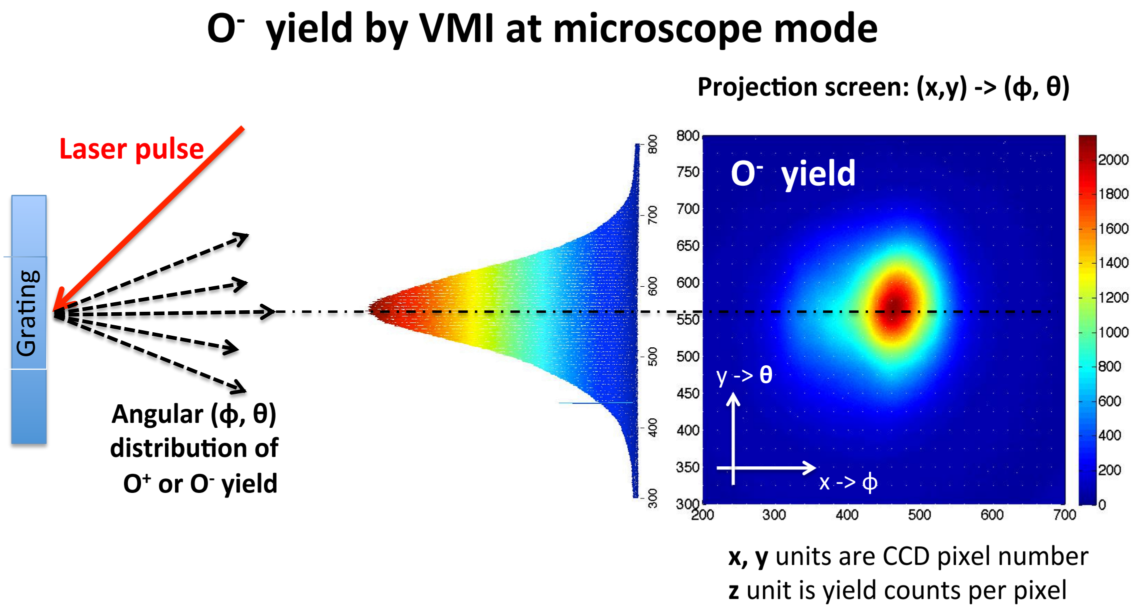

Figure 4.20: Two-dimensional spatial distribution of molecular oxygen (O_2) dissociation products ($O^\pm$ ions) yield. The dissociation process is assisted by surface plasmon resonance excited by 400 nm, 60 fs, p-polarised laser pulse at 300 GW/cm^2 on the 150 grooves/mm gold grating.

of a Au grating leading to a SP excitation. Externally injected O_2 gas (not shown) being dissociated by the strong SP field causing O^- and O^+ yield. Due to charge selective electric potentials applied to the VMI, ions with either positive or negative charge can be detected at one time. A dissociation taking place at a single point can be described by an angular distribution (ϕ, θ), as shown schematically. Thus, 2D distribution in the x and y plane can be associated with the angular distribution only. In more complex situation, an origin of the dissociation cannot be regarded as a single point but as a spatial distribution. Careful treatment of the projected yield can be done by means of Simion projection simulation software, however it is beyond the scope of this work.

A summary of oxygen molecule dissociation after an irradiation of the Au 150 gr/mm and 300 gr/mm gratings by s- and p-polarised 400 nm and 60 fs laser beam at typical intensity of 300 GW/cm^2 is shown in Figure 4.21. Data of the top left image, O^- p-pol Au150 gr/mm, has already been shown in Figure 4.20.

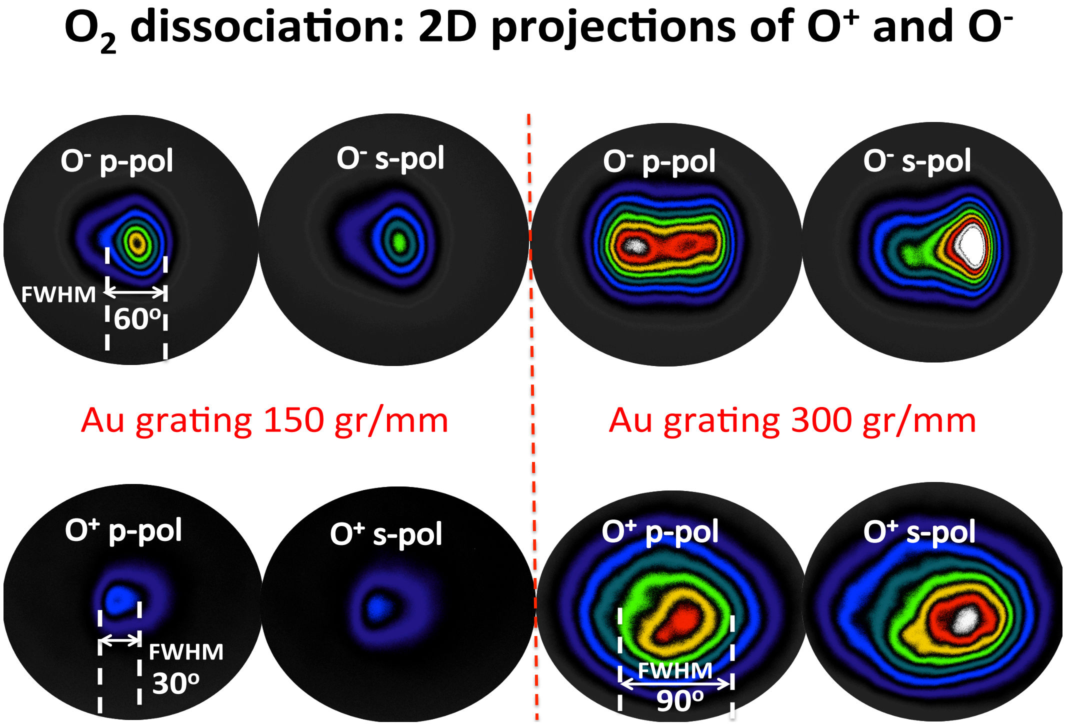

Figure 4.21: Two-dimensional spatial distribution of molecular oxygen (O_2) dissociation products ($O^{\pm}$ ions) yield. The dissociation process is assisted by surface plasmon resonance excited by 400 nm, 60 fs laser pulse at 300 GW/cm^2 on gold (Au) gratings with period of 150 and 300 grooves per mm. Data presented for linear beam polarisation at S (s-pol) and P (p-pol) states. Estimated angles of cone-like yield distribution are shown at the FWHM.

Note, a scale level is different for each grating. The highest ions yield corresponds with the negative ions for the 150 gr/mm grating subjected to p-polarised beam. Overall yield of O^- ions is significantly higher than O^+ ions one. Regarding the data from the 300 gr/mm grating, s-polarisation overall leads to higher yield for both oxygen ions. Estimated distribution angles at the FWHM are: for O^+, 30° and 90° from the Au 150 gr/mm and 300 gr/mm gratings respectively; for O^-, 60° from the Au 150 gr/mm grating. The yield distribution of O^- from the Au 300 gr/mm grating shows two peaks (two dissociation points) being strongly polarisation dependent.

4.4.2.2 Nonlinearity of oxygen dissociation

Presented in Figure 4.22 is O^- ions yield upon excitation intensity as detected from the Au 150 gr/mm and 300 gr/mm gratings depicted by black and red curves respectively. The intensity range was $170 - 750$ GW/cm^2. The insets are typical 2D ions projection images detected by the VMI apparatus, as shown in the previous Figure 4.21. An integrated image information corresponds to a single point on the respective curve. The nonlinearity order of the ionisation process has been denoted by the following indexes $NL = 3.6$ and $NL = 4.5$ for the 150 gr/mm and 300 gr/mm gratings respectively.

Figure 4.22: Surface plasmon assisted O^- nonlinear yield from Au 150 and 300 gr/mm gratings. Excitation intensity range $170 - 750$ GW/cm^2. The insets are typical 2D ions projection images detected by the Velocity Mapping Imaging apparatus.

4.4.2.3 Oxygen dissociation evidence by ToF setup

In addition to the VMI results, oxygen dissociation has been resolved by means of the ToF apparatus. Its outstanding resolution and sensitivity have shown more complex structure of the O^- ions yield peak than being detected by the VMI. Heavier ions originate a background of almost 10% of the total yield. Despite the VMI was operated in a mass-selective (time triggered) mode, it was practically not trivial to filter out these contributions. Thus, the following ToF results reflect a more accurate picture of the O_2 dissociation process.

Logarithmic plot of almost four sequential mass elements following the O^- ions have been mass-resolved and are shown in Figure 4.23. There are at least two well observed peaks with masses of 17 amu and 18 amu. Most probably, the background water molecules dissociation ($H_2O \longrightarrow HO^- + H^+$) are the source for the second, 17 amu peak that contributes approximately 10% of the total yield. Particles trajectory simulation results (obtained by Simion v8) have been depicted by black vertical lines in good agreement with the experimental results. During the simulation, an initial kinetic energy has been chosen to be below 0.05 eV.

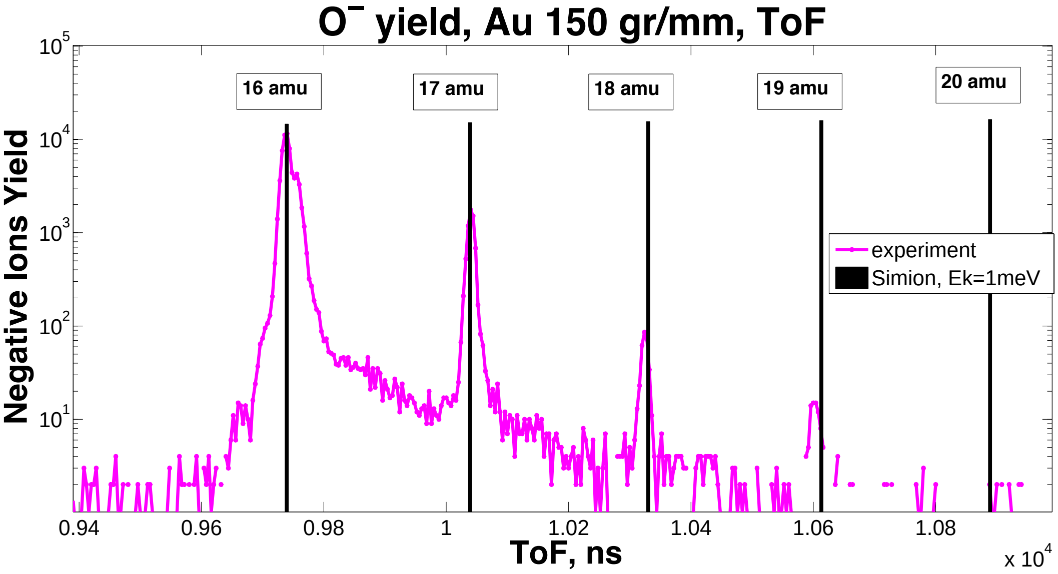

Figure 4.23: Time-of-flight spectrum of negative ions yield in the range of $16 - 20$ amu from Au 150 gr/mm grating. Ions trajectory simulation results are depicted by the black columns.

4.4.2.4 Minimum intensity threshold for oxygen dissociation

In order to find a minimum intensity value required to observe oxygen dissociation, excitation intensity measurements have been conducted by means of (more sensitive than the VMI) ToF setup. A threshold intensity was found to be as little as 50 GW/cm^2.

Results of an order of the nonlinear dissociation yield can be seen from the ToF spectrum analysis as shown in Figure 4.24. This figure represents a summary of the negative ions yield as a function of the excitation intensity and polarisation, in the range of 50 – 700 GW/cm^2. An average nonlinearity order of the O^- peak is found to be $NL = 3.7 \pm 0.1$ in excellent agreement with the VMI results, see Figure 4.22. The background contribution should be taken into account for a careful analysis. The inset shows an example of the ToF spectrum: main peak labeled as O^- is pure O^- yield while two other peak yields, labeled as *(2)* and *(3)*, represent to be subtracted background yield.

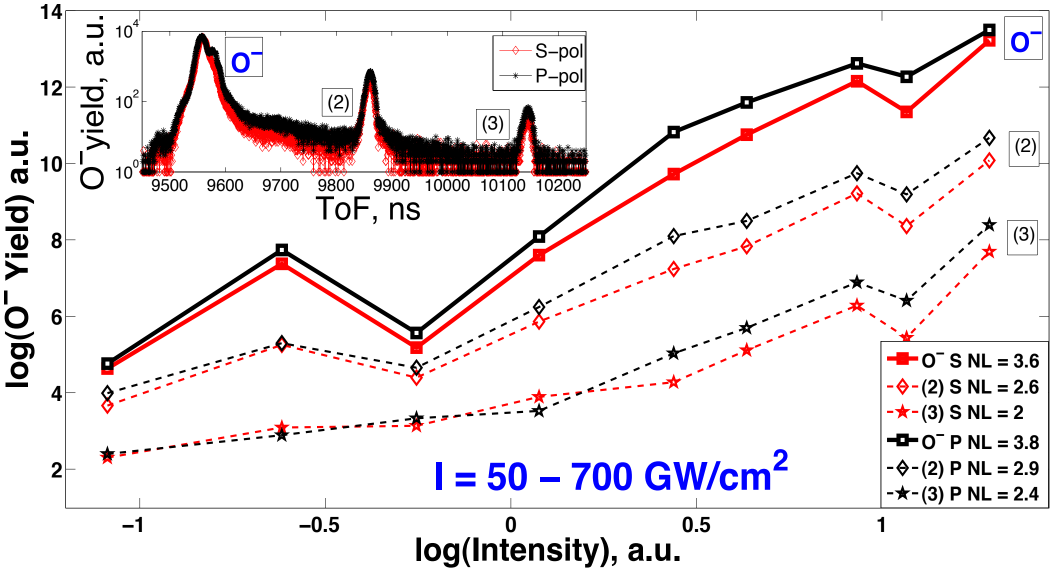

Figure 4.24: Surface plasmon assisted O^- nonlinear yield from the Au 150 gr/mm grating vs intensity range of 50 – 700 GW/cm^2 obtained from Time-of-Flight spectrum at p and s polarisations. The background of HO^- *(2)* and 18 amu ions *(3)* is shown. Inset: Time-of-Flight spectrum example of signal to background yield in a logarithmic scale.

The nonlinear behaviour of the consecutive peaks, *(2)* 17 amu attributed to HO^- and *(3)* 18 amu, is in order of $NL_{17} = 2.75$ and $NL_{18} = 2.2$ respectively. Significantly different NL of oxygen peak on the one hand, and the *(2)* and *(3)* peaks on the other hand, is unclear, despite a dissociation process being responsible for the O^- and HO^- formations.

In all cases, the highest yield amplitude being achieved at the p-polarisation indicating SP involvement (note, the presentation is in a logarithmic scale).

4.4.2.5 Dissociation as function of gas pressure

Linear dependence of the oxygen dissociation yield on the externally injected O_2 gas pressure in the chamber has been observed for both O^- and O^+ products, as expected. See results for the Au 150 gr/mm grating, within an experimental accuracy of 10%, on the left panel of Figure 4.25. Dissociation yield changes by almost 1.5 orders of magnitude at O_2 pressure range of $1 \times 10^{-7} - 5 \times 10^{-5}$ mbar.

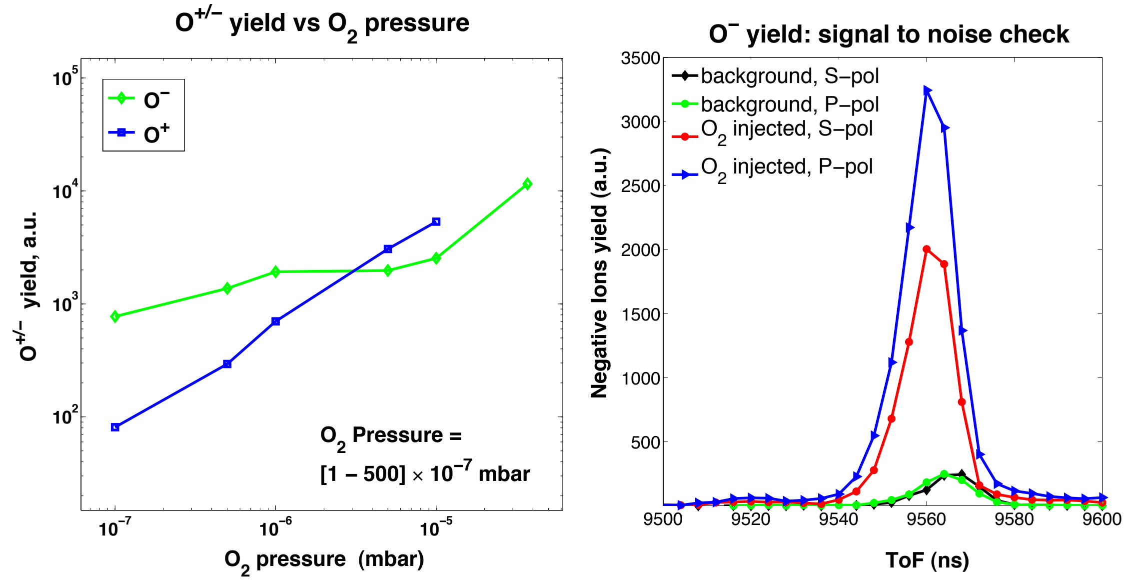

Figure 4.25: Left panel: surface plasmon assisted dissociation of O^- and O^+ linear yield vs O_2 gas pressure in the chamber for Au 150 gr/mm grating. Pressure range is $1 \times 10^{-7} - 5 \times 10^{-5}$ mbar. Right panel: signal and residual background time-of-flight spectrum of O^- from Au 150 gr/mm grating. Residual amount of oxygen remained in vacuum chamber contributes to the background spectrum. Data presented for *p*- and *s*-polarised excitation beam.

Residual background contribution

There was always residual background O_2 molecules in the vacuum chamber. Thus even at an absence of externally injected oxygen gas, there was nonzero yield of oxygen ions. However, this background contribution was just a few percents to the typically observed signal, as shown in the right panel of Figure 4.25. The green and black curves, labeled as "background, S-pol" and "background, P-pol" represent a background yield for *s*- and *p*-polarisations. Typical (O_2 pressure 5×10^{-6} mbar) ions yield amplitude due to externally injected oxygen gas depicted by the blue and red curves denoting *s*- and *p*- excitation beam polarisation states.

4.4.3 Time-resolved surface plasmon assisted oxygen dissociation

In addition to the irradiation by a single beam, Au 150 gr/mm gating has been subjected to an intensity autocorrelation excitation which will be addressed as "pump-pump" excitations. The principle of an intensity autocorrelation has been already described in Section 2.2.1.1, while temporal separation procedure of both beams is similar to the pump-probe measurements, see Section 2.2.2.1. Equal intensity Mach-Zehnder interferometer configuration at ±45° has been utilised, see Figure 4.8. In this measurement both pulses contribute to a perturbation of the system, thus, the name "pump-pump" is more suitable for the explanations.

Detection products are $O^{\pm}$ ions. The pump-pump measurements have been conducted under the following conditions: oxygen pressure in the chamber 4.4×10^{-6} mbar, an equal intensity of both beams set to 330 GW/cm^2, yield integration time was 2 s, providing an accumulation of 2000 pulses per single measurement.

Figures 4.26 and 4.27 demonstrate the obtained results in three various presentations, labeled as A), B) and C). Indexes S and P correspond to p- and s- linear polarisation state of each excitation beam, while their combination describe the pump-pump excitation. For example, PS means p-polarised left arm beam and s-polarised right arm beam. Shown in the panel A) are raw data of the pump-pump dissociation yield accompanied by the yield contributed from each single beam. Both contributions from the left arm are denoted as $S0$ or $P0$ while contributions from the right arm are denoted as $0S$ or $0P$ respectively. Panel B) shows the background subtracted pump-pump data. This background is actually a contribution to the dissociation yield from the well-separated in time pump-pump pulses. Panel C) summarises the pump-pump contrast ration being normalised to the background yield, as it has been defined earlier by Eq. 4.6: $CR = (I_1 + I_2)^{NL}/(I_1^{NL} + I_2^{NL})$.

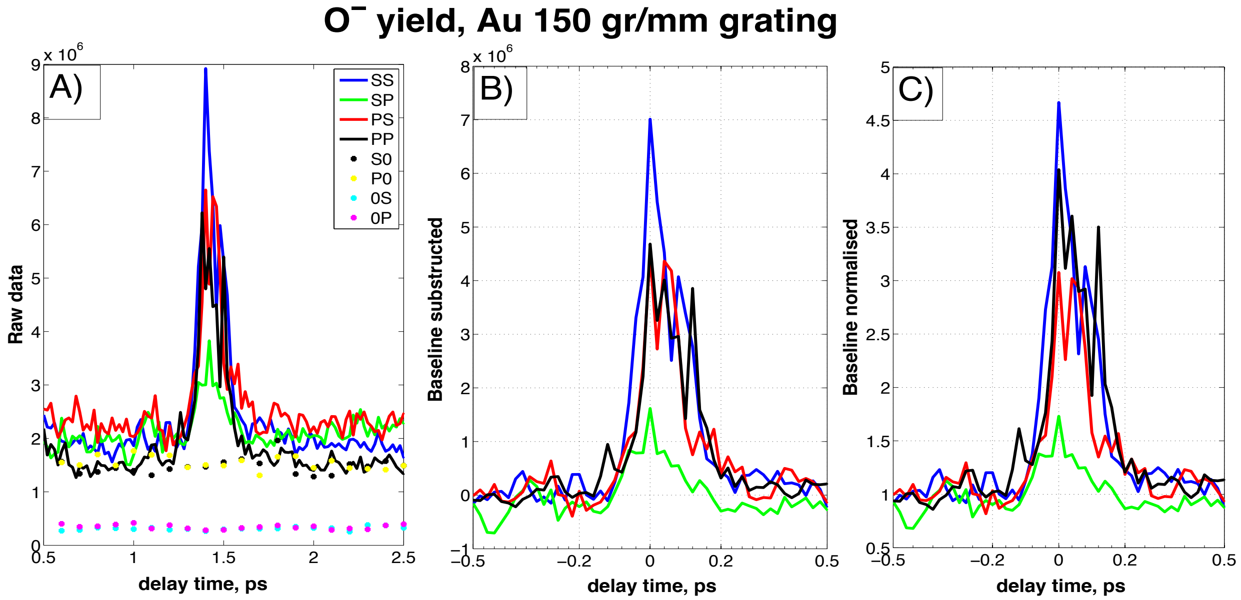

Figure 4.26: O^- yield as a product of O_2 surface plasmon assisted dissociation in the vicinity of Au 150 grooves/mm grating. Central peak corresponds with pump-pump full temporal and spatial overlap. Laser intensity of each arm is 330 GW/cm^2.

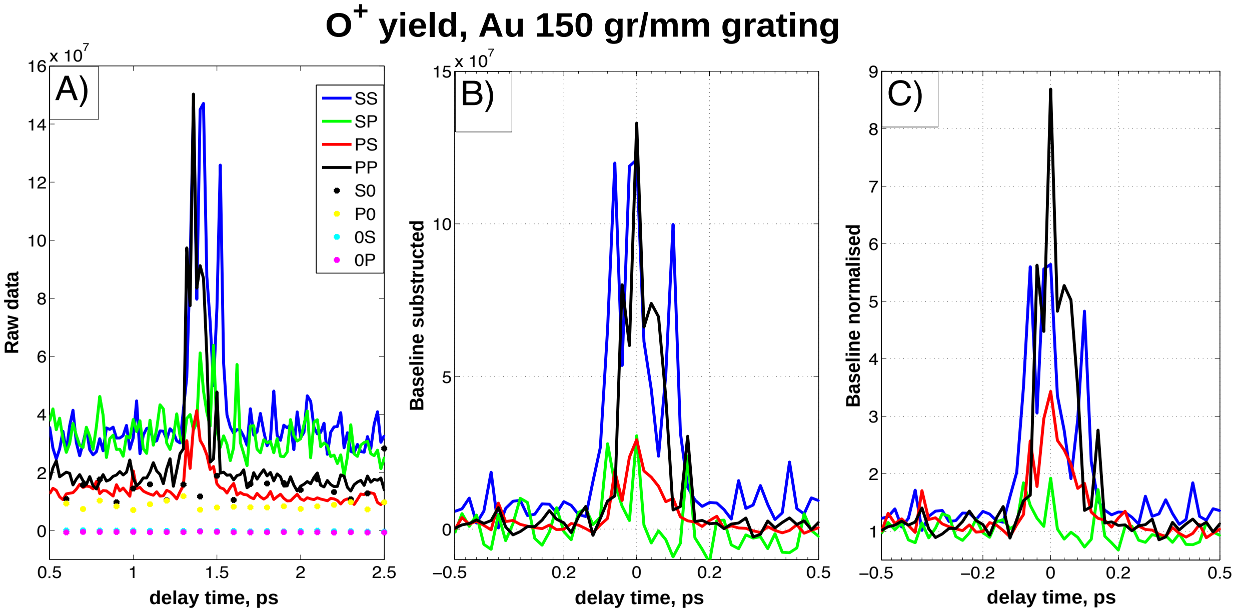

Figure 4.27: O^+ yield as a product of O_2 surface plasmon assisted dissociation in the vicinity of Au 150 grooves/mm grating. Central peak corresponds with pump-pump full temporal and spatial overlap. Laser intensity of each arm is 330 GW/cm^2.

Despite irradiation by equal intensities, $I_1 = I_2$, the yield rate of both O^- and O^+ ions is significantly different for each arm. In fact, major contribution to the yield came from the left arm (I_1).

It is not straightforward to determine a FWHM of the dissociation yield peaks because of noisy and strictly non-Gaussian form. However, it is clearly seen that any peak waist does not exceed 150-200 fs. This number scales well with the convolution of two 60 fs pulses, being in order of 100 fs.

Remarkably high pump-pump peak magnitude occurs at PP, SS and to some extent, PS laser beams polarisation states for both $O^{\pm}$ ions. Defined by Eq. 4.6 peak magnitude to a baseline contrast ratio is $CR \approx 4 - 9$ (see panel C in both Figures 4.26 - 4.27), indicating a strong nonlinear character of the O_2 dissociation process. The contrast ration at the SP (green curve) polarisation state is weakly resolved $CR \approx 1/2$.

In addition, an attempt to measure a pump-pump electron yield (at the same strong intensity of 330 GW/cm^2) has been done, however, no contrast ratio was observed, $CR = 0$. Note, the actual intensity range where time-resolved electron emission has been observed is $2 - 10$ GW/cm^2 only (for more details, see Appendix E). It is possible to conclude that the contrast ratio in the dissociation yield is not stimulated by the electron emission.

4.5 Data analysis

4.5.1 Lifetime scales

Let us consider typical time-resolved yield of oxygen dissociation obtained by means of the pump-pump excitation setup of the VMI apparatus. The right panel of Figure 4.28 shows normalised O^- yield signal as a function the pump-pump delay (two s-polarised equal intensity 60 fs pulses) as depicted by the black curve. The peak waist is approximately 140 fs. An expected pump-pump excitation profile is depicted by the green curve, being a convolution of two 60 fs pulses, the waist of the profile is nearly 90 fs. A single 60 fs pulse is depicted for comparison by the blue curve. Note: in this normalised presentation "zero yield" corresponds actually to a non-zero fixed magnitude yield of well separated in time pump-pump pulses, see panel A of Figure 4.26 for the unprocessed data.

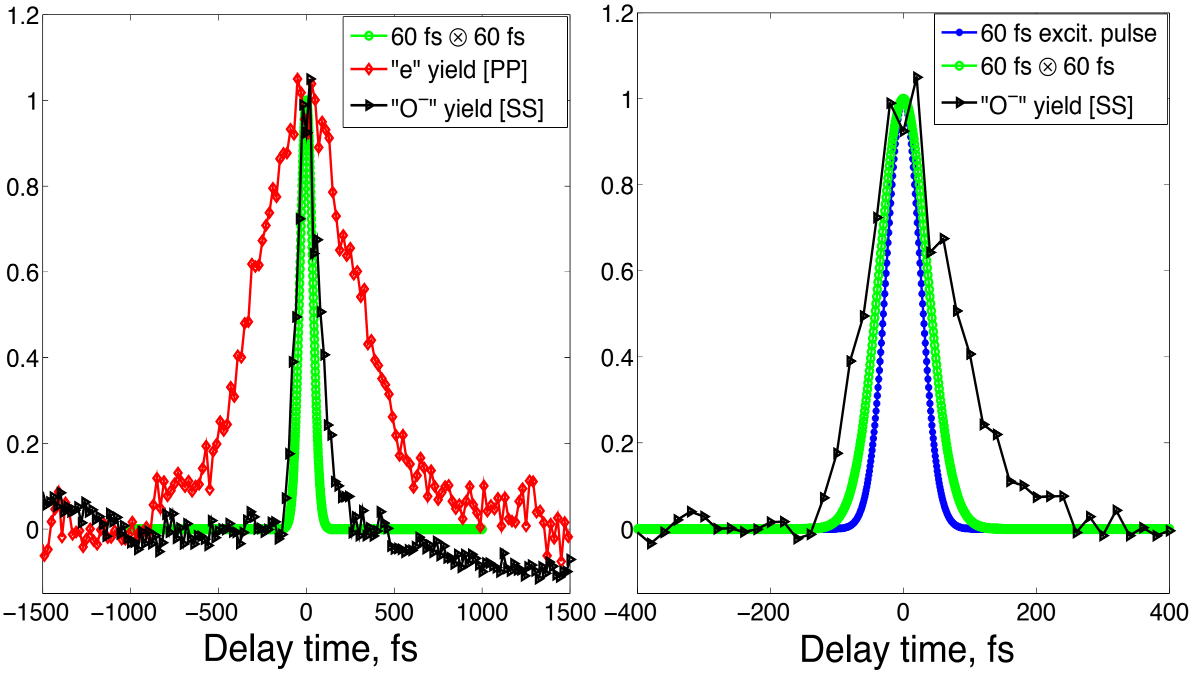

Figure 4.28: Pump-pump time-resolved yield of O_2 dissociation and electron emission from Au 150 grooves/mm grating. Simulated 60 fs excitation and self convoluted pulses are brought for comparison. All data is normalised. Left panel: green curve - simulated response of two 60 fs pulses, FWHM ≈ 90 fs; red curve - electron yield obtained by $p\&p-$polarised at 5 GW/cm^2 beams, FWHM ≈ 700 fs; black curve - O^- product obtained by $s\&s-$polarised at 300 GW/cm^2 beams, FWHM ≈ 140 fs. Right panel: finer resolved O^- yield, simulated response and 60 fs excitation pulse, blue curve.

The observed peak waist of 140 fs is attributed to the actual plasmon lifetime. After a 90 fs excitation has been “switch-off” the resulted gold film electrons coherent excitation has been dumped due to dephasing processes, such as electron-electron interactions and scattering. In our gold film sample, the dephasing time can be estimated as $140 - 90 = 50$ fs. This time is in general agreement with the published [131] value of 20 fs.

The left panel of the above figure compares on a larger scale the 140 fs oxygen dissociation curve with nearly $FWHM \approx 700$ fs pump-pump time-resolved electron emission (the red curve) obtained from the same Au 150 gr/mm grating. Nevertheless, the presented curve represents the highest peak contrast obtained at the PP polarisation state, all four polarisation states have shown similar waist magnitude. For more details, see Appendix E. Apart from the significantly different peaks’ waist magnitude, the electron emission has been detected at low intensity regime only (approximately 5 GW/cm^2, much below the dissociation threshold of 50 GW/cm^2), see Figure E.3. The post SP-enhanced electron emission (taking place after SP decay time) can be attributed, most probably, with ultrafast lattice heating [132]. The possible impact of electron emission on the O_2 dissociation will be discussed below.

4.5.2 Key facts about plasmon-assisted oxygen dissociation

Discussed below are a few questions that should be addressed to the observed oxygen dissociation.

4.5.2.1 Photo-dissociation scenario

It has experimentally been proven that (direct) photo-dissociation is undetectable when an excitation intensity level lays below the determined threshold of 3000 GW/cm^2. Moreover, a damage threshold of the gold films was approximately just 1000 GW/cm^2, preventing usage of excitation intensity above 850 GW/cm^2.

4.5.2.2 Magnitude and field-enhancement factor of Surface Plasmon field

The minimal intensity value at which SP-assisted O_2 dissociation has been observed is 50 GW/cm^2 (see Figure 4.24), providing a laser electric field of $E_{light} = 6.2 \times 10^8$ V/m. The following relation being utilised $E_{light} = \sqrt{2\sqrt{\mu_0/\epsilon_0} I_{light}}$, where I_{light} is the laser intensity. According to the estimated earlier (see Section 4.2.3) O_2 dissociation field threshold is approximately 2.6×10^{10} V/m. Thus, the SP field enhancement, γ, is approximately $\gamma \approx 2.6 \times 10^{10}/6.2 \times 10^8 = 42$, satisfying the requirement of $\gamma >> 1$.

4.5.2.3 Role of Surface Plasmon resonance

There is no doubt that state of (linear) polarisation of the excitation light affects the dissociation process, for example see Figure 4.21. An attempt to detect O_2 dissociation by means of a “flat surface” copper sample did not show any $O^{\pm}$ signal. Thus, absence of a dissociation signal on the flat copper surface proves the key role of SP in the O_2 dissociation.

4.5.2.4 No evidence of an electron collision-induced dissociation

Collisions of O_2 molecules with extensively emitted fast electrons may, in principle, lead to a dissociation of the former [133]. However, no experimental facts have been found to support this idea.

Firstly, the dissociation process is characterised by strong nonlinearity, $NL \simeq 4$, while electron emission, at the high intensity range, has shown nonlinearity order of $NL = 1.2$.

Secondly, an electrons emission excited by the pump-pump mode did not show any yield peak contrast at high intensity regime (an intensity regime where O_2 dissociation took place). Alternatively, as it can be seen from Figure 4.26, the pump-pump yield peak contrast of up to 9 times (900%) has been detected during the dissociation process.

An addition argument is the different lifetime of the yield peak contrast of electron emission (at low intensity regime) and O_2 dissociation (at high intensity regime), being approximately 700 fs and 150 fs respectively.

Lastly, emitted electron energy (of 1.7 eV) is too low to cause collision-induced dissociation of O_2 molecule (requiring 5.2 eV).

4.5.2.5 Dissociation efficiency

Rough estimation of a number of O_2 molecules being dissociated per pulse is approximately $0.5 - 5$ dissociations out of 500 molecules filling the excitation volume. Thus, the O_2 SP-assisted dissociation efficiency does not extend 1%.

4.6 Conclusions and Future work

4.6.1 Summary

Surface plasmon-assisted dissociation of oxygen has been experimentally observed by Time-of-Flight and mass-selected 2D projection imaging methods. $O^{\pm}$ ions data for spatial 2D and time-of-flight yield distribution have been shown. The dissociation process has strictly nonlinear character, the order of nonlinearity is 4 ± 0.5.

The Mach-Zehnder 60 femtosecond interferometer setup was deployed for temporal resolution of O_2 surface plasmon-assisted dissociation and found to be approximately 150 fs, almost twice longer than the convoluted pump-pump excitation profile of the FWHM = 90 fs.

No influence of a strong electron emission yield on the oxygen dissociation process has been observed.

The surface plasmon-assisted dissociation evidence can lead to future investigation of Local Field Distribution Imaging based on the Velocity Mapping Imaging method.

4.6.2 Future work

Current experimental evidence has been focused on the SP assisted dissociation of oxygen molecules, with required bond splitting energy of 5.2 eV. A few attempts have been made to achieve SP assisted ionisation of the inert gases such as Ar and Xe with nearest ionisation energy of 16.3 eV and 12.2 eV respectively as well as N (15.3 eV), however no ionisation products have been detected. In this case promising candidates can be fullerenes of C_{60} and C_{70}, outstanding with relatively low ionisation potential laying in the range of $7 - 8$ eV [134, 135]. These fullerenes have much heavier mass than oxygen, ensuring a benefit of better temporal resolution of time-of-flight based detectors.

Another important point is SP field enhancement. Due to asymmetric nature of the grating field amplification process is less effective comparing to the symmetric grating. In addition, deployment of a gold covered prism in the Kretschmann geometry (exposure of the film from the internal side through a prism) rather than a gold grating, in principle, will decrease any direct (undesired) laser ionisation near the surface.

As a long-range plan, arrays of nano-particles should be introduced for localised SP detection via ionisation (dissociation) of heavy gases/fullerenes.

Chapter 5

Conclusions

With the development of nanotechnology, it has become possible to construct nano-materials with "desirable" properties, on the one hand, and preserve "traditional" properties of the bulk material, on the other hand. This thesis clearly demonstrates a couple of such examples deploying femtosecond pulsed laser apparatus.

The investigation of long electron-hole recombination dynamics in the bulk-insulated silicon nanopillars sample shows that a diffusion has been the dominant process in the carriers recombination in bulk silicon experiments. Moreover, it is incorrect to deduce electron-hole recombination times characterising silicon material from experiments being based on the bulk samples due to a fast diffusion rate.

Another example of an engineering of the nano-material with new properties, is a sample built from crystalline silicon nano-inclusions imbedded in a thin film of amorphous silicon. We have shown, that a response of silicon nano-inclusions to the optical excitation can be strongly enhanced due to a positive interference in the layered sample. Thus, structural order acts as an amplification medium of a relatively weak response at the specific optical excitation.

Time-resolved photoluminescence from amorphous silicon nitride thin films has been studied by means of super-continuum femtosecond-based fiber laser. Electron-hole sub-nanosecond radiative recombination has been attributed to band-tail states. Furthermore, a delayed by a few nanoseconds weak recombination peak has been detected and attributed to the deep band-tail states.

Finally, in situ high vacuum setup based on the ions imaging and mass-spectroscopy techniques is proposed to investigate local electric field distributions on the nanometer scale.

In this setup, a femtosecond pulsed beam is responsible for an excitation of a sufficiently strong surface plasmon resonance resulting strong electromagnetic field in the vicinity of the sample's surface. Externally injected neutral molecules of gas undergo a dissociation or ionisation by means of the surface plasmon field. The initial ions momentum is proportional to a distribution of this field. A "bunch" of such ions can be collected in short time slots by a set of two-dimensional projections. The projection can take place in spatial and momentum coordinates. This information will indicate the investigated local field distribution. Application of a couple of delayed in time femtosecond pulses in a Mach-Zehnder geometry enables femtosecond resolution of surface dynamics: multi-photon electron emission and (plasmon-assisted) oxygen dissociation.

In summary, the obtained results in such different fields as ultrafast carriers relaxation dynamics, electron-hole recombination processes in semiconductors, plasmonics and molecular dissociation, confirm that femtosecond spectroscopy is an universal tool of an investigation of ultrafast processes.

To emphasise universality of ultrafast pulsed lasers, below are brought some examples of their successful deployment in a wide range of scientific fields [119, 136]: Terahertz Imaging, Raman Spectroscopy, Pulsed Laser Deposition, Multi-photon Excitation Microscopy, Light Detecting and Ranging, Laser Ablation, Fluorescence Spectroscopy, Confocal Microscopy, Atomic and Molecular Spectroscopy, Atom Trapping and Cooling; as well as in Life Science and Medicine.

Appendix B

The dielectric function

According to Adler [137], the dielectric function in a semiconductor is a tensor $\epsilon(q+G, q+G')$, where q is a wave vector and G and G' are reciprocal lattice vectors. With the off-diagonal components being essential for charge neutrality in the semiconductor, while the diagonal dielectric constant remains finite in the long-wavelength limit $\epsilon(q) = \epsilon(q,q)|_{q\to 0} \to \epsilon_0$. According to Biswas *et al.* [25], the diagonal part of the dielectric function could be expressed within the random-phase approximation as

$$\epsilon(q) = 1 + \frac{4\pi e^2}{q^2} \sum_k \sum_G \frac{f^0(k) - f^0(k+q+G)}{E(k+q+G) - E(k)} |\langle k| e^{i\vec{q}\cdot\vec{r}} |k+q+G\rangle|^2. \tag{B.1}$$

Here, $f^0(k)$ is the distribution function of the Bloch state $|k\rangle$ of energy $E(k)$.
For the ground state (filled valence band prepared at zero temperature) semiconductor with energy gap, E_g the dielectric constant in the long wavelength limit could be expressed as

$$\epsilon_g(q) \simeq 1 + \frac{4\pi N_0 e^2 \hbar^2}{m_e E_g^2} = 1 + (\frac{\hbar\omega_p}{E_g})^2, \tag{B.2}$$

where N_0 is a number of total electronic density, ω_p is the plasma frequency and m_e is the electron mass.
For a semiconductor with excited density of N_{e-h}, Eq. B.2 in the long wavelength limit generalizes into

$$\epsilon(q) \simeq 1 + \frac{k_s^2}{q^2} + \frac{4\pi(N_0 - N_{e-h})e^2\hbar^2}{m_e E_g^2}, \tag{B.3}$$

where k_s is a screening length. It can be described by the Debye-Hunckel formula for a hot classical electron gas at temperature T_e: $k_s^2 = \frac{4\pi(2N_{e-h})e^2}{\epsilon k_B T_e}$, where k_B is the Boltzmann constant and ϵ denotes the host dielectric constant.
Thus, Eq. B.3 could be expressed within Eq. B.2 as

$$\epsilon(q) \simeq 1 + \frac{k_s^2}{q^2} + (\epsilon_g(q) - 1)\frac{N_0 - N_{e-h}}{N_0}. \tag{B.4}$$

Appendix C

Three-level dynamic model

Below is presented an alternative, to the empiric model of Sabbah *et al.* [27] (see Section 2.4.1.2), method of silicon nanopillars data treatment.

The excitation mechanism of silicon nanopillars can be explained by introduction of an intermediate (virtual) level. Thus, effectively instead of two-level mechanism (valence-conduction bands) we regard a three-level model: valence band - intermediate level - conduction band. This scenario is shown schematically in Figure C.1.

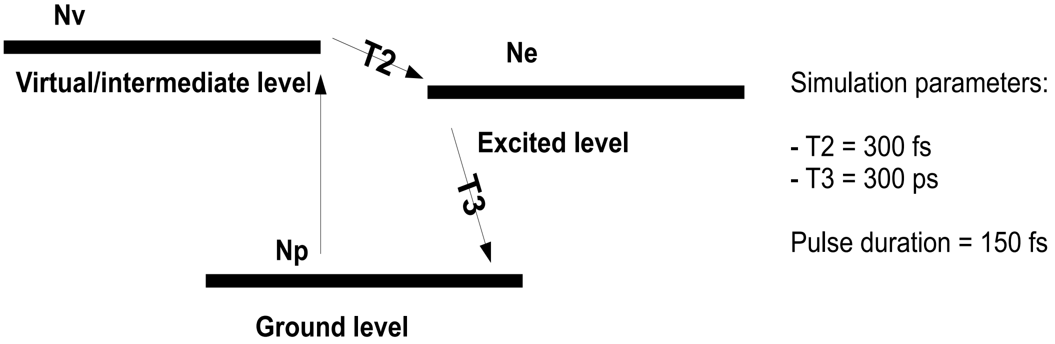

Figure C.1: Schematic band diagram of the tree-level model showing the excitation and decay processes via an intermediate level.

The following set of rate equations describes the excitation-relaxation dynamics of this model.

$$\frac{\partial N_p}{\partial t} = \frac{\alpha I_0(t)}{\hbar\omega_0} - \frac{N_e(t)}{\tau_3}, \tag{C.1}$$

$$\frac{\partial N_v}{\partial t} = \frac{\alpha I_0(t)}{\hbar\omega_0} - \frac{N_v(t)}{\tau_2} \tag{C.2}$$

$$\frac{\partial N_e}{\partial t} = \frac{N_v(t)}{\tau_2} - \frac{N_e(t)}{\tau_3}, \tag{C.3}$$

$$N_v(t) + N_e(t) = N_p(t). \tag{C.4}$$

Where $N_v(t)$ denotes the density of carriers being initially excited to the intermediate level and followed by a decay, with decay time τ_2, via electron-phonon relaxation. By N_p and N_e are denoted upper and lower excited states respectively. Recombination from the valence band characterised by τ_3. Term $\alpha I_0(t)/\hbar\omega_0$ has meaning of a number of absorbed photons and has a temporal profile proportional to the excitation femtosecond pulse of 150 fs. The absolute magnitude of this term has no importance within this simulation.

An example of fitting of this model with experimental data $\Delta R(t)/R_0$ is presented in Figure C.2 as well as predictions at various fluences below melting threshold, F_m. Comparison

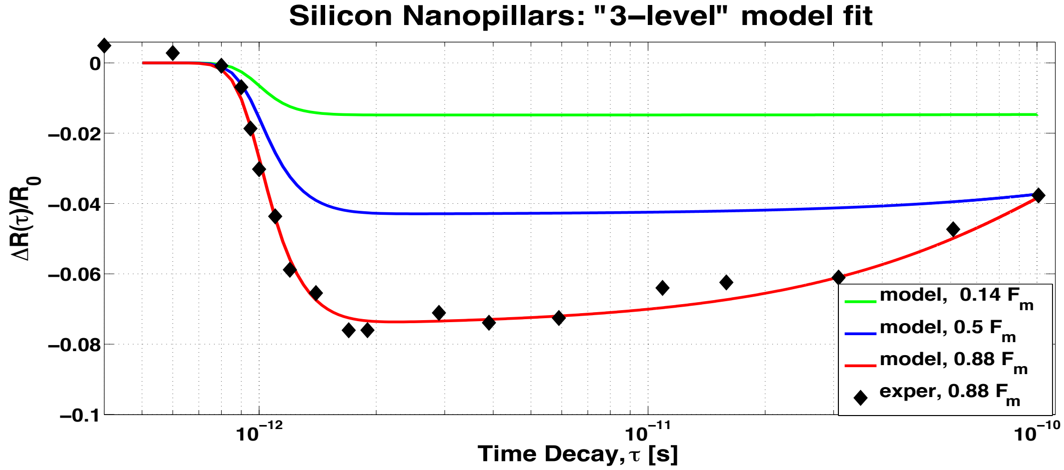

Figure C.2: Fitting of the three-level model results with the experimental data of reflectivity change, $\Delta R(\tau)/R_0$, in Silicon nanopillars. Fluence depicted in silicon melting threshold units, F_m.

of the extracted recombination and relaxation time constants from fitting of the three-level and the empiric model of Sabbah *et al.* [27], “m_{opt}”, to the experimental data of $\Delta R(\tau)/R_0$ for silicon nanopillars is shown in Figure C.3. Both models show similar results, while the empiric model of Sabbah is more sensitive to the changes in the region of small electron-hole density N_{e-h}.

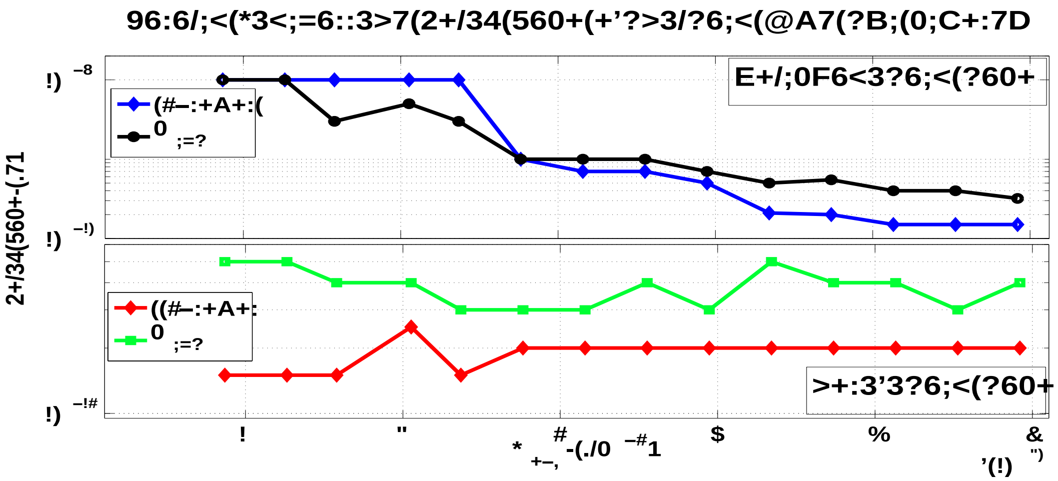

Figure C.3: Extracted recombination and relaxation time constants from fitting of “3-level” and the empiric model of Sabbah *et al.* [27] m_{opt} to the experimental data of $\Delta R(\tau)/R_0$ for silicon nanopillars.

Appendix D

Inversion methods

Further step to an experimentally detected 2D projection of a Newton sphere is to reconstruct original 3D momentum distribution of the considered event. From the mathematical point of view, a detected image (a projection) on the $X - Z$ coordinate system has to be reconstructed to the "natural" $R - \theta - \phi$ spherical system. In addition, a detector coordinates $X - Z$ are discreet real numbers rather than continuous scale, this fact brings irreducible transformation error. There are two main approaches [122]: inversion methods and forward convolution methods. The inversion methods take advantage of a symmetry of a projected image on the screen coordinates, while forward convolution has been used for general cases.

For purposes of oxygen dissociation with symmetrical distribution $sin^2\theta$ it is convenient to use inversion method approach [122] based on the inverse Abel transform [138]. There are a number of numerical algorithms based on the following methods: Abel-Hankel inversion method [139, 140], Back-projection and onion peeling method [124, 141], Iterative inversion [142] and Basis set expansion [143]. The mathematical and calculational complexity of these methods provides a calculation error below 2% according to [122].

D.1 Numerical back-projection

Here, we present a simple numerical approach initially "inspired" by more sophisticated Back-projection method of Helm *et al.* [124]. The idea of this method is to find numerically conversion matrix M which plays a roll of a Jacobean such that an experimentally detected image $Q(X, Z)$ will be transformed into a projected 2D distribution in the natural polar coordinates $R - \theta$, namely $Q(R, \theta) = M \times Q(X, Z)$. The process is described in Figure D.1. Shown in panel A of Figure D.1 is a spherically symmetric momentum distribution with a finite gaussian distribution. On panel B one can find simply the 2D projection of the initial 3D distribution in the polar coordinates, $Q(R, \theta)$. Described in panel C is a projection of the original 3D distribution to the detector plane, $Q(X, Z)$. It is possible to extract a matrix M responsible for 2D $X - Z$ to $R - \theta$ transformation. This matrix is depicted in panel D. The reconstructed 2D image in polar coordinates "inverse" $Q(R, \theta)$ from the $Q(X, Z)$ is depicted in panel E with a transformation numerical error of 4% in panel F. The initial radius of distribution should be extracted from the experimental image and discrete number of the $X - Z$ diminution should be equal to the camera pixels number. The number of pixels that has been used during the simulation is 120 for a quarter of a 3D momentum hemisphere.

The more complex, quintuple shell spherical momentum distribution simulation is presented in the Figure D.2. Above threshold [144] five-fold ionisation has been simulated. The figure descriptions and simulation parameters are the same like in the previous simulation. The simulation accuracy is about 3% as shown in panel F.

In addition, it has been shown an optimisation method of a minimisation of the digitalisation error. It has been shown that the error has particular minimum and cannot be zero.

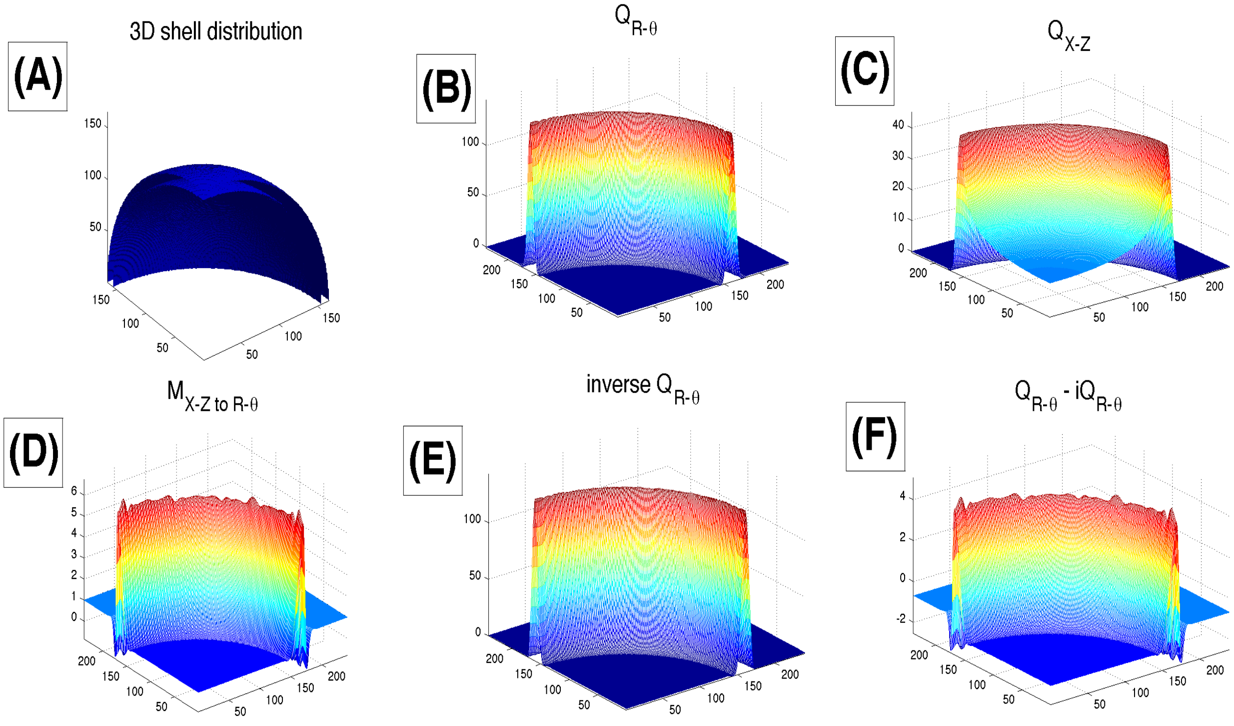

Figure D.1: Inversion method: reconstruction of a 3D momentum distribution from an experimentally detected 2D distribution, given in the discreet Cartesian coordinates. (A) An initial "single shell" spherical distribution, $Q(R, \theta, \phi)$ with a radius, R characterised by a finite gaussian width. (B) Projection of the Q into the 2D R, θ coordinates. (C) Projection of the Q into the 2D X, Z coordinates. (D) 2D transition matrix, M from X, Z into R, θ coordinates. (E) Reconstructed $Q_{rec}(R, \theta) = M \times Q(X, Z)$. (F) Reconstruction error, $Q(R, \theta) - Q_{rec}(R, \theta)$ is below 4%.

Providing a finite number of pixels describing the $X - Z$ space, this minimum corresponds to a particular value of digitalised $\theta - \phi$ coordinates. Namely, for the above simulations, for 120×120 pixel size of a quarter of the detector the optimal digitalisation of angular coordinates is approximately $1/1200$ *rad*. Downsizing of this value will cause higher transformation error, see Figure D.3 and Appendix D.3 for more details.

D.2 Back projection numerical algorithm

The following code is written in Matlab language. The purpose of this algorithm is to find a transformation matrix from two-dimensional discrete Cartesian coordinates to polar coordinates, R, θ. The initial conditions of this algorithm have to be taken from an experimentally measured 2D projection.

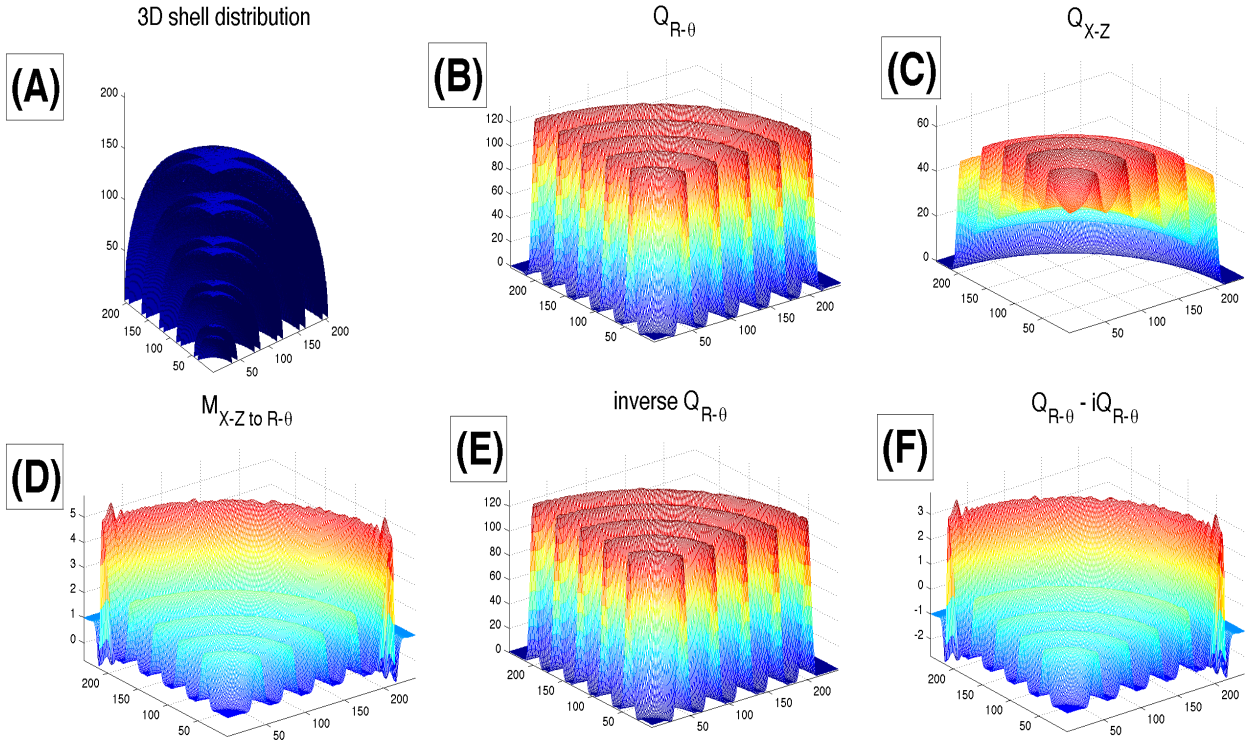

Figure D.2: Inversion method: reconstruction of a 3D momentum distribution from an experimentally detected 2D distribution, given in the discreet Cartesian coordinates. (A) An initial "quintuple shell" spherical distribution, $Q(R, \theta, \phi)$ with a radius, R characterised by a finite gaussian width. (B) Projection of the Q into the 2D R, θ coordinates. (C) Projection of the Q into the 2D X, Z coordinates. (D) 2D transition matrix, M from X, Z into R, θ coordinates. (E) Reconstructed $Q_{rec}(R, \theta) = M \times Q(X, Z)$. (F) Reconstruction error, $Q(R, \theta) - Q_{rec}(R, \theta)$ is below 3%.

```
%% 3D   1/8 sphere creation
R = 200; % outer sphere radius, TO BE DETERMINED FROM THE Exper. DATA
a = 1.2*R;
r = 1:a;
angl_res = 6*R; % TO BE DETERMINED FROM  SPHERE VOLUME SYMULATION
th = (0:1/(angl_res-1):(1/2))*pi;
phi = (0:1/(angl_res-1):1/2)*pi;
s = 0.5*R/10; % distr. deviation,
% TO BE DETERMINED FROM FITTING OF 1D SLICE OF THE Exper. DATA
D = zeros(1,a);
for h = 2:2:10
    D = D +  normpdf(r, h*R/10, s/2.3548); % distribution and NUMBER OF RINGS
end
```

```
D = D/max(D);
C = zeros(a,a,a);
Qrt = zeros(a,a);

for i = 1:length(r)

   for j = 1:length(th)

      for k = 1:length(phi)

        X = round((r(i))*sin(th(j))*cos(phi(k)));
        Y = round((r(i))*sin(th(j))*sin(phi(k)));
        Z = round((r(i))*cos(th(j)));

        if X==0
           X=1;
        end

        if Y==0
           Y=1;
        end

        if Z==0
           Z=1;
        end

        C(X,Y,Z) = D(i);

      end

      %% 2D  1/8 sphere projection on R-theta plane
        x = round(r(i)*sin(th(j)));
        z = round(r(i)*cos(th(j)));

        if x==0
           x=1;
        end

        if z==0
           z=1;
        end

        Qrt(x,z) = D(i);
   end
end
```

```
%% 3D 1/8 sphere
figure(1)
subplot(2,3,1)
p1 = patch(isosurface(C,.5),'FaceColor','blue','EdgeColor','none');
isonormals(C,p1)
view(3);
axis vis3d tight
camlight;
lighting phong
title('3D shell distribution','FontSize',20)

%% matrix massaging
V = sum(sum(sum(C)));
% smoothing of the  2D 1/8 sphere projection on R-theta plane
for i = 2:a-1
    for j = 2:a-1

        if Qrt(i,j)==0
            f = 4;

            if Qrt(i,j+1)==0
                f=f-1;
            end
            if Qrt(i,j-1)==0
                f=f-1;
            end
            if Qrt(i+1,j)==0
                 f=f-1;
            end
            if Qrt(i-1,j)==0
                f=f-1;
            end

            if f>0
                Qrt(i,j) = sum([Qrt(i,j-1) Qrt(i,j+1) Qrt(i-1,j) Qrt(i+1,j)])/f;
            end
        end

    end
end

Qrt = smoothn(Qrt, 20);
Vrt = sum(sum(Qrt));
Qrt = Qrt/Vrt*V;  % Normalisation

subplot(2,3,2)
```

```
mesh(Qrt)
axis tight
title('Q_{R-\theta}','FontSize',20)

%% 2D 1/8 sphere projection on XZ plane
Qxz = zeros(a,a);
for i=(1:a)

    Qxz = Qxz + C(:,:,i);
end

Vxz = sum(sum(Qxz));
Qxz = Qxz/Vxz*V;  % Normalisation
Qxz = smoothn(Qxz, 20);

subplot(2,3,3)
mesh(Qxz)
axis tight
title('Q_{X-Z}','FontSize',20)

%% Inverse matrix [experimental image]x[M_xz_rt] = Inverted Image,
%Px, Pz momentum space
Mxz_rt = (Qrt + 1)./(Qxz+ 1);

subplot(2,3,4)
mesh(Mxz_rt)
axis tight
title('M_{X-Z to R-\theta}','FontSize',20)

iQrt = Qxz.*Mxz_rt;
iQrt = iQrt - min(min(iQrt));

subplot(2,3,5)
mesh(iQrt)
axis tight
title('inverse Q_{R-\theta}','FontSize',20)

subplot(2,3,6)
mesh(Qrt-iQrt)
axis tight
title('Q_{R-\theta} - iQ_{R-\theta}','FontSize',20)
```

D.3 Optimal condition algorithm

The following code is written in Matlab language. The purpose is to show a transformation error dependence on the digital angular resolution of Θ and Φ during a 3D data conversion and 2D projection between spherical, R, Θ, Φ and Cartesian, X, Y, Z coordinate systems. The error arises due to discreet and finite nature of the R, X, Y and Z coordinates, representing a real imaging array of photo-sensors. For example, 480 × 640 pixels CCD camera. The optimal angular resolution of 1/1200 radian is found to produce the smallest error during the back projection procedure for a data taken by a 240×240 pixels photosensor. Described in Figure D.3 is a ratio of a spherical shell of a volume V given in spherical $V(R, \Theta, \Phi)$ and Cartesian $V(X, Y, Z)$ coordinates as a function of an angular resolution of Θ and Φ. The dependence minima is clearly seen in the inset.

```
R = 200;
a = 1.2*R;
r = 1:a;
s = 0.5*R/10; % distr. deviation
D = normpdf(r, R, s/2.3548); % distribution
D = D/max(D);
m = 100;
VV_100 = zeros(m,1);
for  w = 1:m
    angl_res = 500 + (w-1)*25;
    th = (0:1/(angl_res-1):(1/2))*pi;
    phi = (0:1/(angl_res-1):1/2)*pi;
    C = zeros(a,a,a);
    Q = zeros(a,a);
for i = 1:length(r)
   for j = 1:length(th)
       for k = 1:length(phi)
        X = round((r(i))*sin(th(j))*cos(phi(k)));
        Y = round((r(i))*sin(th(j))*sin(phi(k)));
        Z = round((r(i))*cos(th(j)));
        if X==0
           X=1;
        end
        if Y==0
           Y=1;
        end
        if Z==0
           Z=1;
        end
        C(X,Y,Z) = D(i);
      end
   end
end
```

```
%% digital sphere Volume in R,th, phi  a XYZ
V = 0;
for k=a:-1:2
    V = V + 4*pi/3*(r(k)^3-r(k-1)^3)*D(k);
end
V = (V+4*pi*D(1))/8;
Vxyz = sum(sum(sum(C)));
VV_100(w) = V/Vxyz;
end
w = 500 + ((1:m)-1)*25;
w = 1./w*pi/2;
plot(w, VV_100,'-*')
```

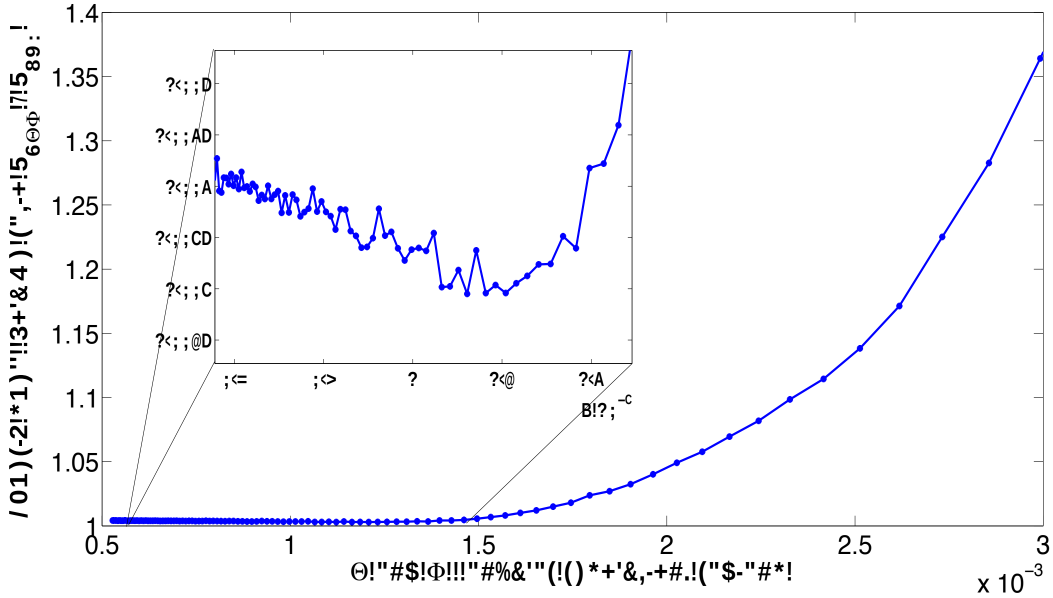

Figure D.3: Ratio of a spherical shell of volume V given in spherical $V(R,\Theta,\Phi)$ and Cartesian $V(X,Y,Z)$ coordinates as function of an angular resolution of Θ and Φ. The parameters R, X, Y and Z are integers in the following range $[1:240]$ reflecting discrete nature of an imaging sensor (i.e. CCD camera). Resolution of $1/1200$ rad provides the smallest error in the back projection process. Inset: a higher resolution presentation of the $V(R,\Theta,\Phi)/V(X,Y,Z)$ minima.

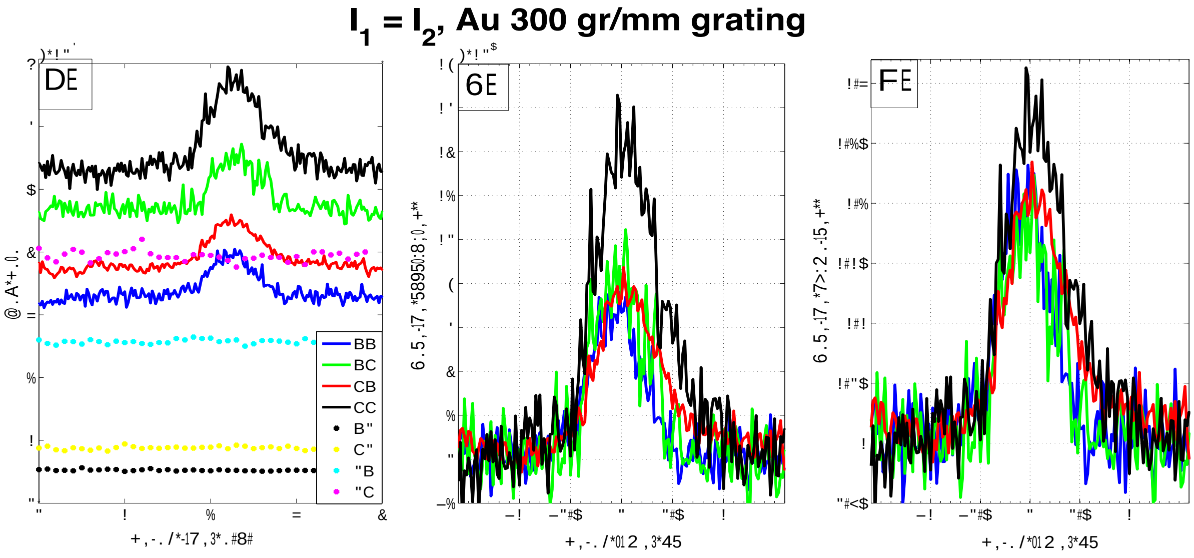

Figure E.2: Au 300 grooves/mm grating: pump-pump electron yield from for p- and s-polarised beams vs delay time. Panel A: raw data including net yield from each beam. Panel B: net yield contribution from the spatial and temporal overlap. Panel C: normalised to a value of the yield in the case of spatial overlap only. $I_1 = I_2 = 6$ GW/cm^2.

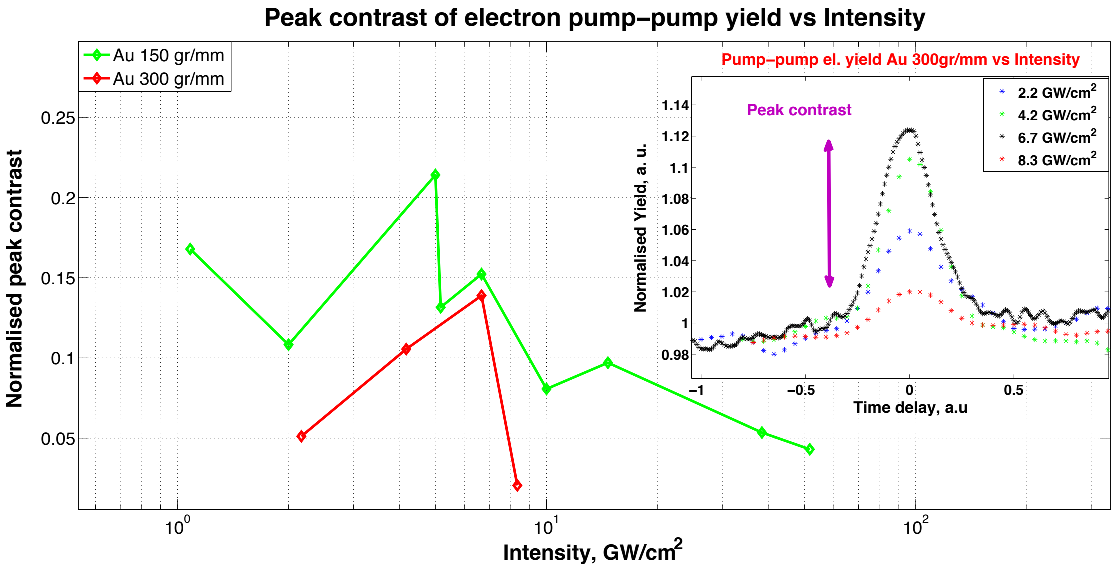

Figure E.3: Peak contrast of electron pump-pump emission yield as function of excitation intensity. Emission sources: Au 150 gr/mm and 300 gr/mm gratings. Inset: time-resolved data for Au 300 gr/mm is depicted for explicit presentation.

Bibliography

[1] www.nobelprize.org

[2] A. L. Cavalieri, N. Muller, Th. Uphues, V. S. Yakovlev, A. Baltuska, B. Horvath, B. Schmidt, L. Blumel, R. Holzwarth, S. Hendel, M. Drescher, U. Kleineberg, P. M. Echenique, R. Kienberger, F. Krausz and U. Heinzmann, Nature **449**, 1029 (2007).

[3] A. Othonos J. Appl. Phys. **83**, 1789 (1998).

[4] M. Aeschlimann, M. Bauer, D. Bayer, T. Brixner, F. J. G. de Abajo, W. Pfeiffer, M. Rohmer, C. Spindler and F. Steeb, Nature, Letters, **446**, 301 (2007).

[5] M. Stockman, M. Kling, U. Kleineberg and F. Krausz, Nature, Photonics, **1**, 539 (2007).

[6] M. Kjellberg, O. Johansson, F. Jonsson, A. V. Bulgakov, C. Bordas, E. E. B. Campbell and K. Hansen, Phys. Rev. A **81**, 023202 (2010).

[7] M. F. Kling, J. Rauschenberger, A. J. Verhoef, E. Hasovic, T. Uphues, D. B. Milosevic, H. G. Muller and M. J. J. Vrakking, New J. Phys. **10** ,025024 (2008).

[8] A. Rouzee, P. Johnsson, E. V. Gryzlova, H. Fukuzawa, A. Yamada, W. Siu, Y. Huismans, E. Louis, F. Bijkerk, D. M. P. Holland, A. N. Grum-Grzhimailo, N. M. Kabachnik, M. J. J. Vrakking and K. Ueda, Phys. Rev. A **83**, 0314011 (2011).

[9] K. Sokolowski-Tinten, C. Blome, J. Blums, A. Cavalleri, C. Dietrich, A. Tarasevitch, I. Uschmann, E. Forster, M. Kammler, M. Horn-von-Hoegen and D. von der Linde, Nature **422**, 287 (2003).

[10] A. Kaplan, M. Lenner and R. E. Palmer, Phys. Rev. B **76**, 0734011 (2007).

[11] T. Hertel, E. Knoesel, M. Wolf, and G. Ertl, Phys. Rev. Lett. **76**, 535 (1996).

[12] V. V. Kruglyak, R. J. Hicken, P. Matousek and M. Towrie , Phys. Rev. B **75**, 035410 (2007).

[13] C. V. Shank, R. Yen and C. Hirlimann, Phys. Rev. Lett. **50**, 454 (1983).

[14] M. Weinelt, M. Kutschera, T. Fauster and M. Rohlfing, Phys. Rev. Lett. **92**,1268011 (2004).

[15] T. Ichibayashi and K. Tanimura, Phys. Rev. Lett. **102**, 0874031 (2009).

[16] V. V. Kruglyak, R. J. Hicken, M. Ali and B. J. Hickey, A. T. G. Pym and B. K. Tanner, Phys. Rev. B **71**, 233104 (2005).

[17] S. Zollnera, K. D. Myersa, J. M. Dolana, D. W. Baileyb, C. J. Stantonc, Thin Solid Films, Elsevier, **313314**, 13, 568 (1998).

[18] Z. L. Samson, K. F. MacDonald and N. I. Zheludev, J. Opt. A: Pure Appl. Opt. **11** 114031 (2009).

[19] T. Tada, A. Hamoudi, T. Kanayama, K. Koga, Appl. Phys. Lett. **70** 2538 (1997).

[20] K. E. Myers, Q. Wang, and S. L. Dexheimer, Phys. Rev. B **64**, 1613091 (2001).

[21] V. V. Poborchii, T. Tada, T. Kanayama, Physica E **7** 545 (2000).

[22] C. Kittel "Quantum Theory of Solids", JohnWiley&Sons, Inc, New York (1963).

[23] K. Sokolowski-Tinten and D. von der Linde, Phys. Rev. B **61**, 2643 (2000).

[24] D. E. Aspnes and A. A. Studna, Phys. Rev. B **27**, 985 (1983).

[25] R. Biswas and V. Ambegaokar, Phys. Rev. B **26**, 1980 (1982).

[26] R. A. Abram, G. N. Childs and P. A. Saunderson, J. Phys. C, **17** 6105 (1984).

[27] A. J. Sabbah and D. M. Riffe, Phys. Rev. B **66**, 165217 (2002).

[28] O. Stenzel, "The physics of thin film optical spectra, an introduction", Springer, Berlin (2005).

[29] O. S. Heavens, "Optical properties of thin solid films", Dover publications, Inc, New York (1991).

[30] D. J. Bradely et al., Appl. Phys. Lett. **16**, 53 (1970). M. Schelev et al., Appl. Phys. Lett. **18**, 354 (1971).

[31] E. O. Goebel, W. Graudzus, and P. H. Liang, J. Lumin. **24**, 573 (1981).

[32] H. Mahr and M. D. Hirch, Opt. Commun. **13**, 96 (1975).

[33] M. C. Downer and C. V. Shank, Phys. Rev. Lett. **56**, 761 (1986).

[34] A. Esser, W. Kutt, M. Strahnen, G. Maidhorn, and H. Kurz, Appl. Surf. Sci. **46**, 446 (1990); F. E. Doany, D. E. Grischkowsky, and C.-C. Chi, Appl. Phys. Lett. **50**, 460 (1987);

[35] F. E. Doany and D. E. Grischkowsky, Appl. Phys. Lett. **52**, 36 (1988).

[36] W. Kutt, A. Esser, K. Seibert, U. Lemmer, and H. Kurz, Proc. SPIE **1268**, 154 (1990).

[37] T. Tanaka, A. Harata, and T. Sawada, J. Appl. Phys. **82**, 4033 (1997).

[38] A. J. Sabbah and D. M. Riffe, J. Appl. Phys. **88**, 6954 (2000).

[39] T. Tanaka, A. Harata, and T. Sawada, Jpn. J. Appl. Phys. **35**, 3642 (1996).

[40] C. M. Li, Z. C. Ying, T. Sjodin, and H.-L. Dai, Appl. Phys. Lett. **66**, 3501 (1995); C. M. Li, T. Sjodin, and H.-L. Dai, Phys. Rev.B **56**, 15 252 (1997).

[41] T. Sjodin, H. Petek, and H.-L. Dai, Phys. Rev. Lett. **81**, 5664 (1998).

[42] R. Buhleier, G. Lupke, G. Marowsky, Z. Gogolak, and J. Kuhl, Phys. Rev. B **50**, 2425 (1994).

[43] J. E. Rothenberg, Opt. Lett. **13**, 713 (1980).

[44] O. B. Wright and V. E. Gusev, Appl. Phys. Lett. **66**, 1190 (1995).

[45] J. Bokor, R. Storz, R. R. Freeman, and P. H. Bucksbaum, Phys. Rev. Lett. **57**, 881 (1986).

[46] N. J. Halas and J. Bokor, Phys. Rev. Lett. **62**, 1679 (1989).

[47] M. W. Rowe, H. Liu, G. P. Williams, and R. T. Williams, Phys. Rev. B **47**, 2048 (1993).

[48] J. R. Goldman and J. A. Prybyla, Phys. Rev. Lett. **72**, 1364 (1994).

[49] S. Jeong, H. Zacharias, and J. Bokor, Phys. Rev. B **54**, R17 300 (1996).

[50] S. Jeong and J. Bokor, Phys. Rev. B **59**, 4943 (1999).

[51] J.C. Diels, W. Rudolph, "Ultrashort laser Pulse Phenomena", Academic Press, San Diego (1995).

[52] D. E. Spence, P. N. Kean and W. Sibbett, Oprics Letters, **16**, 42 (1991).

[53] E. Vallat-Sauvain, U. Kroll, J. Meier, N. Wyrsch, A. Shah, J. Non-crystalline Solids, **266-269**, 125 (2000).

[54] S. A. Boden and D. M. Bagnall, Appl. Phys. Lett. **93**, 1331081 (2008).

[55] G. R. Lin, Y. C. Chang, E. S. Liu, H. C. Kuo and H. S. Lin, Appl. Phys. Lett. **90**, 1819231 (2007).

[56] V. V. Poborchii, T. Tada and T. Kanayama, J. Appl. Phys. **91**, 3299 (2002).

[57] L. D. Landau and E. M. Lifshitz, Electrodynamics of Continuous Media, Elsevier, Oxford, (1984).

[58] Spectrophotometer "Lambda 1000", Perkin-Elmer Ltd., at The Technion - Israel Institute of Technology (TIIT), Haifa, Israel.

[59] S. Jeong and J. Bokor, Phys. Rev. B **59**, 4943 (1999).

[60] L. V. Mercaldo, E. M. Esposito, P. D. Veneri, B. Rezgui, A. Sibai and G. Bremond, J. Appl. Phys. **109**, 093512 (2011).

[61] N. M. Park, C. J. Choi, T. Y. Seong, and S. J. Park, Phys. Rev. Lett. **86**, 1355 (2001); N. M. Park, S. H. Kim, G. Y. Sung, and S. J. Park, Chem. Vap. Deposition **8**, 254 (2002).

[62] L. Dal Negro, J. H. Yi, J. Michel, L. C. Kimerling, T. W. F. Chang, V. Sukhovatkin and E. H. Sargent, Appl. Phys. Lett. **88**, 233109 (2006).

[63] M. Molinari, H. Rinnert and M. Vergnat, J. Appl. Phys. **101**, 123532 (2007).

[64] G. Conibeer, M. Green, E. C. Cho, D. Konig, Y. H. Cho, T. Fangsuwannarak, G. Scardera, E. Pink, Y. Huang, T. Puzzer, S. Huang, D. Song, C. Flynn, S. Park, X. Hao and D. Mansfield, Thin Solid Films **516**, 6748 (2008).

[65] F. Delachat, M. Carrada, G. Ferblantier, J. J. Grob and A. Slaoui, Nano-technology **20**, 415608 (2009).

[66] L. V. Mercaldo, P. Delli Veneri, E. Esposito, E. Massera, I. Usatii and C. Privato, Mater. Sci. Eng. B **77** 159 (2009).

[67] B. Rezgui, A. Sibai, T. Nychyporuk, M. Lemiti, G. Bremond, D. Maestre and O. Palais, Appl. Phys. Lett. **96**, 183105 (2010).

[68] I. G. Austin, W. A. Jackson, T. M. Searle, P. K. Bhat and R. A. Gibson, Phil. Mag. B **52**, 271 (1985).

[69] F. Giorgis, C. Vinegoni and L. Pavesi, Phys. Rev. B **61**, 4693 (2000).

[70] S. V. Deshpande, E. Gulari, S. W. Brown, and S. C. Rand, J. Appl. Phys. **77**, 6534 (1995).

[71] Y. Liu, Y. Zhou, W. Shi, L. Zhao, B. Sun and T. Ye, Materials Letters **58** 2397 (2004).

[72] M. S. Minsky, S. B. Fleischer, A. C. Abare, J. E. Bowers, E. L. Hu, S. Keller and S. P. Denbaars, Appl. Phys. Lett. **72**, 1066 (1998).

[73] K. S. Seol, T. Watanabe, M. Fujimaki, H. Kato, Y. Ohki and M. Takiyama, Phys. Rev. B **62**, 1532 (2000).

[74] W. Siebert, R. Carius, W. Fuhs and K. Jahn, Phys. Status Solidi B **140**, 311 (1987).

[75] L. R. Tessler, Solid State Commun. **111**, 193 (1999).

[76] H. Kato, N. Kashio, Y. Ohki, K. S. Seol, and T. Noma, J. Appl. Phys. **93** 239 (2003).

[77] C. Tsang and R. A. Street, Phys. Rev. B **19**, 3027 (1979).

[78] Infrared devises research and development. D.C. Sirica Ltd, Haifa, Israel.

[79] Fianium Ltd., Southampton SO31 4RA, United Kingdom.

[80] Becker&Hickl GmbH, Nahmitzer Damm 30, 12277 Berlin, Germany.

[81] FAST ComTec GmbH, Grnwalder Weg 28A, 82041 Oberhaching/Mnchen, Germany.

[82] Rhodamine 110 chloride 83695 - BioReagent, suitable for fluorescence. Sigma-Aldrich Company Ltd. The Old Brickyard, New Road, Gillingham, Dorset, SP8 4XT, United Kingdom.

[83] P. M. Goodwin, W. P. Ambrose, J. C. Martin, and R. A. Keller, Anal. Chem. **66**, 64 (1994).

[84] C. V. Shank, R. L. Fork, R. Yen, J. Shah, B. I. Green, A. C. Gossard, and C. Weisbuch, Solid Sate Commun., **47** N12, 981 (1983). C. V. Shank, R. L. Fork, R. F. Leheny, and J. Shah Phys. Rev. Lett. **42** 112 (1979). R. F. Leheny, J. Shah, R. L. Fork, C. V. Shank and A. Migus, Solid Sate Commun., **31** 809 (1979).

[85] R. A. Street, Adv. Phys. **30** 593 (1981).

[86] W. A. Jackson, T. M. Searle, I. G. Austin, and R. A. Gibson, J. Non-Cryst. Solids **77&78** 909 (1985).

[87] F. Urbach, Phys. Rev. **92** 1324 (1953).

[88] J. Kistner, X. Chen, Y. Weng, H. P. Strunk, M. B. Schubert and J. H. Werner, J. Appl. Phys. **110** 023520 (2011).

[89] L. Pavesi and M. Ceschini, Phys. Rev. B **48** 17625 (1993).

[90] B. A. Wilson and T. P. Kerwin, Phys. Rev. B **25** 5276 (1982).

[91] R. A. Street, Solid State Commun. **34** 157 1980.

[92] O. Schmidt, M. Bauer, C. Wiemann, R. Porath, M. Scharte, O. Andreyev, G. Schonhense and M. Aeschlimann, Appl. Phys. B **74**, 223 (2003).

[93] H. Helm, N. Bjerre, M. J. Dyer, D. L. Huestis, and M. Saeed, Phys. Rev. Lett. **70**, 3221 (1993).

[94] H. Reather, Excitation of Plasmons and Interband transitions by Electropns, Springer-Verlag, Berlin, (1980).

[95] H. Raether, Surface Plasmons, Springer-Verlag, Berlin, (1988).

[96] The online database of the Ioffe Physical Technical Institute, Russian Academy of Sciences.

[97] S. E. Irvine, A. Y. Elezabi Phys. Rev. A **73**, 013815 (2006).

[98] D. Sarid and W. Challener, Modern Introduction to Surface Plasmons, Cambridge University Press, (2010).

[99] S. Kawata and V. M. Shalaev, Nanophotonics with Surface Plasmons, Advances in Nano-Optics and Nano-Photonics, Elsevier, (2007).

[100] J. Zawadzka, D. A. Jaroszynski, J. J. Carey, K. Wynne, Nuclear Instruments and Methods in Physics Research A **445**, 324, (2000).

[101] H. A. H. Boot and R. B. R. S. Harvie, Nature **180**, 1187 (1957). A. V. Gaponov and M. A. Miller, Sov. Phys.-JETP **7**, 168 (1958).

[102] L. D. Landau, E. M. Lifshitz, Mechanics, Pergamon Press, Oxford (1969).

[103] J. Kupersztych, Phys. Rev. Lett. **54**, 1385 (1985).

[104] J. Kupersztych, P. Monchicourt, and M. Raynaud, Phys. Rev. Lett. **86**, 5180 (2001).

[105] H. E. Elsayed-Ali, T. B. Norris, M. A. Pessot and G. A. Mourou, Phys. Rev. Lett. **58**, 1212 (1987).

[106] R. W. Schoenlein, W. Z. Lin and J. G. Fujimoto, Phys. Rev. Lett. **58**, 1680 (1987).

[107] S. E. Irvine and A. Y. Elezzabi Appl. Phys. Lett. **86**, 264102 (2005).

[108] L. D. Landau and E. M. Lifshitz, Quantum Mechanics, Pergamon, New York, (1965).

[109] C. Toth, G. Farkas, and K. L. Vodopyanov, Appl. Phys. B: Photophys. Laser Chem. **53**, 221 (1991).

[110] F. Bisio, M. Nyvlt, J. Franta, H. Petek and J. Kirschner, Phys. Rev. Lett. **96**, 087601 (2006).

[111] G. P. Banfi, G. Ferrini, M. Peloi, and F. Parmigiani, Phys. Rev. B **67**, 035428 (2003).

[112] L. Miaja-Avila, C, Lei, M. Aeschlimann, J. L. Gland, M. M. Murnane, H. C. Kapteyn and G. Saathoff, Phys. Rev. Lett. **97**, 113604 (2006).

[113] G. Saathoff, L. Miaja-Avila, M. Aeschlimann, M. M. Murnane and H. C. Kapteyn, Phys. Rev. A **77**, 022903 (2008).

[114] P. S. Kirchmann, L. Rettig, D. Nandi, U. Lipowski, M. Wolf, U. Bovensiepen, Appl. Phys. A **91**, 211 (2008).

[115] M. Kreiter, S. Mittler, W. Knoll and J. R. Sambles, Phys. Rev. B **65**, 125415 (2002).

[116] B. deB. Darwent, Bond Dissociation Energies in Simple Molecules, National Bureau of Standards, US (1970).

[117] A. Bondi, J. Phys. Chem. **68** 441 (1964).

[118] W. H. Weber and G. H. Ford, Optics Letters **6** 122 (1981).

[119] Coherent Inc, 5100 Patrick Henry Drive, Santa Clara, CA 95054 USA.

[120] Kore Technology Ltd, Cambridgeshire Business Park Ely, Cambridgeshire, CB7 4EA, UK.

[121] Stefan Kaesdorf, Geraete fuer Forschung und Industrie, Gabelsbergerstr. 59, D-80333 Muenchen, Germany.

[122] B. Whitaker, Imaging in Molecular Dynamics Technology and Applications, Cambridge University Press (2003).

[123] D. H. Parker, Chapter 1: Velocity mapping studies of molecular photodissociation and photoionization dynamics, from Photoionization and photodetachment, Advanced Series in Physical Chemistry - Vol. 10, World Scientific (2000).

[124] C. Bordas and F. Paulig, H. Helm and D. L. Huestis, Rev. Sci. Instrum. **67** (6) 2257 (1996).

[125] Edmund Optics Ltd, Unit 1, Opus Avenue, Nether Poppleton, York, YO26 6BL, UK.

[126] Richardson Gratings, part of the Newport Corporation, Global Headquarters, 1791 Deere Avenue, Irvine CA 92606, USA.

[127] S. A. Maier, Plasmonics: Fundamentals and Applications. Springer (2007).

[128] J. R. Krenn, D. Somitsch, W. Gotschy, A. Leitner and F. R. Aussenegg, Chemistry and Materials Science, Photons and Local Probes, **300**, 181-187 (1995).

[129] Scientific Instrument Services Inc, 1027 Old York Road. Ringoes, NJ 08551-1054, USA.

[130] A. H. Sommer, Photoemissive Materials, Krieger, Huntington, (1980).

[131] K. Puech, F. Z. Henari, W. J. Blau, D. Duff, G. Schmid, Chem. Phys. Lett. **247**, 13 (1995).

[132] M. Ligges, I. Rajkovic, P. Zhou, O. Posth, C. Hassel, G. Dumpich, and D. von der Linde, Appl. Phys. Lett. **94**, 101910 (2009).

[133] B. Eliasson and U. Kogelschatz, J. Phys. B: At. Mol. Phys. **19**, 1241 (1986).

[134] D.L. Lichtenberger, K. W. Nebesny, C.D. Ray, D.R. Huffman and L.D Lamb, Chem. Phys. Lett., **176**, 203 (1991).

[135] D.L. Lichtenberger, M.E. Rempe and S.B. Godosha, Chem. Phys. Lett. **198**, 454 (1992).

[136] www.coherent.com/Applications/

[137] S. L. Adler, Phys. Rev. 126, 413 (1962).

[138] A. J. R. Heck, D. W. Chandler, Annu. Rev. Phys. Chem. **46**, 335 (1995).

[139] L. M. Smith, D. R. Keefer, J. Quant. Spectrosc. Radiat. Transfer, **39**, 367 (1988).

[140] W. Castleman, Digital Image Processing, Prince Hall London (1978).

[141] J.Winterhalter, D. Maier, J. Hornerkamp, V. Schyja, H. Helm, J. Chem. Phys. **110**, 11187 (1999).

[142] M. J. J.Vrakking, Rev. Sci. Instrum. **72**, 4084 (2001).

[143] V. Dribinski, A. Ossadtchi, V. Mandelshtam, H. Reisler, Rev. Sci. Instrum **73**, 2634 (2002).

[144] Y. F. Ni, S. Zamith, F. Lpine, T. Marchenko, M. F. Kling, O. Ghafur, H. G. Muller, G. Berden, F. Robicheaux and M. J. J. Vrakking, Physical Review A **78**, 0134131 (2008).